Cellular origin influences the immune microenvironment in a pancreatic cancer mouse model with loss of *Pten* and activation of KRAS

by

Yan Dou

B.S., The University of Washington, 2019

A THESIS SUBMITTED IN PARTIAL FULFILLMENT OF

THE REQUIREMENTS FOR THE DEGREE OF

MASTER OF SCIENCE

in

THE FACULTY OF GRADUATE AND POSTDOCTORAL STUDIES

(Cell and Developmental Biology)

THE UNIVERSITY OF BRITISH COLUMBIA

(Vancouver)

May 2022

The following individuals certify that they have read, and recommend to the Faculty of Graduate and Postdoctoral Studies for acceptance, a thesis entitled:

Cellular origin influences the immune microenvironment in a pancreatic cancer mouse model with loss of *Pten* and activation of KRAS

submitted by Yan Dou in partial fulfillment of the requirements for

the degree of Master of Science

in Cell and Developmental Biology

Examining Committee:

Janel Kopp, Assistant Professor, Cell and Developmental Biology, UBC
Co-supervisor

James Johnson, Professor, Cell and Developmental Biology, UBC
Co-supervisor

Kenneth Harder, Associate Professor, Microbiology and Immunology, UBC
Supervisory Committee Member

Kevin Bennewith, Associate Professor, Pathology and Laboratory Medicine, UBC
Additional Examiner

Additional Supervisory Committee Members:

Pauline Johnson, Professor, Microbiology and Immunology, UBC
Supervisory Committee Member

Abstract

Pancreatic ductal adenocarcinoma (PDAC) is a devastating disease with an overall 5-year survival rate of merely 10%. Mouse studies in the past decade have made progress towards a better understanding of how PDAC cellular origin affects tumorigenesis. However, there is little study done on the immune microenvironment differences between acinar and ductal cell-derived precursor lesions and PDAC. Following our previous study that showed loss of *Pten* with oncogenic $Kras^{G12D}$ mutations in the ductal cells ($KPten^{\Delta Duct/+}$) resulted the formation of intraductal papillary mucinous neoplasias (IPMN) as the precursor lesion in mice, we further found similar mutations in the acinar cells ($KPten^{\Delta Acinar/+}$) formed pancreatic intraepithelial neoplasia (PanIN) instead. I subsequently used the $KPten^{\Delta Duct/+}$ and $KPten^{\Delta Acinar/+}$ models to elucidate the effect of cellular origin on the immune microenvironment by performing immunohistochemistry. I focused on immune cell infiltration densities in precursor lesions and PDAC derived from $KPten^{\Delta Duct/+}$ and $KPten^{\Delta Acinar/+}$ mice and found that immune cell population and its changes throughout tumorigenesis are different starting at a precursor lesion stage between these two models. Additionally, macrophages polarized by conditioned media derived from $KPten^{\Delta Duct}$ PDAC cells were polarized in less magnitude compared with macrophages polarized by $KPten^{\Delta Acinar}$ PDAC cells. This difference in polarization was at least partially due to the lower expression of GM-CSF in $KPten^{\Delta Duct}$ PDAC cells. Our study is the first to directly compare immune cell population between acinar- and ductal-derived PDAC with the same genetic background. Our study suggests cellular origin could influence PDAC immune heterogeneity.

Lay Summary

Pancreatic cancer is a devastating disease with an average 5-year survival rate of only 10%. Currently, there is no effective immunotherapy treatment for pancreatic cancer because the immune population around the tumor is heterogeneous among patients. One of the factors that could contribute to this heterogeneity is the cellular origin of pancreatic cancer. To address this hypothesis, I used two mouse models that formed pancreatic tumors from different cellular origins and focused on their immune cell population. I found that the pancreatic immune infiltration is different between the two mouse models during the progression of tumors. In addition, I found that cellular origin resulted in distinct phenotypes of macrophages, which was driven, in part, by the difference in the expression of the cytokine GM-CSF. Our study is the first to show that cellular origin could modulate the immune environment in pancreatic cancer, suggesting it could contribute to the immune heterogeneity seen in patients.

Preface

Experiments were designed and executed by Yan Dou in consultation with Dr. Janel Kopp. Most of the husbandry for mice used in this study were conducted at the University of California, San Diego, by Dr. Janel Kopp, in full compliance of all protocols as approved by the San Diego Animal Care and Use Committees. The rest of the mice used in this study were bred and maintained by Wesley Hunt, Atefeh Samani, Farnaz Taghizadeh, as well as the staff of the Modified Barrier Facility (MBF). These latter animal experiments were approved by the University of British Columbia Animal Care and Use Committees. All primary pancreatic tumor cell lines used in this study were generated by Dr. Janel Kopp, Atefeh Samani, Farnaz Taghizadeh, Wesley Hunt, Kayla Bolduc, and Karnjit Sarai. The F4/80 staining was conducted and analyzed by Yan Dou with help from Tiffany Wai; CD8 and FOXP3 staining and quantification were performed by Ken H. Chu and Justin Chhour. The CD206 staining was done by Ken H. Chu and the quantification was performed by Yan Dou. All cell culture experiments regarding RAW 264.7 and bone marrow-derived macrophages, and the culture of all primary pancreatic tumor cell lines were performed by Yan Dou. All RNA-sequencing was performed by the BRC sequencing core and Dr. Stephane Flibotte performed the sequencing analysis and the production of all heatmaps and the PCA plot in chapters 4.4, 4.5, and 4.6. All other experiments such as qPCR, gene ontology analysis, and Venn diagram graphs in chapters 4.2, 4.3, 4.4, 4.5, and 4.6 were performed by Yan Dou. Analysis of all data except those related to RNA-sequencing was done by Yan Dou in consultation with Dr. Janel Kopp.

Animal protocols were approved by the University of British Columbia Animal Care Committee and the certificates numbers are listed here: # A18-0224 and # A18-0225.

Table of Contents

List of Tables

List of Figures

List of Abbreviations

ADM- acinar-to-ductal metaplasia

AKT- protein kinase B

Arg1- arginase 1

Arid5a- AT-rich interaction domain 5A

BCA- bicinchoninic acid assay

BMDMs- bone marrow-derived macrophages

BPE- bovine pituitary extract

BSA- bovine serum albumin

C-EMT- complete EMT

CAFs- cancer associated-fibroblasts

CCL5- chemokine (C-C motif) ligand 5

Ccl6- chemokine (C-C motif) ligand 6

Ccl9- chemokine (C-C motif) ligand 9

Ccr1- C-C motif chemokine receptor 1

Ccr5- C-C chemokine receptor type 5

Cd163- cluster of differentiation 163

CD4- cluster of differentiation 4

CD68- cluster of differentiation 68

CD8- cluster of differentiation 8

Cd86- cluster of differentiation 86

CDKN2A- cyclin dependent kinase inhibitor 2A

Cre (CreER)- cre recombinase, estrogen receptor conjugated

Csf2rb- colony stimulating factor 2 receptor subunit beta

CTLA-4- cytotoxic T lymphocyte-associated protein

CXCL12- C-X-C motif chemokine ligand 12

Cxcr2- CXC chemokine receptor 2

DAB- 3,3'-diaminobenzidine tetrahydrochloride

EMT- epithelial-to-mesenchymal transition

FBS- fetal bovine serum

FBW7- F-box and WD repeat domain-containing 7

FFPE- formalin-fixed paraffin-embedded

FOXP3- forkhead box P3

GM-CSF (*Csf2*)- granulocyte-macrophage colony-stimulating factor

GO- gene ontology

HRP- horseradish protein

IFN-γ- interferon gamma

IHC- immunohistochemistry

IL-13-interleukin 13

IL-4- interleukin 4

Il10- interleukin 10

Il6- interleukin 6

iNOS (*Nos2*)- nitric oxide synthase

IPMN- intraductal papillary mucinous neoplasia

iPSC- induced pluripotent stem cells

ITS- insulin-transferrin-selenium

KIC- $Kras^{LSL-G12D/+}$; $Ink4a^{fl/fl}$; $Ptf1a^{Cre/+}$

$KPten^{\Delta Acinar}$ PDAC cell lines- PDAC cell lines with $Kras^{G12D}$ and loss of *Pten* in the acinar origin

$KPten^{\Delta Acinar/\Delta Acinar}$- $Ptf1a^{CreER}$; $Kras^{LSL-G12D}$; $Pten^{flox/flox}$; $R26R^{LSL-YFP}$

$KPten^{\Delta Acinar/+}$- $Ptf1a^{CreER}$; $Kras^{LSL-G12D}$; $Pten^{flox/+}$; $R26R^{LSL-YFP}$

$KPten^{\Delta Duct}$ PDAC cell lines- PDAC cell lines with $Kras^{G12D}$ and loss of *Pten* in the ductal origin

$KPten^{\Delta Duct/\Delta Duct}$- $Sox9^{CreER}$; $Kras^{LSL-G12D}$; $Pten^{flox/flox}$; $R26R^{LSL-YFP}$

$KPten^{\Delta Duct/+}$- $Sox9^{CreER}$; $Kras^{LSL-G12D}$; $Pten^{flox/+}$; $R26R^{LSL-YFP}$

Kras- Kirsten rat sarcoma viral oncogene homolog

KPC- $Kras^{G12D}$; $Trp53^{R172H/+}$; $Pdx1^{Cre}$

LAL- limulus amebocyte lysate

LSL- loxp-stop-loxp

Lyve1- lymphatic vessel endothelial hyaluronan receptor 1

M-CSF- macrophage colony-stimulating factor

MCN- mucinous cystic neoplasia

Mki67- marker of proliferation ki-67

Mrc1 (CD206)- mannose receptor c-type 1

NC- negative control

NDS- normal donkey serum

NF-κB- nuclear factor kappa B

Nfkbia- NFKB inhibitor alpha

P-EMT- partial EMT

PanIN-pancreatic intraepithelial neoplasia

PB-IPMN- pancreatobiliary IPMN

PBS- phosphate buffered saline

PCA- principal component analysis

PD-L1 (*Cd274*)- programmed death-ligand 1

PDAC- pancreatic ductal adenocarcinoma

PDX1- pancreatic and duodenal homeobox 1

PI3K- phosphoinositide 3-kinase

PIP3- phosphatidylinositol (3,4,5)-trisphosphate

Pre-IPMN- microscopic IPMN

PTEN- phosphatase and tensin homolog

Ptf1a- pancreas transcription factor 1 subunit alpha

qPCR- quantitative polymerase chain reaction

RNA-seq- RNA-sequencing

Saa3- serum amyloid A-3

scBasal- single-cell basal

scClassical- single-cell classical

scIC- single-cell intermediate co-expressing

scRNA-seq- single-cell RNA-sequencing

SEM- standard error of the mean

SMAD4- mothers against decapentaplegic homolog 4

Socs3- suppressor of cytokine signaling 3

STAT3- signal transducer and activator of transcription 3

STAT5- signal transducer and activator of transcription 5

STI- soybean trypsin inhibitor type I

SWI/SNF- SWItch/Sucrose non-fermentable

TAMs- tumor associated-macrophages

Tbp- TATA-binding protein

Tgf-β- transforming growth factor beta

TIGIT- T cell immunoreceptor with Ig and ITIM domains

Tlr4- toll-like receptor 4

TME- tumor microenvironment

TP53 (Trp53)- tumor protein p53

Tregs- regulatory T cells

VEGF- vascular endothelial growth factor

YFP- yellow fluorescence protein

Acknowledgements

I would like to first express my thanks and gratitude to Dr. Janel Kopp and Dr. James Johnson, who provided this opportunity for me to learn and carry out an independent research project that challenged my critical thinking and scientific skills. I am especially grateful for the guidance, support, and challenge Dr. Janel Kopp provided during these two years to help me become a better scientist. I will carry what I learned with me for the rest of my life.

Secondly, I would like to thank my committee members Dr. Kenneth Harder and Dr. Pauline Johnson for their valuable suggestions on my thesis project. Their helpful immunology advice was what made my research project possible, and as someone without background in immunology I have learned so much in these past two years about the first responders in our body.

Thirdly, I would like to thank all the lab members in the Kopp lab and the Johnson lab for their professional and emotional support throughout my Master program. Without them I wouldn't be at where I am today, finishing up my Master thesis and writing up a manuscript for publication. Their invaluable friendship taught me there is more to being a scientist than just bench work and pipetting.

Last but not the least, I would like to thank my parents, who supported my decision not pursue a Ph.D. Degree and supported me through my hardship in their own ways. Their decision to send me study abroad all those years ago has given me the opportunity to pursue my dream and fulfill my potential, for that I am forever grateful.

Dedication

I dedicate this thesis to Andrew, who showed me the beauty at the bottom of a chasm and shone light into the abyss.

Chapter 1: Introduction

1.1 Pancreatic ductal adenocarcinoma (PDAC)

Pancreatic ductal adenocarcinoma (PDAC), the primary cancer of the pancreas (Kleeff et al., 2016), is a devastating disease with an overall 5-year survival rate of merely 10% due to poor prognosis and lack of effective treatment (Siegel et al., 2021). PDAC is thought to arise from three non-invasive premalignant lesions: microscopic pancreatic intraepithelial neoplasia (PanIN), macroscopic intraductal papillary mucinous neoplasia (IPMN), and mucinous cystic neoplasia (MCN) (Riva et al., 2018). With its increasing incidence but limited progress in developing new treatments, the mortality rate of pancreatic cancer has remained relatively similar for decades. In addition, it is projected to be the third leading cause of cancer-related death in Canada by Brenner et al. (Brenner et al., 2020). A lack of symptoms or biomarkers in the early stages of the cancer's development, as well as drug resistance, all contribute to the poor treatment outcomes of pancreatic cancer (Murakami et al., 2019). In addition, clinical studies reveal that PDAC is a molecularly heterogeneous disease, causing the diverse symptoms and sensitivity to treatment between different patients (Juiz et al., 2019). Therefore, understanding the heterogeneity and carcinogenesis of PDAC is crucial for developing early detection methods and more effective treatments. The PDAC heterogeneity can be defined by different genetic alterations, molecular subtypes, precancerous lesion types, cellular origins, and/or immune landscapes (Connor & Gallinger, 2022; Karamitopoulou, 2019; Patil et al., 2021). Each of these potential contributors to PDAC heterogeneity will be discussed in detail in the following sections.

1.2 Genetics basis of PDAC

Four main genetic mutations are associated with the formation of PDAC (Rhim & Stanger, 2010). Mutations in *KRAS* are recognized as the primary genetic event in the initiation and growth of PDAC, where nearly 95% of human PDAC harbor mutationally activated *KRAS* (Bryant et al., 2014). Contrary to common belief, oncogenic KRAS is not constitutively active, and even normal healthy people have cells bearing oncogenic Ras mutations (Huang et al., 2014). Instead, oncogenic KRAS requires upstream stimulants, such as pro-inflammatory molecules, to enhance and prolong its activation (Daniluk et al., 2012). The other mutations commonly observed in clinical PDAC samples occur in tumor suppressor genes, such as *TP53*, *CDKN2A*, and *SMAD4.* These genes also contribute to the heterogeneity of this disease (Grant et al., 2016). In addition, aberrant activation of the PI3K–AKT pathway has been widely implicated in human cancers, including PDAC (Pulido, 2018). In the PI3K-AKT pathway, the PTEN tumor suppressor dephosphorylates the PI3K product PIP3, and thus negatively regulates PI3K signaling. It has been reported that up to 70% of pancreatic cancer cell lines or tumor tissues have a decrease or loss of PTEN expression (Asano et al., 2004; Ying et al., 2011). PI3K signaling is one of the major KRAS effector pathways, and it has been shown to engage with $Kras^{G12D}$ to form precursor lesions and PDAC (Eser et al., 2014; Ying et al., 2011). Indeed, Kopp et al. demonstrated that reducing *Pten* expression in combination with activation of $Kras^{G12D}$ synergistically promoted the formation of precursor lesions and progression of IPMN to invasive PDAC (Kopp et al., 2018), confirming the positive crosstalk between these two pathways in tumorigenesis.

1.3 PDAC molecular subtypes

In the past decade, many studies have used next-generation sequencing to characterize the transcriptomic landscape of PDAC (Aguirre et al., 2018; P. Bailey et al., 2016; Chan-Seng-Yue et al., 2020; Collisson et al., 2011; Moffitt et al., 2015). The consensus from these studies of human PDAC is that there are two broadly defined subtypes: the classical or basal subtype (Martens et al., 2019). Classical tumors are often well differentiated, whereas basal tumors are often poorly differentiated. In terms of survival, patients with basal-like PDAC tend to have a lower disease-free and overall survival compared to patients with classical-like PDAC (Martens et al., 2019). However, these previous studies utilized bulk RNA-sequencing that treated a piece of tumor as one sample (Aguirre et al., 2018; P. Bailey et al., 2016; Chan-Seng-Yue et al., 2020; Collisson et al., 2011; Moffitt et al., 2015), making the study of intratumoral subtype heterogeneity difficult. More recently, Raghavan and colleagues utilized single-cell RNA-sequencing (scRNA-seq) on patient metastatic tumor biopsies and discovered an intermediate PDAC molecular subtype that expressed gene signatures associated with both basal and classical subtype tumors (Raghavan et al., 2021). In addition, Raghavan et al. also demonstrated the plasticity of PDAC subtypes, because they found that cells changed their transcriptional phenotype in response to the signals from the microenvironment. As a result, PDAC molecular subtypes might be more fluid and complicated than previously thought, potentially contributing to intratumoral, as well as intertumoral, tumor heterogeneity (Raghavan et al., 2021).

1.4 PanIN vs. IPMN

As mentioned previously, both PanIN and IPMN are precursor lesions of PDAC. The major difference between these two precursor lesions is their size, where PanIN is defined as a

microscopic (usually <0.5cm) flat or papillary lesion, while IPMN is macroscopic lesion (usually >1cm) typically with papillary epithelial protrusions and abundant mucin production (Basturk et al., 2015; M Distler et al., 2014). Both lesion types can be classified as low-grade to high-grade (Figure 1.1), but IPMN can be further classified into four histological subtypes, namely the intestinal, pancreatobiliary, oncocytic, and gastric subtypes (Basturk et al., 2015; M Distler et al., 2014). While very similar gene mutations are found in PanIN and IPMN, notable differences have been detected. Specifically, activating mutations in *GNAS* have been shown to be more prevalent in IPMN compared to PanIN. However, its occurrence is more common in intestinal and gastric IPMN subtypes, whereas *KRAS* mutations are more prominent in pancreatobiliary and gastric IPMN and almost absent in oncocytic IPMN (Basturk et al., 2015; M Distler et al., 2014). Other genetic mutations that are more prevalent in IPMN compared to PanIN include *RNF43*, *BRG1*, and *PIK3CA* (Dal Molin et al., 2012; Noë et al., 2020). The importance of these mutations for IPMN development have been supported by studies in genetically engineered mouse models bearing those genetic changes in the pancreas (Hosein et al., 2022; Kopp et al., 2018; von Figura et al., 2014).

In terms of overall prognosis, patients with IPMN-associated PDAC had better progression free survival and overall survival compared to patients with PanIN-associated PDAC (McGinnis et al., 2020). However, studies suggest subtypes of IPMN have independent prognostic values. For example, the 5-year survival of patients with intestinal IPMNs was found to be significantly better than patients with pancreatobiliary IPMNs. In addition, the pancreatobiliary subtype was strongly associated with malignancy and recurrence, and the long-term survival of patients with pancreatobiliary IPMN was comparable with that of PDAC patients without IPMN (Marius

Distler et al., 2013). Both pancreatobiliary and gastric IPMNs form tubular carcinoma, which have a poorer outcome compared to patients with oncocytic or colloid (formed from intestinal IPMN) carcinoma (Mino-Kenudson et al., 2011). In sum, the types of precursor lesions and even the subtypes of IPMN contribute to patient heterogeneity, as they are different at a molecular and histological level and are associated with different prognostic outcomes.

1.5 Cellular origin and PDAC tumorigenesis

Another potential contribution to the heterogeneity of PDAC is its cellular origin (Patil et al., 2021). In the pancreas, there is an endocrine and exocrine component. Both acinar cells and ductal cells make up the exocrine part of the pancreas, where PDAC usually arises (Rhim & Stanger, 2010). Acinar cells are exocrine cells that secrete digestive enzymes, whereas ductal cells make up the ductal structures that carry the digestive enzymes to the duodenum (Figure 1.2). Despite decades of research on PDAC pathogenesis, the exact lineage of the cellular origin of PDAC remains unclear and the cells capable of giving rise to PDAC are controversial. Due to the ductal morphology of most cases of PDAC, ductal cells were originally thought to be the cell of origin for PDAC (Storz & Crawford, 2020). However, recent evidence suggests that both acinar and ductal cells are capable of transformation and progression to PDAC in response to different genetic abnormalities (J. M. Bailey et al., 2016; Ferreira et al., 2017; Kopp et al., 2018; Lee et al., 2019; von Figura et al., 2014). Studies show that acinar cells are more sensitive to *KRAS* mutation than ductal cells and can undergo acinar-to-ductal metaplasia (ADM) to effectively develop PanIN and eventually PDAC (Gidekel Friedlander et al., 2009; Habbe et al., 2008; Kopp et al., 2012). Although ductal cells are more resistant to the $Kras^{G12D}$ mutation, many studies using mouse models have demonstrated that with combination of $Kras^{G12D}$ and

other tumor suppressor gene losses, ductal cells could readily form PanIN or IPMN and eventually progress to form PDAC (J. M. Bailey et al., 2016; Ferreira et al., 2017; Kopp et al., 2018; Lee et al., 2019; Roy et al., 2015; von Figura et al., 2014). However, this tumorigenesis process is different compared to how PDAC arises from acinar cells. Some of the major mouse models that show how cellular origin affects tumorigenesis are discussed below.

1.5.1 Ductal cells require complete loss of *Trp53* function to develop PDAC

Mutations in *TP53* are one of the most commonly found mutation in human PDAC samples after *KRAS* mutations (Waddell et al., 2015). The earliest and also most widely used mouse model with *Trp53* mutation is the "KPC" mouse model that Hingorani et al. developed in 2005 (Hingorani et al., 2005). In this model, mice expressed the $Kras^{G12D}$ and $Trp53^{R172H/+}$ gain-of-function mutation (Lang et al., 2004) from alleles recombined by the *Pdx1-Cre* at an embryonic stage. The KPC mice recapitulated many clinical histopathological features and were able to develop PanIN and subsequently PDAC by 16-week of age (Hingorani et al., 2005). However, during embryonic development, *Pdx1* is expressed by early pancreatic progenitor cells that contribute to all the cell lineages in the pancreas, including both acinar and ductal cells (Magnuson & Osipovich, 2013). As a result, using embryonically activated *Pdx1-Cre* does not allow researchers to study the effect of cellular origin on PDAC tumorigenesis. On the other hand, in adult mice the expression of *Ptf1a* or *Sox9,* for example, is primarily in acinar or ductal cells, respectively. This allows researchers to replace the *Pdx1-Cre* allele with cellular-type-specific Cre allele drivers to study how different mature cell types give rise to PDAC (Magnuson & Osipovich, 2013). As a result, more recent efforts have been made to generate mouse models with inducible Cre drivers that are cellular origin specific (Xu et al., 2019). For example, Bailey

et al. aimed to investigate the cell of origin specific effects of the *Trp53*$^{R172H/+}$ mutation by producing mouse models with a tamoxifen inducible-Cre expressed using a specific cell of origin promotor (J. M. Bailey et al., 2016). Specifically, *Mist1-CreER* was used to target recombination to adult acinar cells, and *Hnf1b-CreER* was used to target recombination to adult ductal cells. In the case of *Kras*^{G12D}-expressing acinar cells, expression from one *Trp53*^{R172H} allele enabled transformation of acinar cells to PanIN and subsequently PDAC as early as 2 months post-injection of tamoxifen. Ductal cells were not affected by the presence of a single mutant *Trp53* allele, but the presence of 2 *Trp53*^{R172H} alleles was sufficient to induce PDAC development from *Kras*^{G12D}-expressing ductal cells by as early as 2.5 months post-injection. These data demonstrated that ductal cells appeared to be unaffected by expression of one copy of the mutant *Trp53* allele, and this suggested that PDAC formed in the KPC model was mainly derived from acinar cells.

In addition to the gain-of-function *Trp53* mutation, Lee at al. used the *Ptf1a*^{CreER} or *Sox9CreER* drivers to induce *Kras*^{G12D} expression and homozygous loss of *Trp53* alleles at 3-4 weeks of age in adult acinar or ductal cells, respectively (Lee et al., 2019). High-grade PanIN and PDAC formed from both cells of origin, however ductal cells developed a smaller number, but higher-grade of PanIN, that progressed to form invasive PDAC faster than acinar cells. In addition, acinar-cell-derived tumors also had higher prevalence of mucinous glandular features compared to ductal-cell-derived tumors, indicating the tumorigenesis process between acinar- and ductal-cell-derived PDAC in these models was fundamentally different, and that cell of origin can have an impact on tumor phenotype.

1.5.2 Loss of *Brg1* plays a context-dependent role on the tumorigenesis of IPMN and PanIN

Brg1 is part of the chromatin-remodeling SWI/SNF complexes. *Brg1* inactivating mutations and deletions have been found in human PDAC, with its expression frequently reduced or lost in human IPMN samples (Dal Molin et al., 2012; Shain et al., 2012). Figura et al. used embryonically active *Ptf1a-Cre* to induce $Kras^{G12D}$ expression and homozygous loss of *Brg1*, and found mice developed cystic neoplastic lesions that resembled human pancreatobiliary IPMN that progressed to form PDAC (von Figura et al., 2014). In addition, the IPMN-PDAC developed with shorter latency but were less lethal and proliferative than PanIN-PDAC derived from mice with $Kras^{G12D}$ expression and heterozygous loss of *Trp53* (von Figura et al., 2014). Further study suggested that adult ductal cells in the context of $Kras^{G12D}$ and *Brg1* loss initiated IPMN-like lesion formation (von Figura et al., 2014). Mechanistically, they found that *Brg1* suppressed the dedifferentiation that preceded neoplastic transformation in mature ductal cells but promoted tumorigenesis after tumors formed by supporting a mesenchymal-like transcriptional landscape (Roy et al., 2015; von Figura et al., 2014). On the other hand, *Brg1* was necessary for PanIN initiation and progression to PDAC through positively regulating *Sox9* expression in adult acinar cells, indicating how adult acinar and ductal cells respond differently to the same mutation changes (Tsuda et al., 2018).

1.5.3 Ductal cells form PDAC in a PanIN-independent manner after loss of *Fbw7*

F-box and WD repeat domain-containing 7 (*FBW7*) is the substrate recognition component of the Skp1-Cul1-F-box ubiquitin ligase complex. Genomic deletion or mutation of *FBW7* has frequently been identified in many human cancers, and low protein expression commonly occurs

in human PDAC samples (Ji et al., 2015). Ferreira et al. found that embryonic deletion of *Fbw7* in combination with $Kras^{G12D}$ expression resulted in hyperplastic ducts as early as postnatal day 0 (at birth), and the formation of dysplastic lesions by postnatal day 7 (Ferreira et al., 2017). Further study utilizing adult ductal and acinar cell-specific CreER drivers found that while activation of KRAS and loss of *Fbw7* in adult acinar cells induced PanIN-dependent PDAC transformation, the same genetic change in adult ductal cells resulted in PDAC development in a low-grade PanIN independent manner (Ferreira et al., 2017). In addition, precursor lesions found in the ductal cell model were not IPMN, but a non-mucinous dysplasia that quickly induced in situ carcinoma, indicating different genetic mutation backgrounds also play a role in determining ductal cell-derived precursor lesion phenotype (Ferreira et al., 2017; Lee et al., 2019; von Figura et al., 2014).

1.5.4 Ductal cells are more sensitive to loss of *Pten* and form IPMN as the precursor lesion

As mentioned previously, PTEN is a well-known tumor suppressor that plays critical roles in controlling the PI3K pathway, with its mutation commonly found in many types of cancers including PDAC (Pulido, 2018). Hill et al. first used *Pdx1-Cre* to induce $Kras^{G12D}$ and homozygous knockout of *Pten* at embryonic stage, but the mice rapidly formed PanIN with occasional invasive cancer and none of the mice survived beyond 3 weeks of age (Hill et al., 2010). In contrast, mice with only one copy loss of *Pten* and activation of *Kras* had a median survival of 3.5 months, and the tumorigenesis was associated with the formation of ADM and PanIN. These results suggest that the lesions formed in the *Pdx1-Cre* mouse model used in Hill et al. might be primarily derived from acinar cells. However, mice with only *Pten* deletion in the

pancreas resulted in ductal metaplasia that originated from centroacinar cells rather than the transdifferentiation of acinar cells (Stanger et al., 2005). As a result, utilizing a ductal and acinar cell specific Cre driver was needed to further investigate how adult ductal or acinar cells specifically responded to the loss of *Pten* with or without $Kras^{G12D}$ expression.

To further investigate the effect of *Pten* loss in adult acinar or ductal cells, Kopp et al. utilized the $Ptf1a^{CreER}$ and *Sox9CreER* drivers, respectively (Kopp et al., 2018). The authors found that homozygous loss of the *Pten* alleles without $Kras^{G12D}$ in the ductal cells was enough to predispose mice to form PanIN, as well as IPMN that were of either oncocytic or pancreatobiliary subtype. Interestingly, spontaneous *Kras* mutation was observed in IPMN mostly associated with the pancreatobiliary subtype. When expression of $Kras^{G12D}$ with loss of one or two copies of *Pten* was induced in ductal cells at 4 weeks of age, ductal cells readily formed PanIN, and pancreatobiliary or gastric IPMN in the common and/or main pancreatic ducts, with some invasive PDAC having loss of heterozygosity at the *Pten* locus in the *Pten* heterozygous model. In addition, the tumor latency of the *Pten* heterozygous mice with $Kras^{G12D}$ is shorter compared to mice with only homozygous loss of *Pten*, but longer compared to mice with $Kras^{G12D}$ and homozygous loss of *Pten*. In adult acinar cells, homozygous loss of *Pten* did not result in premalignant lesions by 13 months of age, indicating that adult ductal and acinar cells are not equally sensitive to *Pten* loss. Recently, Talbert and colleagues demonstrated that mice with $Kras^{G12D}$ and homozygous loss of *Pten* in adult acinar cells (designated as $KPten^{\Delta Acinar/\Delta Acinar}$ in our study) formed PanIN as precursor lesions, with an average survival of 107 days (Talbert et al., 2019). Mice with $Kras^{G12D}$ and heterozygous loss of *Pten* in adult acinar cells ($KPten^{\Delta Acinar/+}$) resulted in PanIN lesions, as well (Figure 1.3 A), but with almost the same

tumor latency as mice expressing only $Kras^{G12D}$ ($KPten^{+/+}$) in their acini (unpublished data from our laboratory). Histologically, we did not find any morphological differences between PDAC arising in the $KPten^{\Delta Acinar/\Delta Acinar}$ and $KPten^{\Delta Acinar/+}$ genotypes; however, their morphologies are different from PDAC derived from the $Kras^{G12D}$; $Pten^{\Delta Duct}$ ductal model as we previously described (Kopp et al., 2018). We observed tumors with intratumoral cystic dilations of varying size and occurring with gastric type epithelium in $KPten^{\Delta Acinar/+}$ pancreata, instead of the small gland-like structures we observed in the $Kras^{G12D}$;$Pten^{\Delta Duct}$ tumors (Figure 1.3 B) (Kopp et al., 2018). In addition, many intratumoral cysts in moderately and well differentiated tumors developed papillae (Figure 1.3 B, circled). These results further indicate that cellular origin has a significant impact on precursor lesion initiation and PDAC tumorigenesis in the context of identical genetic driver mutations, making it an important factor to consider when studying tumor phenotypes, clinical outcomes, and treatments.

1.6 PDAC immune microenvironment

The tumor microenvironment (TME) of pancreatic cancer, including cancer-associated fibroblasts, extracellular matrix, and various types of immune cells, participates in controlling tumor growth, invasion, and metastasis (Murakami et al., 2019). A tumor can be defined by its immunogenicity, namely the ability of a tumor to induce an immune response that can inhibit its growth. This can be contributed by both the antigen expression and antigen presentation of a tumor that can drive a response of the adaptive immune system (Blankenstein et al., 2012). An "immunogenic" tumor, such as melanoma, has a high mutation burden and can present mutated antigens that can be targeted by the adaptive immune system (Passarelli et al., 2017). An "non-immunogenic" tumor, such as PDAC, has significantly less somatic mutations that contribute to

the scarcity of mutated antigens (Brouwer et al., 2021), and dysfunctional/immature dendritic cells that could not facilitate antigen presenting to simulate the adaptive immune system (Hegde et al., 2020; Passarelli et al., 2017). In addition, PDAC TME is also immunosuppressive with increased infiltration of immunosuppressive cells such as tumor-associated macrophages, myeloid-derived suppressor cells, and regulatory T cells to hamper the activation and function of effector lymphocytes and facilitate host immune surveillance escape (Li et al., 2020). This immunosuppressive phenotype is one of the contributors to PDAC's poor response to immune-checkpoint inhibitor therapies that generally benefits other types of "immunogenic" cancers (Schizas et al., 2020). In addition, interpatient immune microenvironment heterogeneity also contributed to the ineffectiveness of clinically approved immunotherapy (Liudahl et al., 2021). Recently, Balachandran et al. found that pancreatic tumors with high neoantigen number and abundant CD8+ T cell infiltration are associated with longer patient survival, offering hope to utilize neoantigen-specific immunity to treat PDAC in selective patients (Balachandran et al., 2017).

Immune cells are present very early in PDAC tumorigenesis, with multiple cells types being detected surrounding precursor lesion, both IPMN and PanIN (Bernard et al., 2019; Clark et al., 2007; Hiraoka et al., 2006; Roth et al., 2020). The cells in the immune system can be sub-categorized into those involved in the innate immune system or the adaptive immune system. The innate immune system includes immune cells that are readily present and can be immediately recruited to site of infection to provide the first response (Inman et al., 2014). Macrophages are one type innate immune cell, and in adult hematopoiesis they are generated from common myeloid precursor cells derived from hematopoietic stem cells (Qualls & Murray,

2011) (Figure 1.4). Common myeloid precursor cells will then differentiate into monocytes, which travel in the blood and migrate into tissues and differentiate into macrophages (Figure 1.4). The differentiation of monocytes into macrophages is largely facilitated by cytokines such as macrophage colony-stimulating factor (M-CSF) (Qualls & Murray, 2011). Another source of macrophages, called tissue-resident macrophages, are derived from yolk sac progenitor cells early in embryogenesis, and unlike monocyte-derived macrophages, tissue-resident macrophages are long lived and capable of self-renewal (Davies et al., 2013) (Figure 1.4). In PDAC TME, the macrophages are called tumor-associated macrophages and they tend to have an immunosuppressive activity and promote tumorigenesis (Inman et al., 2014).

Unlike the first defense offered by the innate immune system; the adaptive immune system requires a longer time to become active through the antigen presenting process. However, this also makes the adaptive immune cells the most effective against neoantigen-bearing cells, such as cancer cells (Inman et al., 2014). CD8+ T cells and regulatory T cells are example cell types from the adaptive immune system. Both cell populations initially originate from a common lymphoid progenitor cell that differentiates from hematopoietic stem cells (Lewis & Blutt, 2019) (Figure 1.4). Common lymphoid progenitor cells will further migrate to the thymus for T cells to mature (Figure 1.4). In the thymus, through somatic recombination of the T cell receptor genes, CD3+ T cells further mature into CD3+ CD8+ T cells, which later become cytotoxic T cells. CD3+ T cells can also become CD3+ CD4+ T cells, which later become T helper cells that help coordinate the immune response by stimulating other immune cells; and CD3+ CD4+ CD25+ T cells, which later become regulatory T cells (Lewis & Blutt, 2019) (Figure 1.4). In the TME, during the early stages of tumor initiations, naïve T cells would be primed in the draining lymph

nodes by antigen presenting cells with immunogenic antigens from tumor cells, followed by their concomitant activation and migration to the TME (Gonzalez et al., 2018). In addition, CD4+ T helper cells help the further activation of the CD8+ T cells to cytotoxic lymphocytes and memory T cells (Borst et al., 2018). CD3+ CD4+ CD25+ T cells can also be derived from CD3+ CD4+ T cells directly (Lewis & Blutt, 2019). In PDAC, CD8+ T cells are often rare, and when present, not effective, whereas regulatory T cells exert an inhibitory effect on the CD8+ T cells and contribute to the immunosuppressive microenvironment of PDAC (Liudahl et al., 2021; Oleinika et al., 2013; Steele et al., 2020). The effects of CD8+ T cells, regulatory T cells, and tumor associated macrophages on the progression from pre-neoplastic lesions to PDAC are discussed further in the following sections.

1.6.1 Cytotoxic CD8+ T cells

As a member of the lymphoid cell population, the cytotoxic CD8+ T cell is one of the most powerful effectors of the adaptive immune system that mediates anti-tumoral effects (Raskov, Orhan, Christensen, et al., 2021). In analyses of a mouse model with embryonic $Kras^{G12D}$ mutation and in human PDAC samples, only a low level of CD8+ T cells were found at the PanIN and IPMN stage, and this infiltration decreased in the invasive lesions (Clark et al., 2007; Hiraoka et al., 2006; Roth et al., 2020). In addition, CD8+ T cells were more commonly found in the stromal compartment or in tertiary lymphoid structures that were not directly adjacent to tumor cells, again indicating their hindered infiltration (Ene-Obong et al., 2013; Liudahl et al., 2021; Roth et al., 2020; Stromnes et al., 2017). Although both CD8+ T cells and CD4+ T cells have been found in human PDAC, functional T cells with high expression of T cell receptor signaling and effector-related genes were rarely observed (Stromnes et al., 2017). Indeed, recent

publications found that CD8+ T cells in patients displayed an exhausted gene expression signature (*TIGIT*), which was more pronounced in advanced disease (Sivakumar et al., 2021; Steele et al., 2020). In addition, the spatial distribution of CD8+ T cells in PDAC also has important prognostic correlation, with CD8+ T cells in close proximity to PDAC cells correlating with increased overall survival (Carstens et al., 2017). In summary, the scarcity of effective CD8+ T cells and their relatively limited infiltration into the tumor contributes to an ineffective immune surveillance against PDAC.

1.6.2 Regulatory T cells (Tregs)

Expressing the transcription factor forkhead box P3 (FOXP3), Tregs suppress effector T cells by secreting immune-suppressive cytokines such as TGF-β, and inducing effector T-cell apoptosis by secreting cytotoxic enzymes such as granzyme B (Murakami et al., 2019). In addition, Tregs express immune checkpoint molecules, such as CTLA-4 and TIGIT, that could ultimately inhibit effector T cells function (Kurtulus et al., 2015; Oleinika et al., 2013; Sivakumar et al., 2021; Steele et al., 2020). Although they are necessary to suppress excessive immune responses to maintain normal immune homeostasis, Tregs are also involved in tumor development in various types of cancer (Ohue & Nishikawa, 2019). In contrast to CD8+ T cells, the infiltration of an active immunosuppressive Treg population is readily observed in clinical and mouse PanIN and IPMN, and the infiltration increased in PDAC (Clark et al., 2007; Hiraoka et al., 2006; Hosein et al., 2022; Liudahl et al., 2021; Roth et al., 2020; Sivakumar et al., 2021). Mechanistically, previous studies found that PDAC cells produced CCL5 and VEGF to promote recruitment of Tregs through CCR5 and neuropilin-1 (Fan et al., 2020). Clinically, low numbers of Tregs and high CD8+ T cell infiltration are associated with long-term survival in patients with PDAC after

pancreatectomy (Liu et al., 2016; Lohneis et al., 2017). In summary, the presence of immunosuppressive Tregs promotes the immune escape phenotype generally seen in PDAC TME.

1.6.3 Tumor-associated macrophages (TAMs)

The high infiltration of macrophages into the stroma of human and mouse precursor lesions and PDAC have been investigated previously (Clark et al., 2007; Liudahl et al., 2021; Roth et al., 2020). The macrophages infiltrating tumor are called tumor-associated macrophages (TAM). Recently, research from the DeNardo laboratory showed that macrophages in PDAC could be derived from both circulating monocytes and embryonically-established tissue-resident macrophages (Y. Zhu et al., 2017). In addition, tissue-resident-derived TAMs showed a more pro-fibrotic transcriptional profile that was distinct from monocyte-derived TAMs (Baer et al., 2022; Y. Zhu et al., 2017). Overall, TAMs regulate immunosuppression through secretion of immunosuppressive cytokines and chemokines, and by promoting Treg recruitment to block effector T cell proliferation (Lankadasari et al., 2019; Yamamoto et al., 2012). In addition, TAMs could express PD-L1 to induce CD8+ T cells exhaustion (Xiang et al., 2021), and the high infiltration of TAMs was shown to facilitate the exclusion of CD8+ T cells from PDAC in mouse model (Beatty et al., 2015b). Indeed, Liudahl et al. (2021) has recently demonstrated that a high intratumoral CD8+/CD68+ (human macrophage marker) ratio and the tumors being lymphoid rich was associated with a longer survival and better outcome in PDAC patients pre-surgically treated with chemotherapy and radiation therapy. These authors also argued that myeloid cells played a crucial role in the immunosuppression of CD8+ and CD4+ T cells, as most of the CD4+ T cells were senescent and non-tumor responsive and the CD8+ T cells were mostly exhausted

and not effective (Liudahl et al., 2021; Sivakumar et al., 2021; Steele et al., 2020). As a result, TAMs play an important role in facilitating the immunosuppressive PDAC TME, in additional to Tregs.

Macrophages can be activated with distinct activation states at a specific time that ranges on the spectrum from pro-inflammatory to anti-inflammatory, and this biological process is called macrophage polarization (Hosein et al., 2019; Rőszer, 2015; Xue et al., 2014). A pro-inflammatory dominant (M1-cell state) macrophage phenotype is usually associated with the removal of pathogens during infection; an anti-inflammatory dominant (M2-cell state) macrophage phenotype is usually associated with the wound healing process, which includes tissue remodeling, phagocytosis of dead cells, and the resolution of inflammation (Shapouri-Moghaddam et al., 2018). However, these beneficial effects of M2-like macrophages can be a double-edged sword, as the anti-inflammatory characteristics could result in an immunosuppressive and pro-tumoral phenotype that is typically observed in TAMs in cancers (Shapouri-Moghaddam et al., 2018). A list of M1-cell state and M2-cell state markers that can help define the polarization state of macrophages can be found in Table 1.1. Recent studies suggest that the polarization of macrophages allows them to express both pro-inflammatory and anti-inflammatory markers. Indeed, *in vivo* and *in vitro* TAMs showed not only a pro-tumoral phenotype but inflammatory signatures, as well (Hosein et al., 2019; Xue et al., 2014). Khabipov et al. (2019) and Boyer et al. (2022) recently showed that murine PDAC cell lines polarized macrophages towards a more pro-tumoral M2-like phenotype *in vitro*, indicating the predominant polarization state of TAMs that might be present in the PDAC TME.

In recent years, there has been an emerging interest in the incorporation of immunotherapy, such as an immune checkpoint inhibitor, into the treatment regimen for many solid tumors. However, clinical trials of immunotherapy in pancreatic cancer have uniformly been disappointing and may only benefit a small subset of patients. This could be potentially due to the fact that most patients lack the stimulated adaptive response to neo-antigens, and the immune microenvironment between patients is heterogeneous (Liudahl et al., 2021; Sivakumar et al., 2021; Steele et al., 2020). To develop more effective immunotherapy options for PDAC and selected patients that could benefit from immunotherapies, we need to have a better understanding of what causes the heterogeneity in PDAC immune microenvironment. Previous studies indicated that an "immune-escape" PDAC TME phenotype shows similarities with a more basal-like PDAC molecular subtype, whereas an "immune-rich" phenotype shows similarities with a more classical-like PDAC (P. Bailey et al., 2016; Collisson et al., 2011; Karamitopoulou, 2019; Moffitt et al., 2015; Wartenberg et al., 2018). In addition, Flowers and colleagues recently demonstrated that a ductal cellular origin is associated with a basal-like human PDAC phenotype, whereas an acinar cellular origin is associated with a classical-like PDAC (Flowers et al., 2021). These results suggest that the cellular origin of PDAC could potentially contribute to different immune microenvironment phenotypes. We previously demonstrated that mice expressing $Kras^{G12D}$ with reduced *Pten* in ductal cells developed IPMN and PDAC, and mice with the same genetic changes in the acinar cells developed PanIN and PDAC (Kopp et al., 2018; Talbert et al., 2019). Herein, we took advantage of these mouse models to investigate whether cellular origin and precancerous lesions influenced the presence of different immune cell types in the PDAC immune microenvironment. For my studies, I primarily focused on mice in which an oncogenic form of *Kras* was expressed and one copy of the *Pten* locus was deleted specifically in ductal cells (*Sox9CreER*) or acinar

cells (*Ptf1a*^{CreER}). In these models, precancerous lesions formed gradually over time, likely through acquisition of secondary mutations or epigenetic changes and subsequently progressed to form primary tumors in a stochastic fashion. I specifically chose models with a longer latency and more stochasticity to more closely adhere to the events occurring during PDAC development in humans (Kopp et al., 2018).

1.7 Hypothesis

I hypothesize that *Kras*^{G12D} expression and loss of *Pten* in adult ductal or acinar cells will result in different immune cell infiltration and phenotypes in the precursor lesions and PDAC.

1.8 Objective

To investigate the immune microenvironment surrounding precursor lesions and PDAC derived from an acinar or ductal origin, we examined cell type-specific tamoxifen-inducible Cre-recombinase mouse models that have oncogenic *Kras*^{G12D} mutations and heterozygous or homozygous loss of *Pten* specifically in acinar (*KPten*$^{\Delta Acinar/+}$/ *KPten*$^{\Delta Acinar/\Delta Acinar}$, respectively) and ductal cells (*KPten*$^{\Delta Duct/+}$/ *KPten*$^{\Delta Duct/\Delta Duct}$, respectively) (Figure 1.5 A). The genetic changes in the acinar cell model were facilitated by the acinar cell expressed *Ptf1a*^{CreER}, whereas the changes in the ductal cell model were facilitated by the ductal cell expressed *Sox9CreER*. Mice were injected at 4-weeks-old with tamoxifen to induce recombination and were harvested at later timepoints when it was expected that pancreatic tumors had formed (Figure 1.5 A-B). PDAC cell lines were established from a few pancreatic tumors, and the rest were fixed for histological analysis (Figure 1.5 B). I used immunohistochemical staining against CD8, FOXP3, F4/80 to detect and quantify the immune infiltration of CD8+ T cells, Tregs, and macrophages,

respectively. In addition, we measured the distance between immune cells and the nearest ductal epithelium for CD8+ T cells and Tregs. I found that the immune cell infiltration and how it changes during tumorigenesis are different between the two cellular origin models starting at the precursor lesion stage. Specifically, PDAC derived from ductal cells tends to have more CD8+ T cell and Treg cell infiltration than those derived from acinar cells. Additionally, PDAC cells derived from ductal cells did not activate macrophages as much as the PDAC cells derived from the acinar cell model. This was, in part, due to the reduced expression of granulocyte-macrophage colony-stimulating factor (GM-CSF) in ductal cell-derived PDAC. With these studies we are beginning to understand how cellular origin shapes the immune microenvironment and its evolution throughout tumorigenesis. This could provide insight into the development of personalized immunotherapy, as the cellular origin of a patient's pancreatic tumor might offer insight into its unique immune microenvironment, making targeted immunotherapy more efficient and accurate.

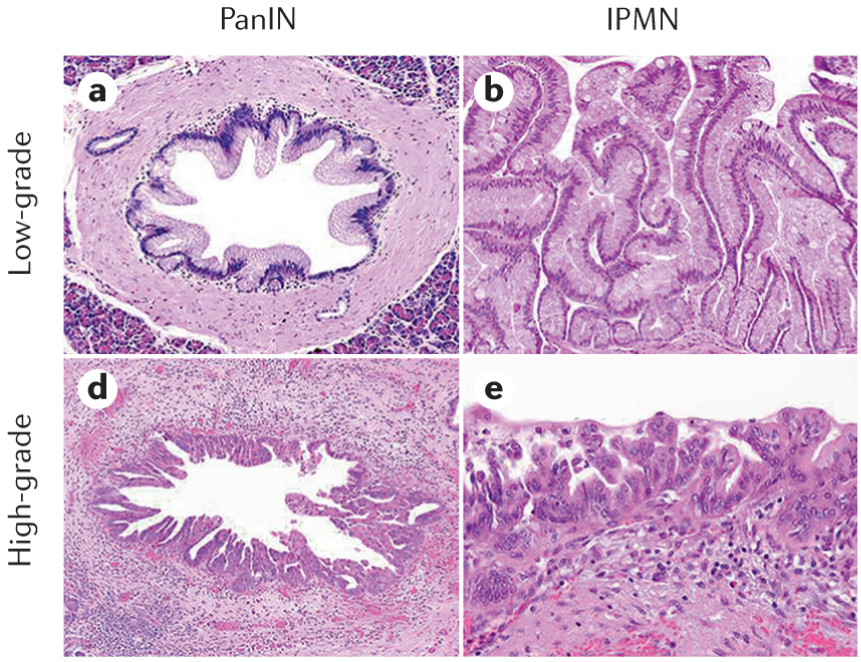

Figure 1.1 Histological difference between PanIN and IPMN.

Adapted from Singhi et al. Figure 1 (Singhi & Wood, 2021). Hematoxylin and eosin (H&E) stain showing low-grade and high-grade PanIN and IPMN. PanIN is <0.5 cm in size, whereas IPMN is >1 cm in size. Part a and d; magnification×20. Part b, e; magnification ×40.

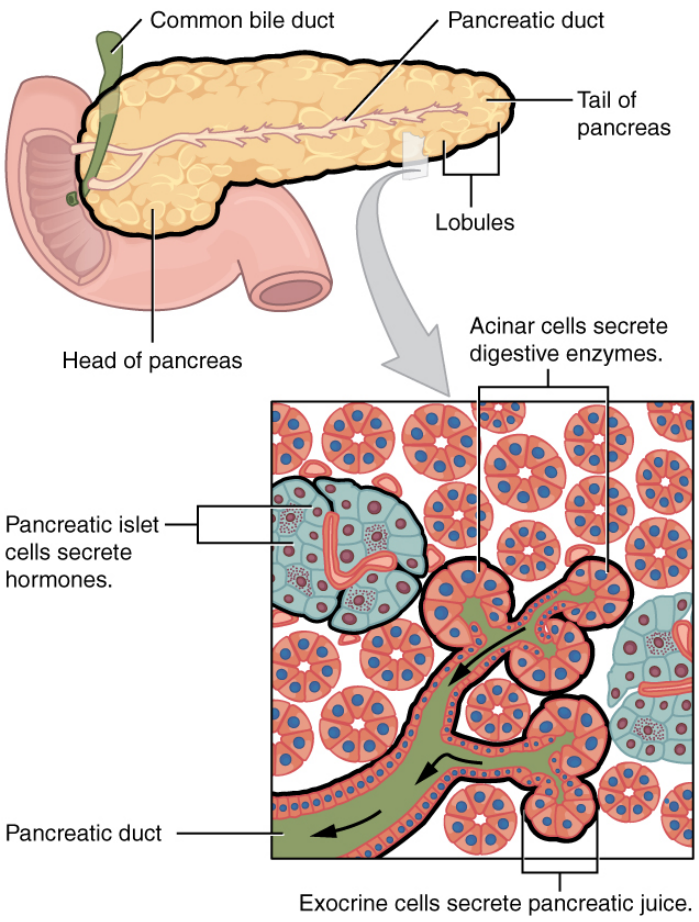

Figure 1.2 The pancreatic structures.

Adapted from Anatomy & Physiology, Connexions Web site. http://cnx.org/content/col11496/1.6/, Jun 19, 2013. The exocrine part of the pancreas consists of acinar cells and ductal cells. Acinar cells are exocrine cells that secret digestive enzymes, which will travel to the duodenum through the pancreatic duct made from ductal cells.

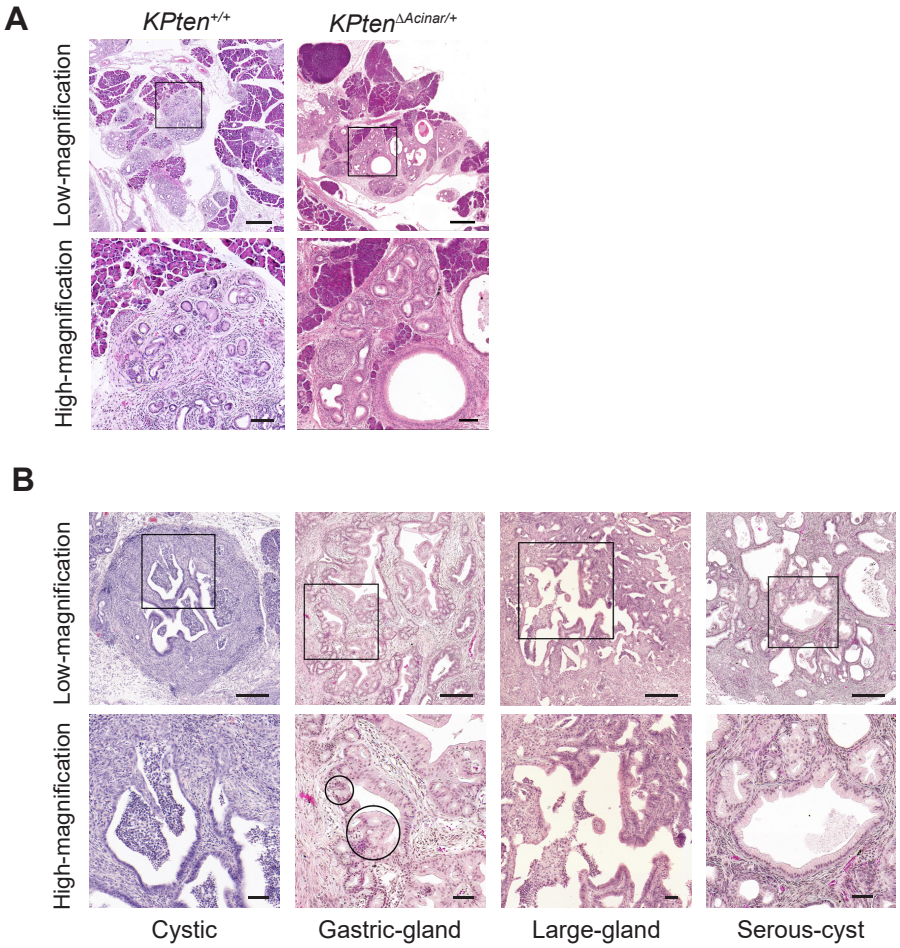

Figure 1.3 *KPten*$^{\Delta Acinar/\Delta Acinar}$ *and KPten*$^{\Delta Acinar/+}$ tumors histology.

(A) Low-magnification (top row) and high-magnification (bottom row) images of H&E staining of PanIN in *KPten*$^{+/+}$ mice and *KPten*$^{\Delta Acinar/+}$ mice.

(B) Low-magnification (top row) and high-magnification (bottom row) images of H&E staining of the different histological tumor phenotypes observed in *KPten*$^{\Delta Acinar/\Delta Acinar}$ and *KPten*$^{\Delta Acinar/+}$ mice. For high-magnification of gastric-gland image, circles show papillae in the gastric type epithelium. All phenotypes were observed in both genotypes.

Scale bars: 500 µm (A, top), 100 µm (A, bottom), 500 µm (B, top), 50 µm (B, bottom)

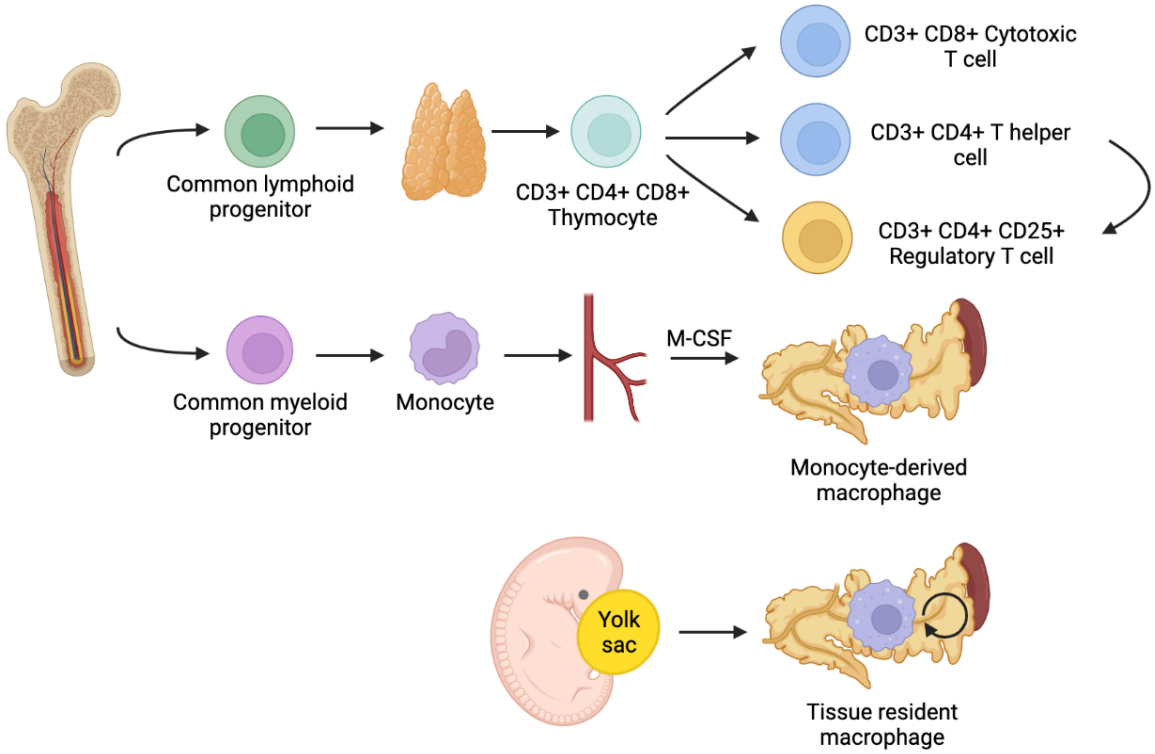

Figure 1.4 The differentiation of CD8+ T cells, CD4+ T cells, regulatory T cells, and macrophages.

A simplified diagram showing the differentiation of CD8+ T cells, CD4+ T cells, regulatory T cells, and macrophages through adult hematopoiesis from hematopoietic stem cell in the bone marrow. In addition to adult hematopoiesis, macrophages can also be differentiated from yolk sac progenitors during embryogenesis, and this macrophage population are called tissue resident macrophages.

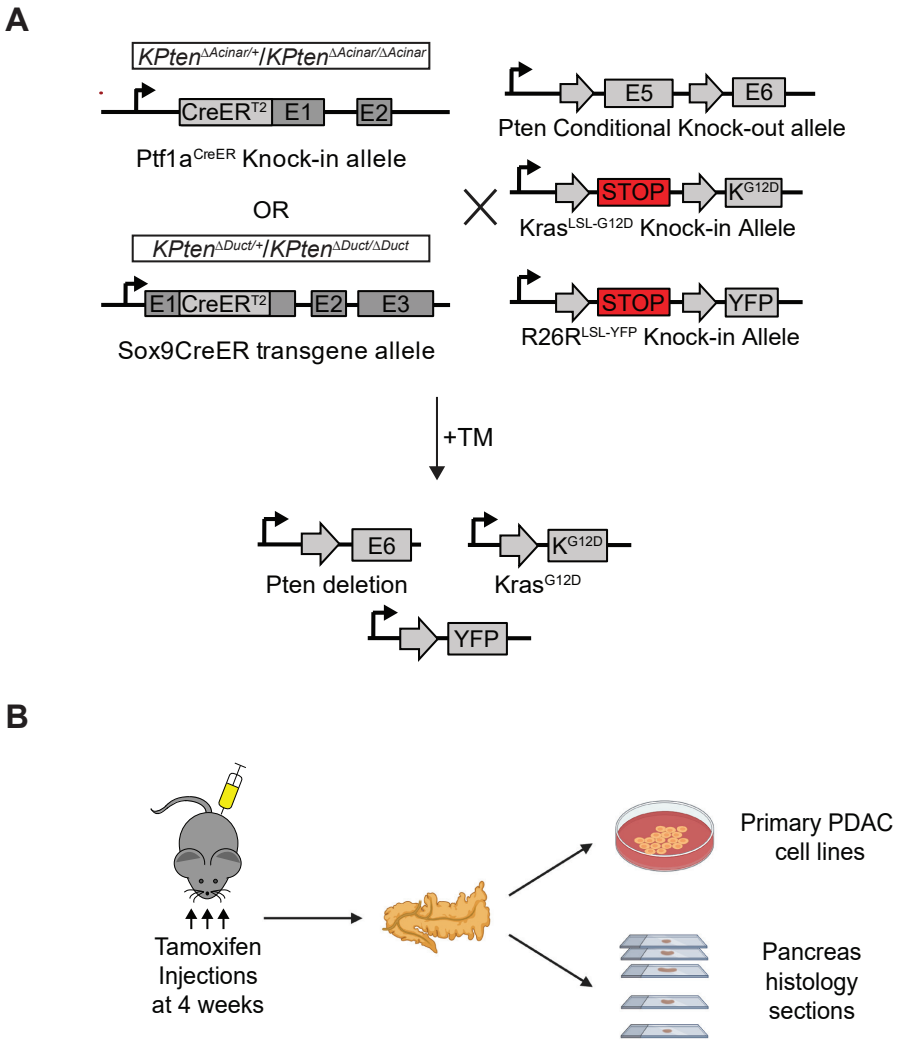

Figure 1.5 Schematic describing the alleles utilized to generate the mouse models and tissues used for this study.

(A) Schematic of the alleles in the *Ptf1a*^{CreER}*; Kras*$^{LSL\text{-}G12D}$*; Pten*$^{flox/+}$*; R26R*$^{LSL\text{-}YFP}$ (*KPten*$^{\Delta Acinar/+}$), *Ptf1a*^{CreER}*; Kras*$^{LSL\text{-}G12D}$*; Pten*$^{flox/flox}$*; R26R*$^{LSL\text{-}YFP}$ (*KPten*$^{\Delta Acinar/\Delta Acinar}$); and *Sox9CreER; Kras*$^{LSL\text{-}G12D}$*; Pten*$^{flox/+}$*; R26R*$^{LSL\text{-}YFP}$ (*KPten*$^{\Delta Duct/+}$), *Sox9CreER; Kras*$^{LSL\text{-}G12D}$*; Pten*$^{flox/flox}$*; R26R*$^{LSL\text{-}YFP}$ (*KPten*$^{\Delta Duct/\Delta Duct}$) mouse lines used in this study. Allele schematics reflect their composition before and after recombination induced by tamoxifen (TM) injection.

(B) Cre-mediated DNA recombination of $Kras^{LSL\text{-}G12D}$, $Pten^{flox/+}$, and $R26R^{LSL\text{-}YFP}$ alleles in *Ptf1a*- and *Sox9*-expressing cells was induced at 4 weeks of age with tamoxifen. Pancreata was harvested later for histology sections and/or creating primary PDAC cell lines.

M1-cell state macrophage markers	M2-cell state macrophage markers
iNOS, CD80, CD86, CD169, TLR2, TLR4, pSTAT1, TNF, IL6, IL1, IL23, CCL2, CCL5, IL12, CXCL8/9/10/11/16	Arginase, CD163, CD206, CD204, VEGF, IL10, CXCR1, CXCR2, CCL17/18/22/24

Table 1.1 M1- and M2- cell state specific markers.

Markers adapted from Ka et al. and Takeya and Komohara (Ka et al., 2014; Takeya & Komohara, 2016).

Chapter 2: Material and Methods

2.1 Mice

Sox9CreER (Font-Burgada et al., 2015), *Ptf1a*^{CreER}(Kopinke et al., 2012), *Pten*^{flox}(Lesche et al., 2002), *Kras*$^{LSL\text{-}G12D}$(Tuveson et al., 2004), and *R26R*$^{LSL\text{-}YFP}$(Srinivas et al., 2001) mice have been described previously and were maintained on a mixed C57BL/6 and CD1 background (Charles River Laboratories). 6-week-old C57BL/6J female mice were ordered from The Jackson Laboratory. Tamoxifen (Sigma-Aldrich) was dissolved in corn oil and administered subcutaneously at 5 mg per 40 g of body weight per injection. All described animal experiments were approved by the University of British Columbia and University of California, San Diego Animal Care and Use Committees.

2.2 Histology and immunohistochemical analysis

Paraffin-embedded sections were prepared and underwent immunohistochemical (IHC) stains as described previously (Lee et al., 2019; A. M. Y. Zhang et al., 2019). In short, sections were first deparaffinized and rehydrated through a series of xylene and ethanol incubation. Optional antigen retrieval was then performed on the rehydrated slides for each antigen staining according to Table 1. Slides were then quenched with 2% H_2O_2 solution in 1X phosphate buffered saline (PBS) (pH=7.4) for 15 mins at room temperature. Afterwards, slides were blocked with 5% normal donkey serum (NDS) in 0.1% Triton-X in 1X PBS (pH=7.4) for an hour at room temperature unless specified by the ImmPRESS® HRP Polymer Detection Kit (Vector Laboratories). Sections were then incubated overnight at 4˚C with primary antibodies. Biotinylated secondary antibodies were incubated with the sections at room temperature for an

hour before changing to VECTASTAIN Elite Avidin-biotin complex (Vector Laboratories) with two hours incubation at room temperature. Slides stained using ImmPRESS® HRP Polymer Detection Kit were incubated with ImmPRESS Polymer Reagents for 30 mins at room temperature instead. 3-3'-diaminobenzidine tetrahydrochloride (DAB) was used as the chromogen. Slides were counter stained with Mayer's hematoxylin (Sigma-Aldrich) and mounted with Cytoseal (Fisher). The mounted slides were then scanned using 3DHISTECH Panoramic MIDI slide scanner (3DHISTECH Ltd., Hungary). The primary and secondary antibodies used for IHC staining with antigen retrieval methods are listed in the Table 2.1. One section per mouse was used to do each IHC staining, as our sections are archive sections that are limited.

The distance of Tregs and CD8+ T cells distance to the nearest ductal epithelium was measured manually using the measuring annotation tool in Aperio ImageScope software (Leica Biosystems, Germany). All Tregs and CD8+ T cells infiltrating the stoma around each lesion were included in the analysis. The areas of interest surrounding every lesion in an entire pancreatic section of a mouse was classified and analyzed. The area of interest includes the immediate stromal structure that separated a particular lesion from another/ normal adjacent area. After creating a measuring annotation mark for the distance for all Tregs and CD8+ T cells within the area of interest, the Aperio ImageScope software would also provide a count of total annotations, hence the total number of infiltrating Tregs or CD8+ T cells for that area of interest. The infiltration density of Tregs or CD8+ T cells in each class of lesion was then calculated as the total number of infiltrating cells normalized to the pixel area occupied by the hematoxylin staining (all nuclei) within the area of interest. Pixel area was used instead of lesion area as

IPMN tend to be much bigger than PanIN with a lot of empty space inside. The microinvasion area near a IPMN or Pre-IPMN was counted as PDAC. 10-14 mice were analyzed for each genotype.

Macrophage infiltration was quantified by using the positive pixel count tool in Aperio ImageScope software. In short, fixed paraffin embedded mouse pancreatic sections were first stained for F4/80 antigen to visualize macrophages. An entire section for each slide was then assessed and annotated with areas of interest inclusive of ADM, PanIN, IPMN, Pre-IPMN, or PDAC. The infiltration density (%) of F4/80+ macrophages for each lesion category was expressed as the pixel area occupied by the DAB staining (F4/80+) normalized to the pixel area occupied by the DAB staining plus the hematoxylin staining (all nuclei). The infiltration density for each lesion category was then graphed as the average infiltration density of a specific type of lesion for the entire pancreatic section per mouse and 9-14 mice were analyzed for each genotype. CD206 staining positivity within PDAC in mice of different genotypes was quantified in the same way.

2.3 Primary PDAC cell culture

Primary mouse cell lines were established from PDAC harvested from $KPten^{\Delta Duct/+}$, $KPten^{\Delta Duct/\Delta Duct}$, and $KPten^{\Delta Acinar/+}$ mice (the PDAC cell lines derived from these mice are designated as $KPten^{\Delta Duct}$ and $KPten^{\Delta Acinar}$ PDAC cells) as previously described with slight modifications (Reichert et al., 2013). Briefly, 3-8 mm of tumor was minced with a razor blade or spring scissors and incubated in Dulbecco's modified Eagle's medium/Ham’s F-12

(DMEM/Ham's F-12; Corning) with 2.22 mg/mL collagenase B (Roche), 0.05 mM $CaCl_2$ and 0.02 mg/ml DNase I (Sigma-Aldrich) at 37°C for ~20 minutes. The digested tissue was collected by centrifugation at 1000 rpm for 5 min with soft deceleration and the supernatant was removed. The cell clumps were dissociated by 0.05% trypsin-EDTA (Corning) at room temperature for 5 minutes then the trypsin was inhibited by additional of 2 mg/ml soybean trypsin inhibitor (Sigma-Aldrich) and 2% Fetal Bovine Serum (FBS, HyClone) in 1X PBS (Lonza). The cells were washed three times with Hank's Balanced salt solution (HBSS; Lonza) containing 0.02 mg/ml DNase I. Finally, the cells were plated on a 2.31 mg/ml rat tail collagen type I (Corning) 2 mm thick gel and grown in pancreatic ductal cell medium as previously described (Reichert et al., 2013) with slight modifications: 0.25 mg/ml bovine serum albumin (VWR), 5 mg/ml D-glucose (VWR), 0.1 mg/ml soybean trypsin inhibitor type I (Sigma-Aldrich), 5 µl/ml insulin-transferrin-selenium (Gibco), 25 µg/ml bovine pituitary extract (Gibco), 20 ng/ml epidermal growth factor (Sigma-Aldrich), 5 nM 3, 3′, 5-triiodo-L-thyronine (Sigma-Aldrich), 1 µM dexamethasone (Sigma-Aldrich), 100 ng/ml cholera toxin (Sigma-Aldrich), 1.22 mg/ml nicotinamide (Sigma-Aldrich), 5% Nu-serum IV culture supplement (Corning), 0.5X penicillin/streptomycin (VWR), and 2.5 mg/ml fungizone (Life Technologies) in DMEM: Ham's F12 medium. Cells were grown in a humidified incubator at 37°C and 5% CO_2, refed every two days and passaged at ~80% confluency. In addition, polymerase chain reaction (PCR) was performed on cell lines to confirm recombination as described in Table 2.2.

To passage cells, the medium was aspirated and the collagen with adherent cells was digested by 2.22 mg/mL collagenase type XI (Sigma-Aldrich) solution and 0.02 mM $CaCl_2$ in warm DMEM: Ham's F12. The collagen gel typically disappeared after 12 minutes in the 37°C water bath. The

cell suspension was spun at 1500 rpm for 5 minutes and the supernatant was removed. The cells were dissociated by 0.05% trypsin-EDTA at room temperature for 5 minutes, followed by trypsin inhibition with 2 mg/ml soybean trypsin inhibitor in 2% FBS in 1X PBS. Cells were washed with HBSS four times by centrifuge and the cell pellet was resuspended in the pancreatic ductal cell medium and plated on collagen gels at a 1:3 split. For long-term preservation, primary PDAC cell lines were stored in 10% DMSO and 90% FBS in liquid nitrogen.

2.4 PDAC conditioned media generation

PDAC conditioned media from the cell line 367 (*KPten*$^{\Delta Duct}$) was generated using pancreatic ductal cell medium. Medium was refreshed when PDAC cells reached 50-60% confluence, and the conditioned media was harvested after 24 hrs, sterile filtered using Nalgene™ Rapid-Flow™ Vacuum Filter Units (Thermo Scientific), and aliquoted and stored at -80 °C. To generate conditioned media from PDAC cells ("Drop-out" media) to produce low baseline macrophage polarization background, the following components were removed from the "Complete" pancreatic ductal cell medium recipe: bovine serum albumin (BSA), soybean trypsin inhibitor type I (STI), insulin-transferrin-selenium (ITS), bovine pituitary extract (BPE), cholera toxin, and fungizone. The Nu-serum IV culture supplement concentration (using a batch with minimal endotoxin levels) was subsequently increased from 5% to 10% to compensate for the loss of BPE. *KPten*$^{\Delta Duct}$ (except 367) and *KPten*$^{\Delta Acinar}$ PDAC cells were cultured in this drop-out media for 5 passages and subsequently expanded into 3 10-cm cell culture dishes (Corning). Low-endotoxin PDAC conditioned media was harvested the same way as for the *KPten*$^{\Delta Duct}$ 367 cell line. Fresh Drop-out pancreatic ductal cell medium placed on collagen without cells for 24 hrs

was used as negative control for effect of the media alone on macrophage. It was aliquoted and stored at -80 ºC in a manner similar to the PDAC conditioned media.

2.5 RAW 264.7 cell culture and polarization

RAW 264.7 murine macrophages (ATCC, Manassas, VA, USA) were a generous gift from Dr. Lisa Osborne's Laboratory at UBC. RAW 264.7 cells were cultured in T-75 cell culture flasks (Thermo Scientific) at 37°C and 5% CO_2 in growth media made with 10% FBS and 1x penicillin/streptomycin (VWR) in Dulbecco's modified Eagle's medium (Gibco). Cells were passaged using 1x Versene (Gibco) according to manufacture protocol.

To expose RAW 264.7 murine macrophages to *KPten*$^{\Delta Duct}$ 367 conditioned media for the nitric oxide synthase and arginase activity assays, 4x10^6 cells were seeded into each T-75 flask using the following medias: 367 PDAC conditioned media was mixed with RAW 264.7 growth medium at a 2:3 ratio. To generate polarization controls, negative control pancreatic ductal medium (see above) was mixed with RAW 264.7 medium at a 2:3 ratio with a total volume of 8ml per T-75 flask. The M0 control was cultured in RAW 264.7 medium only. Negative control was cultured in the media mixture without any cytokine stimuli. For the M1 state control, 50 ng/ml of IFN-γ (STEMCELL Technologies) was added to the media mixture, and for M2 state control, 10 ng/ml of IL-4 (STEMCELL Technologies) and IL-13 (STEMCELL Technologies) were added to the media mixture. RAW 264.7 macrophages were cultured in these control medias and PDAC conditioned media for 24 hrs and then harvested for nitric oxide synthase and arginase activity assay.

To polarize RAW 264.7 murine macrophages with each Drop-out PDAC conditioned media, each drop-out media was mixed with RAW 264.7 medium at a 2:3 ratio. One million cells were seeded into each 6-well (Corning) with a total volume of 2 ml media mixture. The M0 control was used to assess the baseline state of the RAW 264.7 cells. RAW 264.7 macrophages were incubated for 24 hrs in the media and then collected for RNA isolation.

2.6 Limulus Amebocyte Lysate (LAL) assay

The LAL assay was conducted by using ToxinSensor™ Chromogenic LAL Endotoxin Assay Kit (Genscript) to measure endotoxin level according to the manufacture protocol. In short, each component in the pancreatic ductal medium was diluted to the concentration in the final medium and then subjected to the LAL assay. Colorimetric reading was performed using the TECAN Spark plate reader (TECAN). Endotoxin level was calculated as endotoxin unit (EU) per ml.

2.7 Arginase activity assay

The arginase assay was conducted by using the Arginase Activity Assay Kit (Sigma-Aldrich) according to the manufacture's protocol. In short, $1x10^6$ cells were lysed with 10 mM Tris-HCl (pH 7.4) containing 1X Halt™ Protease Inhibitor Cocktail (ThermoFisher) and 0.4% (w/v) Triton X-100 (Fisher Scientific), and a small aliquot of the cell lysate was used to perform the Micro BCA assay (Thermo Scientific) for protein concentration. Both assays were performed using clear 96-well plates (Corning), and colorimetric reading was performed using the TECAN Spark plate reader (TECAN). Arginase activity was calculated as mU per mg of total protein.

2.8 Nitric Oxide Synthase Assay

Nitric oxide synthase assay was conducted by using Nitric Oxide Synthase Activity Assay Kit (Abcam) according to the manufacture's protocol. In short, $3x10^6$ cells were lysed with NOS Assay Buffer containing 1X Halt™ Protease Inhibitor Cocktail (ThermoFisher), and a small aliquot of the cell lysate was used to perform the Micro BCA assay (Thermo Scientific) for protein concentration. Both assays used clear 96-well plates (Corning), and colorimetric reading was measured using TECAN Spark plate reader (TECAN). Nitric oxide synthase activity was calculated as mU per mg of total protein.

2.9 Cytokine array assay

Cytokine expression in *KPten*$^{\Delta Duct}$ or *KPten*$^{\Delta Acinar}$ PDAC cells conditioned media was measured by using Proteome Profiler Mouse Cytokine Array Kit, Panel A (R&D Systems) according to the manufacture protocol. Conditioned media from *KPten*$^{\Delta Duct}$ PDAC cell lines 409 and 746A, and *KPten*$^{\Delta Acinar}$ PDAC cell lines 321A and 339A were analyzed. An average integrated density of each cytokine from duplicated spots was calculated using ImageJ (U. S. National Institutes of Health).

2.10 Bone marrow-derived macrophages cell culture

Bone marrow-derived macrophages (BMDMs) were differentiated from bone marrow harvested from femurs of 6-11 week old C57BL/6J female mice, as previously described (Toda et al., 2021), with slight modifications. Female C57BL/6J mice were chosen for BMDM derivation as all PDAC cell lines in this study were derived from female mice. In short, bone marrow cells were flushed from both ends of a femur by using 25G needles (BD) with 10 ml of ice-cold

DMEM: Ham's F12 medium. Both femurs from each mouse were used, and each femur generated around 20-30 million bone marrow cells. After harvesting, bone marrow cells were seeded in T-175 cell culture flasks (Thermo Scientific) with a seeding density of $5x10^5$ cells per ml of BMDM medium and each flask had 20 ml. BMDM medium consists of 10% heat-inactivated low-endotoxin FBS (Hyclone) and 0.5x penicillin/streptomycin in DMEM: Ham's F12 medium. Mouse macrophage-colony stimulating factor (mM-CSF) (STEMCELL Technologies) was added to the culture medium fresh at a concentration of 50 ng/ml, and bone marrow cells were cultured at 37°C and 5% CO_2 for 7 days for BMDMs to differentiate. Fresh BMDM medium (20 ml) with 50 ng/ml mM-CSF was added to the culture on day 3 of differentiation. On day 6, 20 ml of culture medium was removed, then 20 ml fresh BMDM medium with 50 ng/ml mM-CSF was added to the culture. BMDM cells were harvested at day 7 using Accutase (Innovative Cell Technologies, Inc.) according to manufacturer's protocol.

2.11 BMDM cell culture in conditioned PDAC media

To assess the effects of PDAC-secreted factors on BMDMs, PDAC conditioned media was mixed with BMDM medium at a 2:3 ratio. To generate BMDM controls, negative control media was mixed with BMDM medium at a 2:3 ratio. M0 controls were cultured in BMDM medium without mixing with the negative control media. For M0 and negative control (NC), mM-CSF was added to the media mixture at 10 ng/ml as it plays an important role in macrophage survival (Otero et al., 2009). For M1 control, 50 ng/ml of IFN-γ was added to the media mixture, and for M2 control, 10 ng/ml of IL-4 and IL-13 was added to the media mixture. To neutralize GM-CSF/CCL5/CXCL12/M-CSF, anti-GM-CSF antibody (Invitrogen eBioscience; 16-7331-81),

anti-CCL5 antibody (R&D System; MAB478-100), anti-CXCL12 antibody (R&D System; MAB310-100), anti-M-CSF antibody (R&D System; MAB416-100), Rat IgG2a kappa isotype control antibody (Invitrogen eBioscience; 16-4321-81), or Rat IgG2b isotype control antibody (R&D System; MAB0061) was added to the PDAC conditioned media mixture at a concentration of 1 μg/ml (Guo et al., 2017; Huen et al., 2015; Sottnik et al., 2015). The media mixture was incubated with the antibodies with rocking at 4 ^{o}C for 1 hr prior to adding the media to the BMDMs. BMDMs were seeded at a density of $1x10^{6}$ cells per 6-well (Corning) with 2 ml of media mixture described above for 24 hrs. Three technical replicates (three 6-wells) were performed for each PDAC cell line. Afterwards, the media was aspirated, and the wells were washed with HBSS. RNA was harvested by adding 350 μl RLT buffer (Qiagen) directly to the wells.

2.12 RNA extraction and Quantitative real-time PCR analysis

RNA from cells was extracted using the RNeasy Mini Kit (Qiagen) and the RNA concentration was measured by the NanoDrop® ND-1000 UV-Vis Spectrophotometer (Thermo Scientific). cDNA was synthesized using the High-Capacity cDNA Reverse Transcription Kit (Thermo Fisher Scientific) and quantitative real-time PCR (qPCR) analysis was performed with 10 ng cDNA using the Power SYBR® Green PCR Master Mix kit (Applied Biosystems). The qPCR conditions were 95˚C for 10 min, 95˚C for 15s, and 60˚C for 60s, with the last two steps repeated for 39 cycles. The accumulation of double-stranded DNA was measured in real-time using the Bio-RadCFX384, C1000 Touch Thermal Cycler (Bio-Rad), and the fold change expression was calculated as $2^{-\Delta\Delta Ct}$ against negative control. Duplicates were performed for each sample in 384-well plate (Bio-Rad) to account for pipetting error. *Tbp* was used as housekeeping gene, and ΔCt

was calculated as the difference of Ct values between gene of interest and *Tbp*. The stability of *Tbp* was validated with RNA-seq data with a FPKM value of 9-10 for all groups. qPCR primer sequences can be found in Table 2.3.

2.13 RNA-sequencing and analysis

Bulk-RNA sequencing was performed by the BRC sequencing core. Sample quality control and quantity measurement were performed using the Agilent 2100 Bioanalyzer. Smples were then prepped following the standard protocol for the NEBNext Ultra II Stranded mRNA (New England Biolabs). Sequencing was performed on the Illumina NextSeq2000 with Paired End 61bp × 61bp reads. Sequencing data was demultiplexed using Illumina's bcl2fastq2.

RNA-sequencing preliminary analysis was performed by Dr. Stephane Flibotte using the previously described method (Vuilleumier et al., 2019). In short, the alignments to the transcriptome were performed by using STAR, HISAT2, kallisto, or Salmon aligners. Quantification of the reads was then performed directly with STAR, kallisto and Salmon or with RSEM and StringTie. In all cases, de-multiplexed read sequences were aligned to the Mus Musculus (mm10) reference genome sequences. In-house Perl scripts were used to sum all the read counts for all genes and comprise matrices for the gene read counts. Differential expression analysis was then performed on the data from those matrices using R package DESeq2 and edgeR and produced results from the total 10 pipelines. The output for each pipeline compiles a list of genes ranked by the P-value for differential expression after correction for multiple testing with a significant cut-off value of $p<0.05$. A combined list of genes was obtained with the 10

pipelines and genes with a significance of $p<0.05$ in at least half the pipelines were considered as differentially expressed and thus used in this study. Genes with an inconsistent differentially expression direction between pipelines were eliminated from the combined list. The kallisto-DESeq2 pipeline was used to make heatmaps, as it produced similar results with the combined list. Heatmaps were created with the R package pheatmap using the regularized log transformed data obtained with kallisto-DESeq2. Row means were subtracted to improve difference in visualization.

To compare our PDAC cell lines with those in Aiello et al. (Aiello et al., 2018), the principal component analysis (PCA) eigenvectors were first calculated with the prcomp R using only the samples in Aiello et al., then the location of the five PDAC cell lines in this study was calculated using those eigenvectors. The plots were done using ggplot2 in R. To create KIC macrophage pseudo bulk-RNA-sequencing data from the scRNA-seq data set in Hosein et al. (Hosein et al., 2019), Seurat was used to recreate the macrophage clusters reported in the original manuscript. The total counts for each gene that is unique to the KIC macrophage cluster were obtained with the aggregate function in R, which compiled all the counts for each gene in a specific cluster. Gene ontology pathway enrichment analysis was performed by using Enrichr (Xie et al., 2021).

2.14 Statistical analysis

Statistical parameters including the sample size n (number of animals or cell lines), mean ± standard error of the mean (SEM), and statistical significance are reported in the figure legends and figures. Parametric and non-parametric P values were calculated in GraphPad Prism 8.0 or Excel. GraphPad Prism was used to calculate the mean and SEM. $p<0.05$ was considered as

significant and asterisks denote statistical significance level (*, $p< 0.05$; **, $p<0.01$; ***, $p<0.001$; ****, $p<0.0001$).

Primary antibodies					
Antigen	Source	Catalog	Dilution	Species	Antigen retrieval
F4/80	Invitrogen eBioscience Thermo Fisher	14-4801-82	1:100	Rat	30s 0.4mg/ml proteinase K digestion or no antigen retrieval
FOXP3	Invitrogen eBioscience Thermo Fisher	14-5773-82	1:200	Rat	Low pH buffer 200mL 10mM citrate buffer at pH 6
CD8	Invitrogen eBioscience Thermo Fisher	14-0808-82	1:1000	Rat	Low pH buffer 200mL 10mM citrate buffer at pH 6
MMR/CD206	R&D Systems	AF2535-SP	1:1000	Goat	30s 0.4mg/ml proteinase K digestion or no antigen retrieval
Secondary antibodies					
Antigen	Source	Catalog	Dilution	Species	Used for which primary antibodies
Rat	Vector Laboratories	MP-7404-50	1:2	Goat	Used for CD8, FOXP3
Goat	Vector Laboratories	MP-7405-15	1:2	Horse	Used for CD206
Rat	Jackson ImmunoResearch laboratories, Inc.	712-065-150	1:1000	Donkey	Used for F4/80

Table 2.1 Primary and secondary antibodies used for IHC staining in this study.

Mouse allele	Primer name	Sequence (5'-3')	Product
Recombined *Kras*^{G12D}	Web1	GTCTTTCCCCAGCACAGTGC	Amplifies a ~650bp *Kras*^{G12D} and ~620bp wildtype band.
	Web2	CTCTTGCCTACGCCACCAGCTC	
Recombined *Pten*	PTEN6637-F #1294	TCCCAGAGTTCATACCAGGA	Amplifies a ~650bp Loxp band, a ~500bp wildtype band and ~300bp *Pten* knockout band.
	PTEN6925-R #1295	GCAATGGCCAGTACTAGTGAAC	
	PTEN7319-R #1296	AATCTGTGCATGAAGGGAAC	

Table 2.2 PCR primers sequences used for recombination analysis.

Gene name	Forward primer	Reverse primer
Tbp	5'-AGAACAATCCAGACTAGCAGCA-3'	5'-GGGAACTTCACATCACAGCTC-3'
Arg1	5'-TTGGGTGGATGCTCACACTG-3'	5'-GTACACGATGTCTTTGGCAGA-3'
Mrc1	5'-CTCTGTTCAGCTATTGGACGC-3'	5'-CGGAATTTCTGGGATTCAGCTTC-3'
Cd163	5'-GGTGGACACAGAATGGTTCTTC-3'	5'-CCAGGAGCGTTAGTGACAGC-3'
Il6	5'-CTGCAAGAGACTTCCATCCAG-3'	5'-AGTGGTATAGACAGGTCTGTTGG-3'
Nos2	5'-GTTCTCAGCCCAACAATACAAGA-3'	5'-GTGGACGGGTCGATGTCAC-3'
Tnf	5'-CCTGTAGCCCACGTCGTAG -3'	5'-GGGAGTAGACAAGGTACAACCC-3'
Cxcl10	5'-CCAAGTGCTGCCGTCATTTTC-3'	5'- GGCTCGCAGGGATGATTTCAA-3'
Cd86	5'-CTGGACTCTACGACTTCACAATG-3'	5'- AGTTGGCGATCACTGACAGTT-3'
Il10	5'-GCTCTTACTGACTGGCATGAG-3'	5'- CGCAGCTCTAGGAGCATGTG-3'
Tgfb	5'-CTCCCGTGGCTTCTAGTGC-3'	5'- GCCTTAGTTTGGACAGGATCTG-3'
Cxcr2	5'-ATGCCCTCTATTCTGCCAGAT-3'	5'-GTGCTCCGGTTGTATAAGATGAC-3'
Cd274	5'-TGCGGACTACAAGCGAATCACG-3'	5'-CTCAGCTTCTGGATAACCCTCG-3'
Ccl9	5'-CCCTCTCCTTCCTCATTCTTACA-3'	5'-AGTCTTGAAAGCCCATGTGAAA-3'
Csf2rb	5'-GTGGAGCGAAGAGTACACTTG-3'	5'-CCAAAGCGAAGGATCAGGAG-3'
Socs2	5'-AGTTCGCATTCAGACTACCTACT-3'	5'-TGGTACTCAATCCGCAGGTTAG-3'
Ccr1	5'-CTCATGCAGCATAGGAGGCTT-3'	5'-ACATGGCATCACCAAAAATCCA-3'
Ccl6	5'-GCTGGCCTCATACAAGAAATGG-3'	5'-GCTTAGGCACCTCTGAACTCTC-3'
Saa3	5'-TGCCATCATTCTTTGCATCTTGA-3'	5'-CCGTGAACTTCTGAACAGCCT-3'

Table 2.3 qPCR primer sequences used in this study.

Chapter 3: Cellular origin affects immune infiltration

Introduction

To test the hypothesis that the immune cell infiltrations are difference between acinar-cell- and ductal-cell-derived precancerous lesions and PDAC, I first conducted IHC on pancreatic histology sections to study the immune infiltration pattern and density of Tregs, CD8+ T cells, and macrophages.

3.1 *KPten*$^{\Delta Acinar/+}$ mice have more Tregs and CD8+ T cells at the precursor lesion stage, whereas *KPten*$^{\Delta Duct/+}$ mice are more enriched in those cell population at the PDAC stage.

To investigate the immune infiltration differences in *KPten*$^{\Delta Acinar/+}$ and *KPten*$^{\Delta Duct/+}$ mice, we used archived paraffin embedded pancreas histology sections generated from these mouse models (age 4-8 months for *KPten*$^{\Delta Duct/+}$ mice, age 7-18 months for *KPten*$^{\Delta Acinar/+}$ mice) and performed IHC staining using antibodies against immune cell populations that have the most prognostic value. The first two immune cell populations I investigated by IHC staining were Tregs and CD8+ T cells by using anti-FOXP3 or anti-CD8 antibodies, respectively (Figure 3.1 A-B). Both cell populations have prognostic value as low numbers of Tregs and high CD8+ T cell infiltration were associated with long-term survival in patients with PDAC after pancreatectomy (Liu et al., 2016; Lohneis et al., 2017). We first quantified the total number of cells surrounding or infiltrating into different types of morphological structures, specifically ADM, PanIN, microscopic IPMN (Pre-IPMN), IPMN, or PDAC. Overall, both immune cell populations had similar infiltration pattern between *KPten*$^{\Delta Acinar/+}$ and *KPten*$^{\Delta Duct/+}$ models. First, I found that the majority of Tregs and CD8+ T cells were present around ADM lesions in both *KPten*$^{\Delta Duct/+}$ and *KPten*$^{\Delta Acinar/+}$ mice, although the infiltration of these cells is higher in

KPten$^{\Delta Acinar/+}$ mice compared to *KPten*$^{\Delta Duct/+}$ mice (Figure 3.1A-B, Figure 3.2 A). In addition, in *KPten*$^{\Delta Duct/+}$ mice, there were significantly less Tregs and CD8+ T cells present surrounding pre-IPMN (FOXP3+: $7x10^{-6}$ cell count/negative pixel area (CN); CD8+: $3.5x10^{-6}$ CN) or IPMN (FOXP3+: $1.9x10^{-6}$ CN; CD8+: $1.8x10^{-6}$ CN) compared to ADM (FOXP3+: $2.6x10^{-5}$ CN; CD8+: $1.4x10^{-5}$ CN) (Figure 3.1 A-B, Figure 3.2 A). Interestingly, the number of FOXP3+ and CD8+ cells increased when the IPMN was associated with PDAC (FOXP3+: $5.8x10^{-6}$ CN; CD8+: $3.8x10^{-6}$ CN) (Figure 3.2 A). This is consistent with previous clinical observations that FOXP3+ cells are more prevalent in PDAC compared to IPMN (Hiraoka et al., 2006; Roth et al., 2020). In *KPten*$^{\Delta Acinar/+}$ mice, on the other hand, the number of these cell populations decreased from ADM (FOXP3+: $9.9x10^{-5}$ CN; CD8+: $4x10^{-5}$ CN) to PanIN (FOXP3+: $3.7x10^{-5}$ CN; CD8+: $1.5x10^{-5}$ CN) to PDAC (FOXP3+: $4.2x10^{-6}$ CN; CD8+: $1.7x10^{-6}$ CN) (Figure 3.1 A-B, Figure 3.2 A). This decrease in the CD8+ T cell population from PanIN to PDAC is consistent with previous mouse model and clinical studies (Hiraoka et al., 2006; Tiberti & Nezi, 2020). Overall, Treg and CD8+ T cell infiltration are significantly higher in PanIN in *KPten*$^{\Delta Acinar/+}$ mice compared to IPMN in *KPten*$^{\Delta Duct/+}$ mice (Figure 3.1 A-B, Figure 3.2 A). In addition, there are generally more Tregs and CD8+ T cells in *KPten*$^{\Delta Duct/+}$ PDAC compared to *KPten*$^{\Delta Acinar/+}$ PDAC.

Since the distance between CD8+ T cells and PDAC cells had prognostic value (Carstens et al., 2017), I decided to look at how close Tregs and CD8+ T cells were to the preneoplastic/neoplastic cells by measuring the distance between these immune cells to the nearest ductal epithelium. All values were shown in violin plot to demonstrate data distribution. In both *KPten*$^{\Delta Duct/+}$ and *KPten*$^{\Delta Acinar/+}$ mice the immune cells were further away from the tumor cells in PDAC compared those nearby IPMN or PanIN, respectively (Figure 3.1 A-B, Figure 3.2

B). In addition, Tregs and CD8+ T cells were closer to the preneoplastic cells in PanIN in *KPten*$^{\Delta Acinar/+}$ mice compared to IPMN in *KPten*$^{\Delta Duct/+}$ mice (Figure 3.1 A-B, Figure 3.2 B). These data suggest a potential trend that a higher number of immune cells infiltrating lesions is correlated to a shorter distance of the immune cells from the preneoplastic/neoplastic cells. Consistent with this trend, I also saw significantly shorter distance of Tregs and CD8+ T cells to the tumor cells in *KPten*$^{\Delta Duct/+}$ PDAC compared to *KPten*$^{\Delta Acinar/+}$ PDAC (Figure 3.1 A-B, Figure 3.2 B). Taken together, these data show that infiltration of both Tregs and CD8+ T cells decreased as PanIN progressed to become PDAC in *KPten*$^{\Delta Acinar/+}$ mice but increased as IPMN progressed to become PDAC in *KPten*$^{\Delta Duct/+}$ mice.

3.2 Macrophage infiltration differs at the precursor lesion level between *KPten*$^{\Delta Duct/+}$ and *KPten*$^{\Delta Acinar/+}$ mice.

In addition to CD8+ T cells and Tregs, I studied the infiltration of macrophages next, as they are one of the most abundant and investigated myeloid cell populations in the PDAC immune microenvironment (Beatty et al., 2015a; Liou et al., 2017; Tu et al., 2021; Yaqing Zhang et al., 2017; Y. Zhu et al., 2017). To look at the infiltration of macrophages, I did IHC staining against the F4/80 antigen. In *KPten*$^{\Delta Duct/+}$ mice, macrophage infiltration into the stroma was most abundant in ADM lesions and PDAC, but there were very few F4/80+ cells present in the stroma associated with PanIN, Pre-IPMN, and IPMN lesions (Figure 3.3 A). Interestingly, we found that macrophages tended to infiltrate the stalk of the IPMN where invasion of tumor cells into the stoma was apparent, rather than inside IPMN nodules (Figure 3.3 Ai, Aii). *KPten*$^{\Delta Acinar/+}$ mice on the other hand had uniformly high macrophage infiltration around precursor lesions and PDAC (Figure 3.3 B). To quantify the macrophages that were surrounding the precursor lesions and

PDAC, I quantified the average infiltration density of macrophages surrounding each lesion type. I found that the infiltration density of macrophages surrounding precursor lesions in *KPten*$^{\Delta Acinar/+}$ mice (46-50%) was significantly higher than those in *KPten*$^{\Delta Duct/+}$ mice (26-38%), similar to what I found in the CD8+ T cells and Tregs infiltrations (Figure 3.3 C). Specifically, PanIN in the *KPten*$^{\Delta Acinar/+}$ model had twice as much as macrophage infiltration when compared to IPMN in *KPten*$^{\Delta Duct/+}$ mice (Figure 3.3 C). However, I did not observe any significant difference in TAM infiltration between *KPten*$^{\Delta Duct/+}$ PDAC and *KPten*$^{\Delta Acinar/+}$ PDAC (Figure 3.3 C). I did similar macrophage quantification for the *KPten*$^{\Delta Duct/\Delta Duct}$ and *KPten*$^{\Delta Acinar/\Delta Acinar}$ histology sections with homozygous loss of *Pten* and observed similar results (Figure 3.4). In addition, the macrophage infiltration differences between the acinar cell and ductal cell PDAC models were similar between the *Pten* heterozygous and the homozygous models (Figure 3.3, Figure 3.4). Taken together, these results show that lesions arising from acinar cells tend to attract more macrophages than precursor lesions of a ductal cell origin, at least in this genetic context.

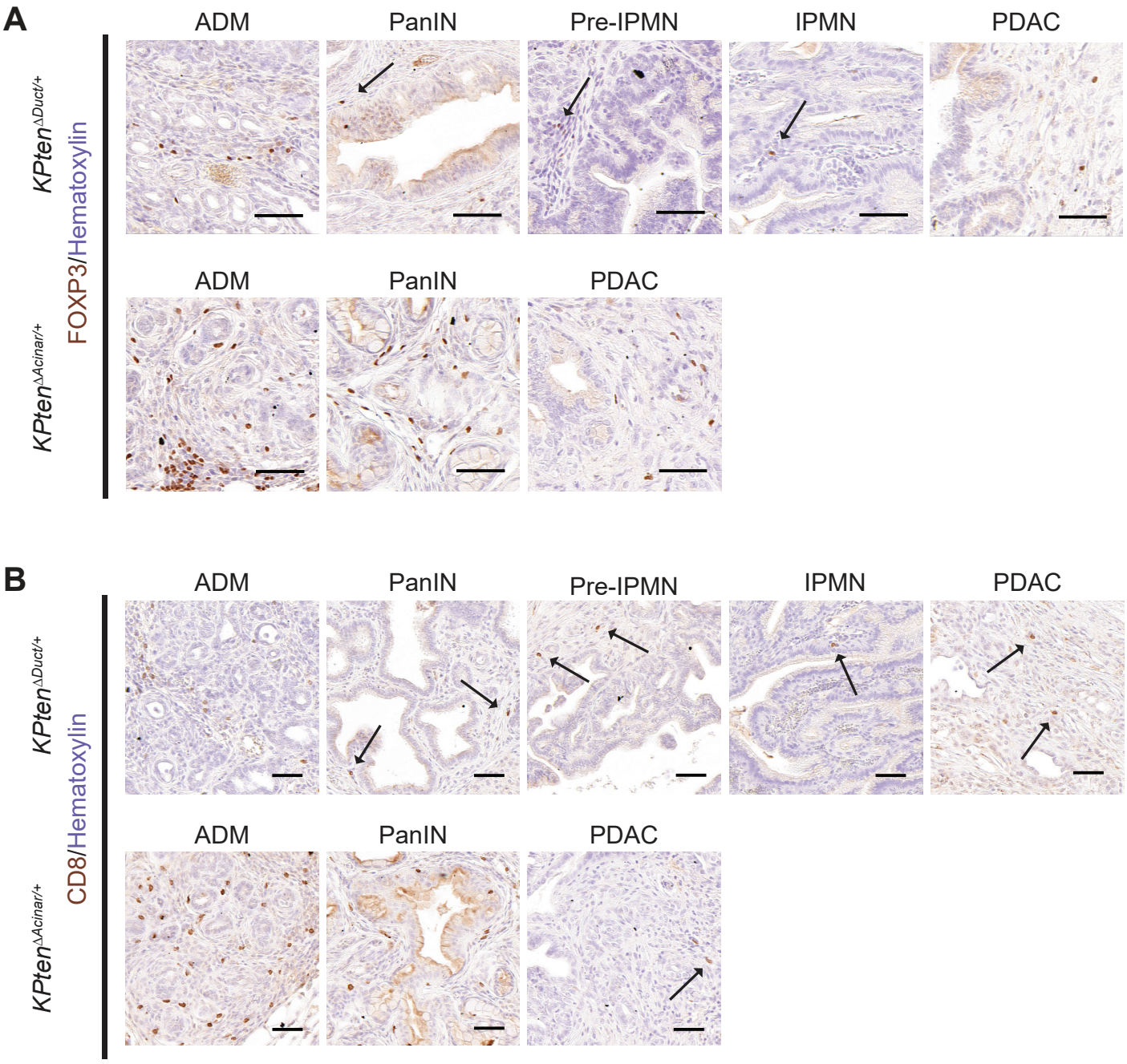

Figure 3.1 Tregs and CD8+ T cells infiltration pattern in precursor lesions and PDAC between *KPten*$^{\Delta Acinar/+}$ and *KPten*$^{\Delta Duct/+}$ mice.

(A) Representative images of immunohistochemistry for FOXP3 in different precursor lesions and PDAC in *KPten*$^{\Delta Duct/+}$ and *KPten*$^{\Delta Acinar/+}$ mice. Black arrows point Tregs cells.

(B) Representative images of immunohistochemistry staining for CD8 in different precursor lesions and PDAC in *KPten*$^{\Delta Duct/+}$ and *KPten*$^{\Delta Acinar/+}$ mice. Black arrows point CD8+ T cells. Scale bar: 50 μm.

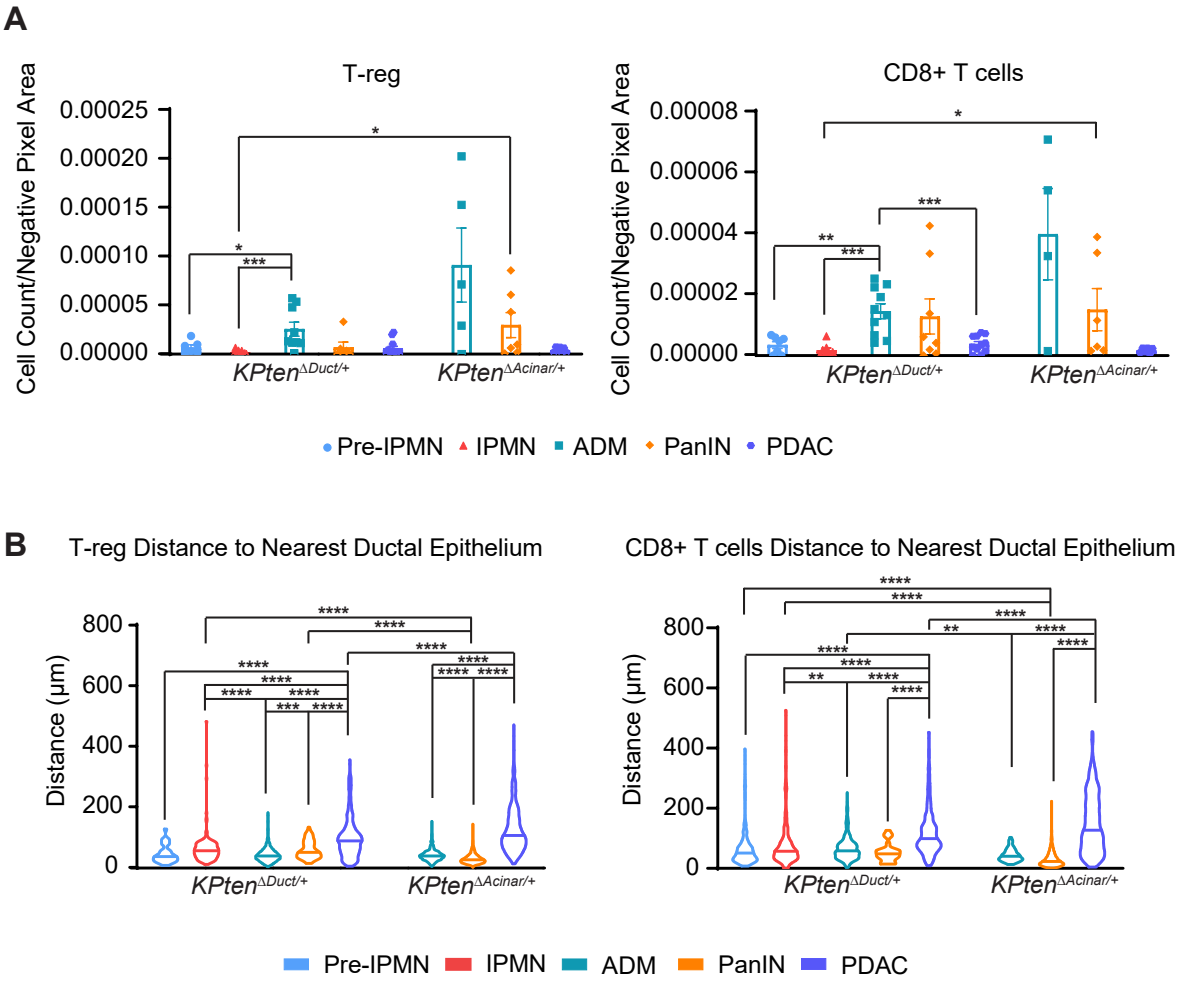

Figure 3.2 Treg and CD8+ T cells infiltration level and proximity to neoplastic cells are different between *KPten*$^{\Delta Acinar/+}$ and *KPten*$^{\Delta Duct/+}$ mice.

(A, left) Quantification of Tregs as indicated by FOXP3+ cells divided by the total number of hematoxylin positive pixels in a region of interest in *KPten*$^{\Delta Duct/+}$ and *KPten*$^{\Delta Acinar/+}$ mice (n=10-12 mice per genotype). (A, right) Quantification of CD8+ T cells as indicated by the number of

CD8+ cells divided by the total number of hematoxylin positive pixels in a region of interest in *KPten*$^{\Delta Duct/+}$ and *KPten*$^{\Delta Acinar/+}$ mice (n=10-14 mice per genotype). Mann–Whitney U test was used for statistic calculation.

(B, left) Quantification of the distance between individual FOXP3+ T cells and the nearest glandular structure lumen in *KPten*$^{\Delta Duct/+}$ and *KPten*$^{\Delta Acinar/+}$ mice (n=10-12 mice per genotype).

(B, right) Quantification of the distance between individual CD8+ T cells and the nearest glandular structure lumen in *KPten*$^{\Delta Duct/+}$ and *KPten*$^{\Delta Acinar/+}$ mice (n=10-14 mice per genotype).

All values shown in either box graph or violin plot to demonstrate data distribution. One-way ANOVA with Tukey test was used for statistic calculation. *P<0.05, **P<0.01, ***P<0.001, ****P<0.0001.

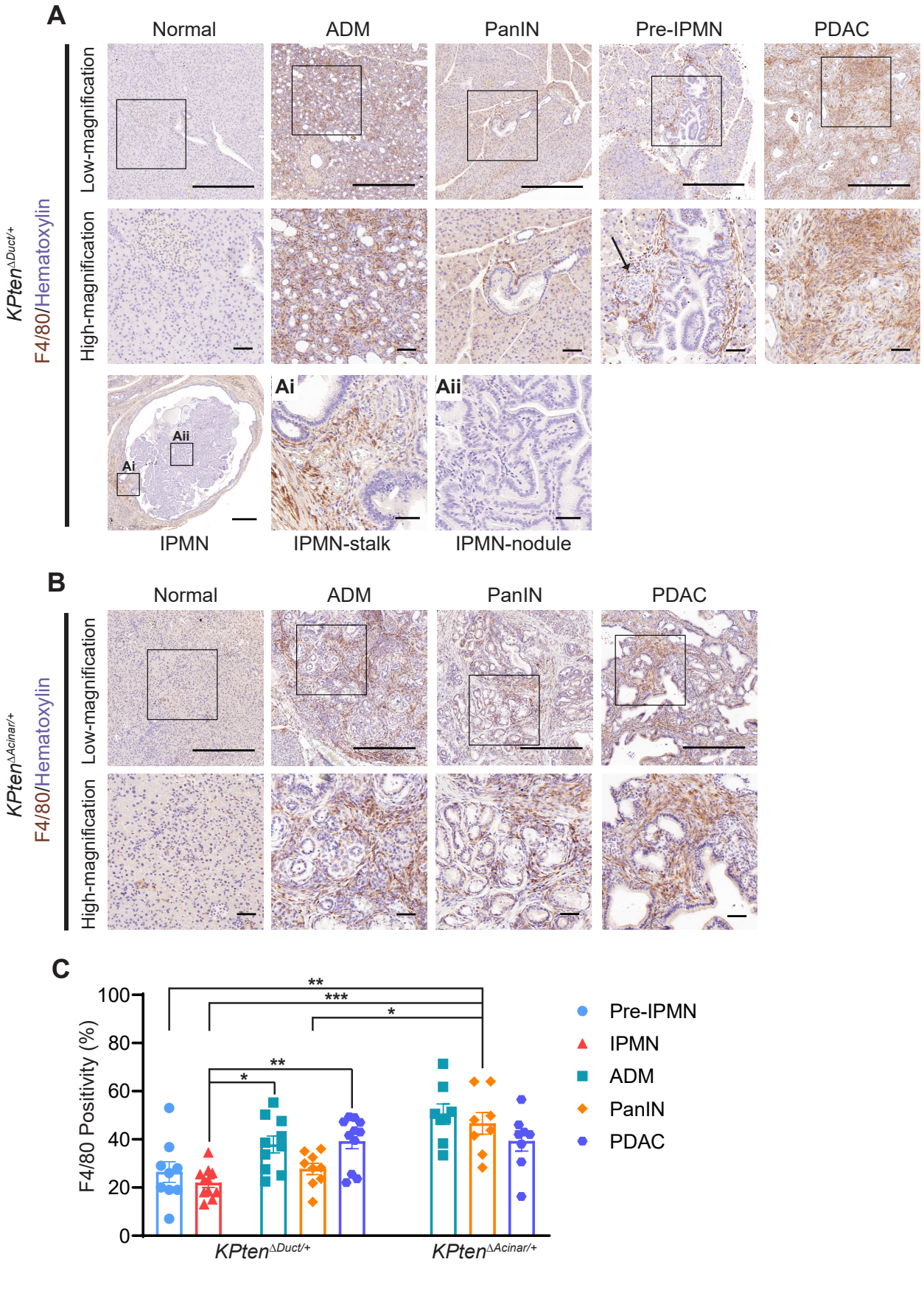
A
Normal
ADM
PanIN
Pre-IPMN
PDAC
KPten ΔDuct/+
F4/80/Hematoxylin
Low-magnification
High-magnification
Ai
Aii
IPMN
IPMN-stalk
IPMN-nodule
B
Normal
ADM
PanIN
PDAC
KPten ΔAcinar/+
F4/80/Hematoxylin
Low-magnification
High-magnification
C
F4/80 Positivity (%)
100
80
60
40
20
0
**
***
*
**
*
KPten ΔDuct/+
KPten ΔAcinar/+
Pre-IPMN
IPMN
ADM
PanIN
PDAC

Figure 3.3 Macrophage infiltration differs at the precursor lesion level between *KPten*$^{\Delta Duct/+}$ and *KPten*$^{\Delta Acinar/+}$ mice, but not at PDAC stage.

Low-magnification (top row) and high-magnification (box outlined area in top row shown in bottom row) images of immunohistochemistry for F4/80 in different precursor lesions and PDAC in *KPten*$^{\Delta Duct/+}$ (A) and *KPten*$^{\Delta Acinar/+}$ (B) mice. Black arrow in (A) points PDAC microinvasion in an area near a pre-IPMN. Ai and Aii in (A) are high-magnification images of the stalk and nodule aspects of the IPMN shown at low power in the first column.

(C) Quantification of macrophages infiltration as indicated by F4/80 staining positivity in a region of interest in *KPten*$^{\Delta Duct/+}$ and *KPten*$^{\Delta Acinar/+}$ mice (n=11-13 mice per genotype).

All values shown in box graph to demonstrate data distribution. All values shown as mean±SEM. One-way ANOVA with Tukey test was used for statistic calculation. *P<0.05, **P<0.01, ***P<0.001. Scale bar: 400 μm (A, top, IPMN; B, top), 50 μm (A, bottom, Ai, Aii; B, bottom).

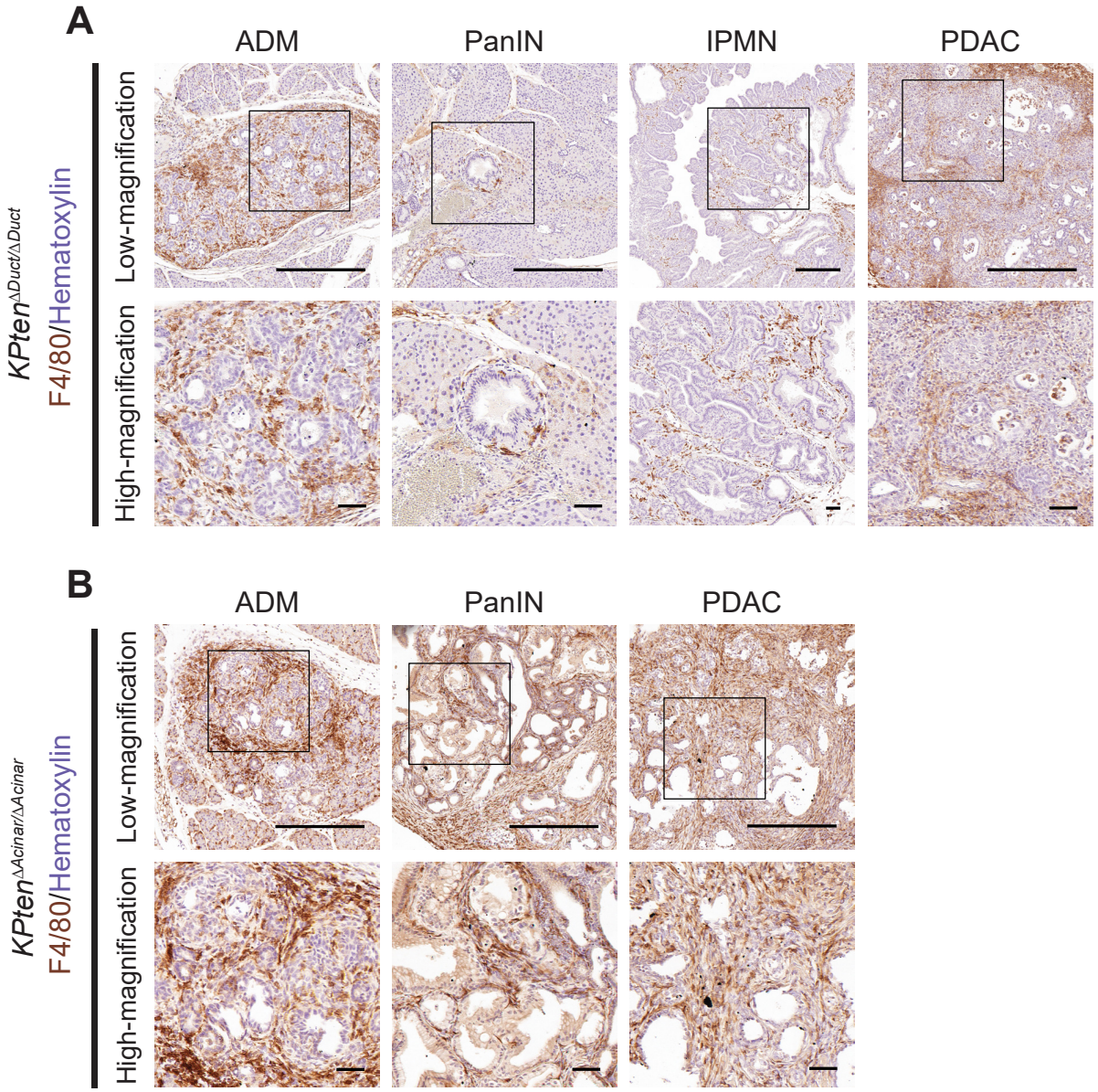
A
ADM
PanIN
IPMN
PDAC
KPten^ΔDuct/ΔDuct
F4/80/Hematoxylin
Low-magnification
High-magnification
B
ADM
PanIN
PDAC
KPten^ΔAcinar/ΔAcinar
F4/80/Hematoxylin
Low-magnification
High-magnification
C
F4/80 Positivity (%)
100
80
60
40
20
0
***
*
***
*
*
IPMN
ADM
PanIN
PDAC
KPten^ΔDuct/ΔDuct
KPten^ΔAcinar/ΔAcinar

Figure 3.4 Macrophage infiltration between *KPten*$^{\Delta Duct/\Delta Duct}$ and *KPten*$^{\Delta Acinar/\Delta Acinar}$ also differs at the precursor lesion level, but not at PDAC stage.

Low-magnification (top row) and high-magnification (box outlined area in top row shown in bottom row) images of immunohistochemistry for F4/80 in different precursor lesions and PDAC in *KPten*$^{\Delta Duct/+}$ (A) and *KPten*$^{\Delta Acinar/+}$ (B) mice.

(C) Quantification of macrophage infiltration as indicated by F4/80 staining positivity in a region of interest in *KPten*$^{\Delta Duct/\Delta Duct}$ and *KPten*$^{\Delta Acinar/\Delta Acinar}$ mice (n=9-10 mice per genotype).

All values shown in box graph to demonstrate data distribution. All values shown as mean±SEM. One-way ANOVA with Tukey test was used for statistic calculation. *P<0.05, ***P<0.001.

Scale bar: 400 μm (A, B top), 50 μm (A, B bottom).

Chapter 4: Cellular origin determines immune and PDAC phenotype

4.1 Genetic characterization of primary cell lines created from *KPten*$^{\Delta Duct}$ and *KPten*$^{\Delta Acinar}$ mice.

Based on the classical definition of macrophage activation states, macrophages can be polarized to a M1-like pro-inflammatory state, or a M2-like anti-inflammatory state depending on cytokine and chemokine signals in the TME (van Dalen et al., 2018). However, recent studies suggested that the polarization of TAMs was dynamic and plastic rather than fixed at one of the extreme ends of the M1 to M2 spectrum (Rőszer, 2015; Xue et al., 2014). As we observed differences in FOXP3+ and CD8+ cell infiltration, as well as differences in the presence of macrophages as normal cells formed tumors from acinar and ductal cells, we decided to study macrophage polarization differences between the two cellular origin models by using an *in vitro* polarization system. To do this our laboratory previously established PDAC primary cell lines specifically from tumors from different cellular origins, so that we could create conditioned media from the tumor cells. I have designated these PDAC cell lines as *KPten*$^{\Delta Duct}$ (367, 409, 746A-the numbers represent different mice) or *KPten*$^{\Delta Acinar}$ (321A, 333A, 339A) PDAC cells. These cell lines were established from tumors from two *KPten*$^{\Delta Duct/+}$ mice (367, 746A, no macroscopic IPMN was noted), one macroscopic IPMN in a *KPten*$^{\Delta Duct/\Delta Duct}$ mouse (409, arising from spontaneous recombination of the genetic alleles), and three grossly visible tumors in *KPten*$^{\Delta Acinar/+}$ (321A, 333A, 339A) mice (note: cell lines derived from the same cellular origin are treated as biological replicates). In terms of the morphology of the PDAC cell lines, they showed epithelial cobblestone-like morphology and grew in colonies of cells, which generated a monolayer on the thick collagen gel of the cell culture plate (Figure 4.1 A). All PDAC cell lines showed

recombination of the *Kras*^{G12D} allele (Figure 4.1 B), and all *KPten*$^{\Delta Acinar}$ PDAC cell lines showed genetic loss of heterozygosity at the *Pten* locus (Figure 4.1 C). The two *KPten*$^{\Delta Duct/+}$ PDAC cell lines 367 and 746A still retained some level of wildtype *Pten* allele (Figure 4.1 C). As a result, I have characterized these PDAC cell lines for the first time and showed that all *KPten*$^{\Delta Acinar}$ PDAC cell lines had loss of *Pten* heterozygosity, whereas the two *KPten*$^{\Delta Duct/+}$ PDAC cell lines still retained the wildtype *Pten* allele.

4.2 Optimization of PDAC culture media for macrophage polarization studies.

To harvest PDAC cell line conditioned media to study the macrophage polarization phenotype, I first cultured the PDAC cell lines until they reached 50-60% confluence, then refreshed the media and let it condition for 24 hrs. Afterwards, I harvested this conditioned media and dilute it 2:3 with complete macrophage media, and subsequently used this mixture to condition macrophages for 24 hrs. To first test out my macrophage polarization paradigm, I used RAW 264.7 macrophages due to their easy culture conditions and their reported ability to polarize in response to PDAC conditioned media (Khabipov et al., 2019). I used conditioned media generated from one of the *KPten*$^{\Delta Duct}$ PDAC cell lines, 367, to try to polarize RAW 264.7 macrophages for 24 hrs. I also included a M0 control (cultured in RAW 264.7 macrophage medium only), a negative control (NC) (cultured in 2:3 ratio of unconditioned pancreatic ductal medium to RAW 264.7 macrophages medium), a M1 control (cultured in NC media with 50 ng/ml IFN-γ), and a M2 control (cultured in NC media with 10 ng/ml of IL-4 and IL-13). After 24 hrs, I harvested RAW 264.7 macrophages from each polarization group to perform an arginase activity or a nitric oxide synthase (iNOS) activity assay (Figure 4.2 A, B). Surprisingly, I observed a high-level arginase activity and iNOS activity in the NC control media compared to

the M0 control media (Figure 4.2 A, B). Thus, some components of the duct media alone likely induced the arginase activity in the NC and M1 controls, and the iNOS activity in the M2 and NC controls (Figure 4.2 A, B). Additionally, because the level of arginase and iNOS activities in the RAW 264.7 cells exposed to *KPten*$^{\Delta Duct}$-367 conditioned media was similar to the NC control, this suggested that any activity from the tumor cell line might simply be due to background activity caused by the pancreatic ductal medium.

To reduce the arginase and iNOS activity levels induced by the pancreatic ductal medium, I tried removing different components in the medium recipe one by one and then polarizing RAW 264.7 macrophages in the specific drop-out media mixed with RAW 264.7 macrophage medium at a 2:3 ratio for 24 hrs. Afterwards, I harvested RNA from the macrophages and chose to use qPCR assays of *Arg1* and *Nos2* (iNOS) gene expression as readout for the arginase and iNOS activity to improve the throughput of my assays. I found that only by removing bovine serum albumin (BSA), bovine pituitary extract (BPE), soybean trypsin inhibitor (STI), insulin-transferrin-selenium (ITS), and cholera toxin together from the pancreatic ductal medium (5-drop-out media) could decrease the expression level of both *Arg1* and *Nos2* by 20- and 4-fold (Figure 4.2 C). However, the level of *Nos2* was still about 20-fold higher compared to M0 control (Figure 4.2 C). To further reduce the *Nos2* expression, I focused on removing components that might have substantial amounts of endotoxin, since it could trigger a strong pro-inflammatory response in macrophages (Laskin et al., 1994). To identify components with endotoxin, I performed a limulus amebocyte lysate (LAL) assay on pancreatic ductal medium components that might have substantial amount of endotoxin. Surprisingly, I found that fungizone has a relatively high amount of endotoxin units that accounted for almost all of the

endotoxins present in the 5-drop-out media configuration (Figure 4.2 D). Therefore, I removed fungizone from the 5-Drop-out media and designated this new medium formula as 6-Drop-out ductal media. qPCR analysis of *Arg1* and *Nos2* expression level shows the *Nos2* background induced by the 6-Drop-out ductal media was reduced to almost the same level as the M0 control (Figure 4.2 E).

After successfully generating the low-endotoxin, low arginase background 6-Drop-out ductal media, I cultured $KPten^{\Delta Acinar}$ and $KPten^{\Delta Duct}$ PDAC cell lines in this medium for at least 5 passages to monitor gene expression by qPCR because we hypothesized that some of the cytokine gene expression previously in tumor cell lines from our laboratory could be due to the presence of the endotoxin. I specifically examined the expression of those cytokine genes previously identified in the Kopp laboratory as differentially expressed between tumors of different cellular origins (manuscript in preparation) (Figure 4.3 A-E). I found that expression of genes, such as *Tnf*, *Il33*, and *Il4ra* reduced over time but began to stabilize after 3 passages in the 6-Drop-out media. This suggested that although the cytokine expressions in these PDAC cell lines did change after being cultured in the 6-Drop-out media, they eventually stabilized. I also noticed during the passaging of the cells in 6-Drop-out media that their expansion times began to reduce noticeably. Because I had completely removed BPE, which is thought to act like a serum replacement factor, I doubled the amount of Nu-Serum IV to compensate for the loss of serum. This complementation restored growth of 5 of the 6 cell lines. The sixth line, $KPten^{\Delta Duct}$ 367 couldn't proliferate in this complemented Drop-out medium long-term and underwent senescence (Figure 4.3 F). As a result, $KPten^{\Delta Duct}$ 367 was excluded from further polarization analysis with the 6-Drop-out ductal cell media. Additionally, the other 2 $KPten^{\Delta Duct}$ PDAC cell

lines began growing faster with apparent loss of cell contact inhibition and acquired a mesenchymal morphology (Figure 4.3 G). Interestingly, the *KPten*$^{\Delta Acinar}$ cell lines did not change their growth or morphology in the 6-Drop-out ductal cell media suggesting that the 6-Drop-out media was permissive for *KPten*$^{\Delta Acinar}$ cells but exerted a selection pressure on *KPten*$^{\Delta Duct}$ cell lines. Overall, these results demonstrate the effects of medium components on influencing immune cell phenotypes and cytokine expression in tumor cells, as well as emphasizes the importance of reducing the background activity induced by the medium itself.

4.3 *KPten*$^{\Delta Acinar}$ and *KPten*$^{\Delta Duct}$ PDAC cells polarized RAW 264.7 macrophages and BMDMs with an M2-like phenotype but with different cytokine expressions

After optimizing my macrophage polarization conditions, I generated conditioned media from each of the remaining *KPten*$^{\Delta Acinar}$ and *KPten*$^{\Delta Duct}$ PDAC cell lines and then froze it in aliquots. I then conditioned RAW 264.7 macrophages with the PDAC conditioned media for 24 hrs. I have combined biological replicates (cell lines) derived from each cellular origin together for the qPCR analysis, and I have shown the triplicates for each cell line to show the heterogeneity between the biological replicates. qPCR analysis of the 264.7 cells exposed to conditioned media derived from *KPten*$^{\Delta Acinar}$ PDAC cells showed higher than baseline levels of *Tnf*, *Cd86*, and M2-cell state markers *Arg1* and *Cxcr2* (Takeya & Komohara, 2016) (Figure 4.4A). *KPten*$^{\Delta Duct}$ PDAC conditioned macrophages on the other hand expressed higher than baseline levels of *Tnf*, *Arg1*, and *Il10*; and lower than baseline level of *Nos2* (Figure 4.4A). Comparing the two cellular origins, *KPten*$^{\Delta Acinar}$ PDAC conditioned RAW macrophages expressed significantly higher levels of *Agr1* and *Cxcr2*, whereas *KPten*$^{\Delta Duct}$ PDAC conditioned macrophages expressed higher level of *Il10* and decreased level of *Nos2* (Figure 4.4A). However, I found that conditioned RAW

macrophages do not express M2-cell state TAM markers *Mrc1* and *Cd163* (Ct value higher than 35) (Haque et al., 2019). Therefore, I decided to validate and further test my observations in primary bone marrow-derived macrophages (BMDMs), as they have been widely used for macrophage phenotyping studies (Orecchioni et al., 2019).

First, I harvested femur bone marrow (BM) cells from wild-type BL6 females at 6-11 weeks of age. I preferentially used females, since my PDAC cell lines were all collected from female mice. I then differentiated these cells into F4/80+ macrophages using M-CSF for 7 days. Consistent with a macrophage identity, more than 95% of the BM-derived cells were typically CD11b+F4/80+ after 7 days of culture (Figure 4.4.B). Similar to RAW 264.7 cells, I then re-plated macrophages on day 7 of culture into 6 wells then exposed them to conditioned media from $KPten^{\Delta Acinar}$ and $KPten^{\Delta Duct}$ PDAC cell lines. Similar to my observations with RAW264.7 cells, qPCR analysis shows that BMDMs polarized by $KPten^{\Delta Acinar}$ PDAC cells exhibited higher than baseline expression of M1-cell state marker *Il6* (Orecchioni et al., 2019), *Arg1*, *Cxcr2*, *Mrc1*, and *Cd163* (Figure 4.4 C). $KPten^{\Delta Duct}$ PDAC polarized BMDMs, on the other hand, expressed higher than baseline levels of *Arg1*, *Il10*, *Mrc1*, and *Cd163*; and lower than baseline level of *Nos2* (Figure 4.4 C). Comparing the two cellular origins, by $KPten^{\Delta Acinar}$ BMDMs exhibited a much higher levels of *Il6* and *Arg1*, whereas $KPten^{\Delta Duct}$ BMDMs expressed lower levels of *Cd86*, *Nos2*, and *Cxcr2*, and a slightly higher level of *Il10* (Figure 4.4 C). The expression of both *Mrc1* and *Cd163* were similar between the BMDMs exposed to $KPten^{\Delta Acinar}$ or $KPten^{\Delta Duct}$ PDAC cell conditioned media (Figure 4.4 C). To repeat this polarization experiment and ensure the PDAC cell lines stability, I generated another batch of conditioned media from $KPten^{\Delta Acinar}$ and $KPten^{\Delta Duct}$ PDAC cell lines and did the same polarization study.

Although there were variations in gene expression levels between the two independent experiments, the general trend of the gene expression difference between BMDMs polarized by *KPten*$^{\Delta Acinar}$ and *KPten*$^{\Delta Duct}$ PDAC cell lines were similar in terms of *Il6*, *Cd86*, *Arg1*, *Il10*, *Cxcr2*, *Mrc1*, and *Cd163* expressions (Figure 4.4 C-D). In both cases, I observed the higher expression of *Nos2* in *KPten*$^{\Delta Acinar}$ BMDMs compared to *KPten*$^{\Delta Duct}$ BMDMs (Figure 4.4 C-D). However, the expressions of *Nos2* were very low with a Ct value of 34 and above, thus was not really expressed.

To validate the M2-like transcriptional programs that I observed in BMDMs polarized by *KPten*$^{\Delta Acinar}$ and *KPten*$^{\Delta Duct}$ PDAC cell lines, we performed IHC staining on *KPten*$^{\Delta Acinar/+}$ and *KPten*$^{\Delta Duct/+}$ PDAC using marker CD206, which is encoded by *Mrc1* (Figure 4.4 E) (Haque et al., 2019). There was a strong signal for CD206 in the stroma (Figure 4.4 E). When quantified by calculating the CD206+ infiltration density, I found that 40% of the area of interest was positive, about the same positivity as F4/80 (Figure 4.4 F). This suggests that the majority of macrophages present surrounding lesions in *KPten*$^{\Delta Acinar/+}$ and *KPten*$^{\Delta Duct/+}$ pancreata have some level of an M2-like phenotype (Figure 4.4 F, Figure 3.3 C, Figure 3.4 C) (Rossi Sebastiano et al., 2020). Similar to the TAM quantification data and the qPCR data, there was no significant difference in CD206+ cells between PDAC in *KPten*$^{\Delta Acinar/+}$ and *KPten*$^{\Delta Duct/+}$ mice (Figure 4.4 F, Figure 3.3 C, Figure 3.4 C). Overall, these results demonstrate that BMDMs polarized by *KPten*$^{\Delta Acinar}$ and *KPten*$^{\Delta Duct}$ PDAC cell lines both exhibit an M2-like phenotype, but the extent and breadth of the changes in the transcriptional program might be different between the two polarized BMDM groups.

4.4 BMDMs polarized by *KPten*$^{\Delta Acinar}$ PDAC cells show a greater similarity to *in vivo* TAMs compared to BMDMs polarized by *KPten*$^{\Delta Duct}$ PDAC cells.

To further investigate the transcriptional landscape of BMDMs polarized by *KPten*$^{\Delta Acinar}$ or *KPten*$^{\Delta Duct}$ PDAC cell conditioned media, we did bulk RNA-sequencing (RNA-seq) on the polarized BMDM samples, as well as the M0, NC, M1, and M2 controls. BMDMs polarized by the *KPten*$^{\Delta Acinar}$ PDAC cell line 339A was omitted from the analysis due to RNA degradation at the time of sequencing. Analysis of differentially expressed genes revealed that compared to the negative control groups (M0 and NC combined), 197 genes were more highly expressed in *KPten*$^{\Delta Acinar}$ PDAC polarized BMDMs, whereas only 27 genes were more highly expressed in *KPten*$^{\Delta Duct}$ PDAC polarized BMDMs (Figure 4.5 A-B, Appendix A.1-A.2). In both cases, most of the differentially expressed genes were downregulated compared to the negative control group (Figure 4.5 A, B). Examination of the genes that were upregulated in *KPten*$^{\Delta Acinar}$ BMDMs suggested that they are related to GM-CSF signaling (*Ccl6*, *Ccr1*, *Csf2rb*) (Croxford et al., 2015; Jarmin et al., 1999), STAT5 pathway (*Arg1*, *Socs2*, *Ccl9*) (Hennighausen & Robinson, 2008; Huen et al., 2015; T. Yang et al., 2016), STAT3 pathway (*Stat3*, *Socs3*, *Cd274*) (Hennighausen & Robinson, 2008; Marzec et al., 2008), and NF-κB activation (*Tlr4*, *Arid5a*, *Nfkbia*) (Figure 4.5 A) (Nyati et al., 2019). One notable gene is *Cd274*, which codes the immune checkpoint protein, programmed cell death receptor ligand 1 (PD-L1). Many studies have shown that the expression of PD-L1 in PDAC contributed to a worse prognosis and poorer survival outcome for patients (Birnbaum et al., 2016; Liang et al., 2018; Yamaki et al., 2017; Yue Zhang et al., 2022). This suggested the TAM population in *KPten*$^{\Delta Acinar}$ PDAC might contribute to a worse survival outcome. Gene Ontology (GO) analysis of pathways enriched in *KPten*$^{\Delta Acinar}$ BMDMs also revealed categories related to cytokine signaling response, induction of NF-κB, and

inflammatory response, indicating a strong polarization response of *KPten*$^{\Delta Acinar}$ BMDMs (Figure 4.5 C, Appendix A.3).

Interestingly, most of the genes upregulated in *KPten*$^{\Delta Duct}$ BMDMs compared to controls were related to protein folding and cell adhesion (Figure 4.5 B, D, Appendix A.4). However, *KPten*$^{\Delta Duct}$ BMDMs uniquely expressed higher levels of *Mrc1*, which is a well-known M2-like TAM marker; and *Cd93*, which has been recently shown to be associated with an M2-like TAM phenotype (Figure 4.5 B, D, Appendix A.4) (Z. Zhang et al., 2022). The higher expression of *Mrc1* in *KPten*$^{\Delta Duct}$ BMDMs by RNA-seq might be the fact that *KPten*$^{\Delta Acinar}$-339A polarized BMDMs, which had high expression level of *Mrc1* (Figure 4.4 C-D), were not included for the RNA-seq analysis. Nevertheless, *KPten*$^{\Delta Duct}$ BMDMs also expressed higher level of *Mki67*, indicating higher proliferation (Figure 4.5 B). We also found *KPten*$^{\Delta Acinar}$ BMDMs and *KPten*$^{\Delta Duct}$ BMDMs shared 8 markers, mostly related to cell-cell adhesion (Appendix A.1-A.2). However, one common marker that stood out was *Cd33*, whose expression in myeloid cells was associated with a poor survival in melanoma patients (Choi et al., 2020). We also noticed that the PDAC cell polarized BMDMs do not fit neatly into the same transcriptomic profile as either M1 or M2 controls, as their most variable gene expressions do not align (Figure 4.5 E). This confirms previous results (Boyer et al., 2022; Wu et al., 2020) and suggests that tumor-educated macrophages (TEM) do not equal to an M1 or M2 state, and that the traditional M1 and M2 polarized states do not necessarily represent the *in vivo* TME.

To further investigate if our *in vitro* polarized BMDMs show similarity to *in vivo* TAMs, we re-analyzed a scRNA-seq data set of the macrophages from the “late KIC”

(*Pdx1Cre;Kras^{G12D};Cdkn2a$^{flox/flox}$*) mouse model from Hosein and colleagues (Hosein et al., 2019), and then created a pseudo-bulk RNA-seq gene expression profile to identify markers that were unique to the KIC macrophages then compared their expression between the *KPten$^{\Delta Acinar}$* BMDMs and *KPten$^{\Delta Duct}$* BMDMs from our studies. Comparing our polarized BMDM markers with late KIC macrophage markers, we found a somewhat stronger correlation between *KPten$^{\Delta Acinar}$* BMDMs and the late KIC macrophages, compared to *KPten$^{\Delta Duct}$* BMDMs and the late KIC macrophages (Figure 4.5 F). In addition, 26 out of the 38 enriched pathways in *KPten$^{\Delta Acinar}$* BMDMs overlap with those in the late KIC macrophages, including those shown in Figure 4.5 C (Appendix A.3). On the contrary, *KPten$^{\Delta Duct}$* BMDMs showed relatively little resemblance to the late KIC macrophages, with only one enriched pathway overlapping with the late KIC macrophages (Figure 4.5 F, Appendix A.4). Although both *KPten$^{\Delta Acinar}$* BMDMs and *KPten$^{\Delta Duct}$* BMDMs expressed KIC macrophage markers, about two-third of these markers were higher expressed by *KPten$^{\Delta Acinar}$* BMDMs compared to *KPten$^{\Delta Duct}$* BMDMs (Appendix A.5), again indicating a stronger resemblance between *KPten$^{\Delta Acinar}$* BMDMs and *in vivo* TAMs. Overall, these results demonstrate that *KPten$^{\Delta Acinar}$* PDAC cell conditioned media polarized BMDMs to a greater extent and more closely resembled previously examined *in vivo* TAMs.

4.5 BMDMs were polarized by *KPten$^{\Delta Acinar}$* PDAC cells through the GM-CSF signaling pathway.

To further dissect the mechanism behind the difference in BMDM polarization between the acinar and the ductal cell of origin, we did RNA-seq on the *KPten$^{\Delta Acinar}$* and *KPten$^{\Delta Duct}$* PDAC cell lines. I found that many cytokines and chemokines were differentially expressed between *KPten$^{\Delta Acinar}$* and *KPten$^{\Delta Duct}$* PDAC cell lines, including *Csf2*, which codes for the protein GM-

CSF (Figure 4.6 A-B). GM-CSF signaling is known to affect the STAT3, STAT5, and NF-κB signaling pathways (Thorn et al., 2016; Zhan et al., 2019). Here, I have found that some of the genes that are upregulated in *KPten*$^{\Delta Acinar}$ BMDMs are related to these pathways (Figure 4.5 A). This suggests a potential role for GM-CSF in driving the transcriptional response of BMDMs to *KPten*$^{\Delta Acinar}$ conditioned media with a greater response. In addition, Boyer and colleagues recently showed the secretion of GM-CSF from PDAC cells polarized BMDMs towards a pro-tumoral phenotype with an increased expression in markers such as *Arg1* and *Ccr1* (Boyer et al., 2022). To examine whether the GM-CSF protein was present in the PDAC cell conditioned media, I measured the secreted levels of GM-CSF and other cytokines in PDAC cell conditioned media using the Proteome Profiler Mouse Cytokine Array Kit, Panel A (R&D Systems). I found that *KPten*$^{\Delta Acinar}$ PDAC cells indeed have a much higher secretion of GM-CSF in their conditioned media, validating the RNA-seq data (Figure 4.6 C, Appendix B.1).

To further interrogate whether the higher secretion level of GM-CSF from *KPten*$^{\Delta Acinar}$ PDAC cells drove the increased M2-like phenotype of *KPten*$^{\Delta Acinar}$ BMDMs, I neutralized GM-CSF using antibody in the conditioned media and then cultured BMDMs with the neutralized conditioned media or an IgG control neutralized conditioned media. I then used qPCR to quantify the changes in selected pro-M2 like and GM-CSF signaling related markers in polarized BMDMs. As expected, I saw a dramatic reduction in *Arg1* expression with the neutralization of GM-CSF in *KPten*$^{\Delta Acinar}$ BMDMs compared to the IgG control (Figure 4.6 D). The absolute magnitude of suppression varied, likely due to the differences in expression and secretion of GM-CSF present in each *KPten*$^{\Delta Acinar}$ PDAC cell line (Figure 4.6 A-C). Interestingly, *KPten*$^{\Delta Duct}$ PDAC cell line 409 also expressed low levels of *Csf2*, but neutralizing GM-CSF activity in

conditioned media from this cell line slightly increased the *Arg1* expression in *KPten*$^{\Delta Duct}$-409 polarized BMDMs (Figure 4.6 D). This suggests that how BMDMs responded to the GM-CSF neutralization in the PDAC conditioned media depended on which cellular origin the media was derived from. In addition to changes in *Arg1* expression, I observed the reduction of many GM-CSF signaling related-markers (*Ccl6*, *Ccr1*, *Csf2rb*, *Socs2*, *Ccl9*, *Cd274*) and the STAT3-related M2-TAM marker *Mrc1* (Jones et al., 2016) in *KPten*$^{\Delta Acinar}$ BMDMs (Figure 4.6 D). The expression level of *Il6*, which is a downstream target of NF-κB signaling (Brasier, 2010), decreased significantly in the *KPten*$^{\Delta Acinar}$ BMDMs neutralized with GM-CSF as well (Figure 4.6 D). Interestingly, the expression level of pro-M2 markers *Cd163* and *Saa3* (Djurec et al., 2018; Shiraishi et al., 2018) increased in *KPten*$^{\Delta Acinar}$ BMDMs treated with anti-GM-CSF antibody (Figure 4.6 D).

KPten$^{\Delta Duct}$ BMDMs, on the other hand, showed a much milder response in gene expressions following the GM-CSF neutralization. More specifically, only the *KPten*$^{\Delta Duct}$ PDAC cell line 409 conditioned BMDMs produced a significant response following the neutralization in some genes related to GM-CSF signaling (*Ccl6*, *Socs2*), and the M2-markers *Mrc1* and *Cd163* (Figure 4.6 D). It should be noted that some gene expressions, especially those in *KPten*$^{\Delta Duct}$ BMDMs, were not influenced by the GM-CSF neutralization, indicating GM-CSF was not the only cytokine that promoted the BMDM polarization phenotype (Figure 4.6 D). Interestingly, similar to the observation with the expression changes in *Arg1* between cellular origins, the gene expression changes in *Cd163* also showed the opposite trend between *KPten*$^{\Delta Acinar}$ BMDMs and *KPten*$^{\Delta Duct}$ 409 BMDMs (Figure 4.6 D). In addition, the expression levels of most of the genes in Figure 4.6 D expressed by *KPten*$^{\Delta Acinar}$ BMDMs treated with anti-GM-CSF antibody decreased to almost

the same level as *KPten*$^{\Delta Duct}$ BMDMs (Figure 4.6 D). Overall, these results show *KPten*$^{\Delta Acinar}$ PDAC cell polarized BMDMs to a greater extent, which was at least partially due to increased GM-CSF signaling.

4.6 *KPten*$^{\Delta Acinar}$ and *KPten*$^{\Delta Duct}$ PDAC cells show distinct molecular subtypes.

To further investigate the transcriptomic differences between *KPten*$^{\Delta Acinar}$ and *KPten*$^{\Delta Duct}$ PDAC cells in addition to differences in cytokine expressions, we performed differential gene expression analysis of the previously mentioned RNA sequencing data, as described previously (Vuilleumier et al., 2019). We found that most of the top 200 most significantly differentially expressed genes were enriched in expression in the *KPten*$^{\Delta Duct}$ PDAC cell lines compared to *KPten*$^{\Delta Acinar}$ PDAC cells (Figure 4.7 A). Examining the GO terms associated with the differentially expressed genes, as well as the genes with the greatest change, suggested that *KPten*$^{\Delta Duct}$ PDAC cell lines had higher expression of genes associated with a mesenchymal phenotype. Studies in the past decade aiming to subtype clinical PDAC samples by using next generation sequencing demonstrated that at a transcriptomic level, PDAC can be generally categorize into either basal (quasi-mesenchymal) or classical subtypes (Martens et al., 2019). Basal subtype PDAC tended to express genes enriched for signatures of epithelial-to-mesenchymal transition (EMT) program and interferon response (Aiello et al., 2018; Chan-Seng-Yue et al., 2020; Espinet et al., 2021), whereas classical subtype PDAC expressed genes enriched for epithelial, gastric, and pancreatic lineage programs (Chan-Seng-Yue et al., 2020; Raghavan et al., 2021). To examine which PDAC subtype *KPten*$^{\Delta Duct}$ or *KPten*$^{\Delta Acinar}$ PDAC cell lines more closely resembled, we studied the expression of genes related to a basal or classical subtype. I found that genes associated with a basal and classical subtype were differentially

expressed in *KPten*$^{\Delta Acinar}$ and *KPten*$^{\Delta Duct}$ PDAC cells (Figure 4.7 B). Specifically, while *KPten*$^{\Delta Duct}$ PDAC cells strongly expressed many basal subtype-related genes, especially ones related to an EMT-like program, *KPten*$^{\Delta Acinar}$ PDAC cells had higher expression levels of classical subtype-related genes (Figure 4.7 B). In addition, *KPten*$^{\Delta Duct}$ PDAC cells also expressed a higher level of interferon response-related gene signatures, such as *Ifit2*, *Ifitm1*, and *Ifitm2* (Figure 4.7 B) that were previously linked to a basal like PDAC subtype (Espinet et al., 2021). This suggests a more classical-like PDAC subtype for *KPten*$^{\Delta Acinar}$ PDAC cells, and a more basal-like PDAC subtype for *KPten*$^{\Delta Duct}$ PDAC cells.

To further compare the molecular subtypes of our PDAC cell lines with previously published data sets examining PDAC subtype, we first compared our PDAC cell lines with the mouse PDAC cell lines created in Aiello et al. (Aiello et al., 2018). These cell lines were characterized as either having complete EMT (C-EMT) with basal-like phenotype, or partial EMT (P-EMT) with classical-like phenotype. We used these cell lines to create a basal to classical Eigen vector and then examined how close our PDAC cell lines clustered to the basal or classical end of the spectrum. Principle component analysis (PCA) revealed that *KPten*$^{\Delta Acinar}$ PDAC cell lines were clustered with P-EMT cell lines, indicating their similarity to the classical phenotype (Figure 4.7 C). *KPten*$^{\Delta Duct}$ PDAC cell lines were situated between P-EMT cell lines and C-EMT cell lines, with one of the *KPten*$^{\Delta Duct}$ PDAC cell lines being closer to the C-EMT cluster. The clustering of the *KPten*$^{\Delta Duct}$ PDAC cell lines near zero suggests that they have an intermediate phenotype with a weak similarity to the classical subtype or basal subtype (Figure 4.7 C).

I then compared the differentially expressed gene signatures in *KPten*$^{\Delta Acinar}$ and *KPten*$^{\Delta Duct}$ PDAC cells with the scRNA-seq human PDAC subtype signatures from Raghavan et al. (Raghavan et al., 2021). In this paper, they found metastatic PDAC cells exhibited 3 different subtypes intracellularly, including single-cell basal (scBasal), single-cell classical (scClassical), and single-cell intermediate co-expressing (scIC) subtype categories (Raghavan et al., 2021). Using the gene signatures correlated with these 3 different PDAC subtypes published by Raghavan et al., we compared our *KPten*$^{\Delta Acinar}$ and *KPten*$^{\Delta Duct}$ PDAC cell markers with the makers in Raghavan et al., and this was plotted as a Venn diagram. These Venn diagrams revealed that *KPten*$^{\Delta Acinar}$ PDAC cells indeed have a strong overlap with scClassical subtype, some overlap with scBasal subtype, and few gene shared with scIC subtype (Figure 4.7 D). On the other hand, *KPten*$^{\Delta Duct}$ PDAC cells have a weaker overlap with scClassical subtype compared with *KPten*$^{\Delta Acinar}$ PDAC cells (Figure 4.7 E). However, *KPten*$^{\Delta Duct}$ PDAC cells have a stronger overlap with both scBasal and scIC subtypes than *KPten*$^{\Delta Acinar}$ PDAC cells (Figure 4.7 E). These results support the hypothesis that *KPten*$^{\Delta Duct}$ PDAC cells have a more intermediate/basal-like subtype, while *KPten*$^{\Delta Acinar}$ PDAC cells have more features associated with a classical subtype. Although at this stage, we can't make any definitive conclusions regarding how this subtype difference might affect the expression level of *Csf2*, this will be discussed in detail in Chapter 5. Overall, these results show that cellular origin affects the molecular subtype of PDAC, with the ductal cellular origin having a tendency towards basal-like phenotype, and the acinar cellular origin having a classical phenotype.

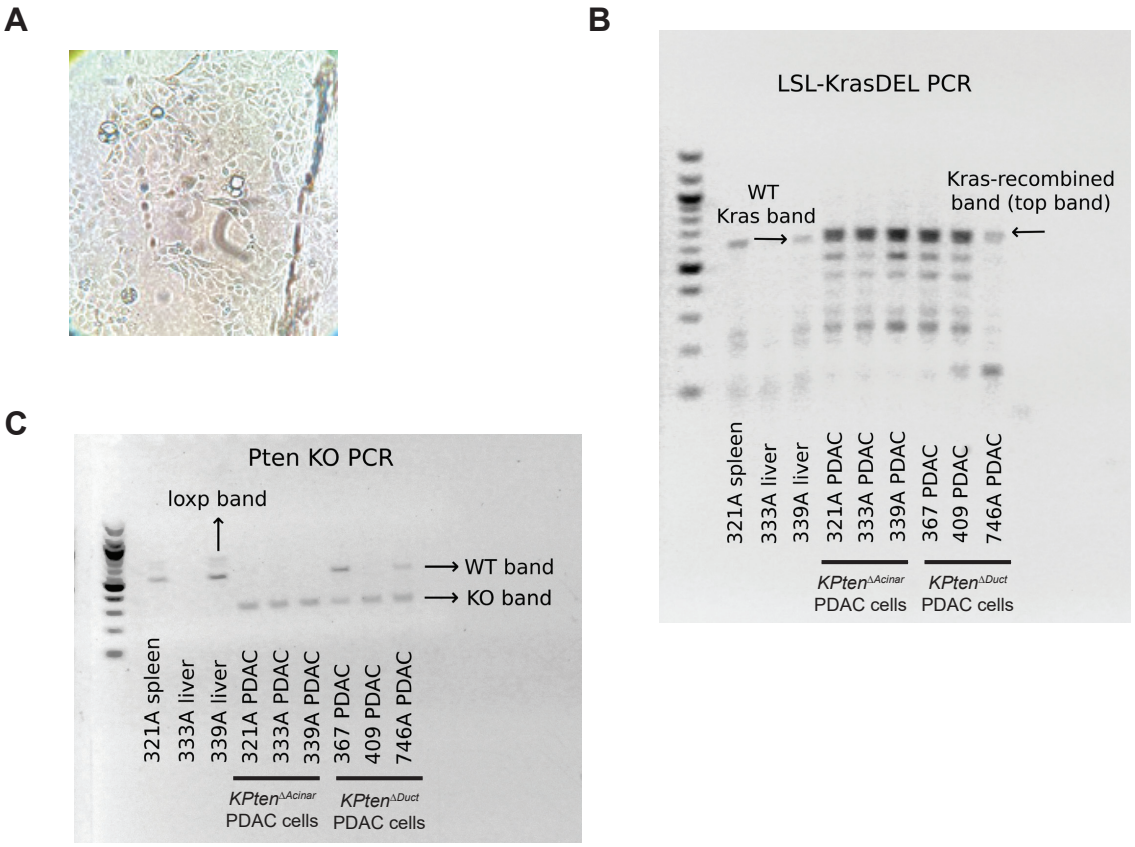

Figure 4.1 *KPten*$^{\Delta Duct}$ and *KPten*$^{\Delta Acinar}$ PDAC cell lines morphology and alleles recombination.

(A) Representative image showing the cobblestone epithelial morphology of the PDAC cell lines used in this study. PDAC cells grew as colonies and formed a monolayer structure, with occasional vesicles detected. Original magnification: 40X.

(B) LSL-KrasDEL PCR showing the recombination of the *Kras* allele. The wildtype *Kras* band is 622bp, whereas the *Kras*^{G12D} recombined allele is 650bp. The DNA ladder is in 100bp increments. Spleen and liver tissues were used as negative controls.

(C) *Pten* knockout PCR showing the recombination of the *Pten* allele. The *Pten* Loxp band is 650bp, wildtype *Pten* band is 500bp, whereas the *Pten* recombined deletion allele is 300bp. The DNA ladder in 100bp increments. Spleen and liver tissues were used as negative controls.

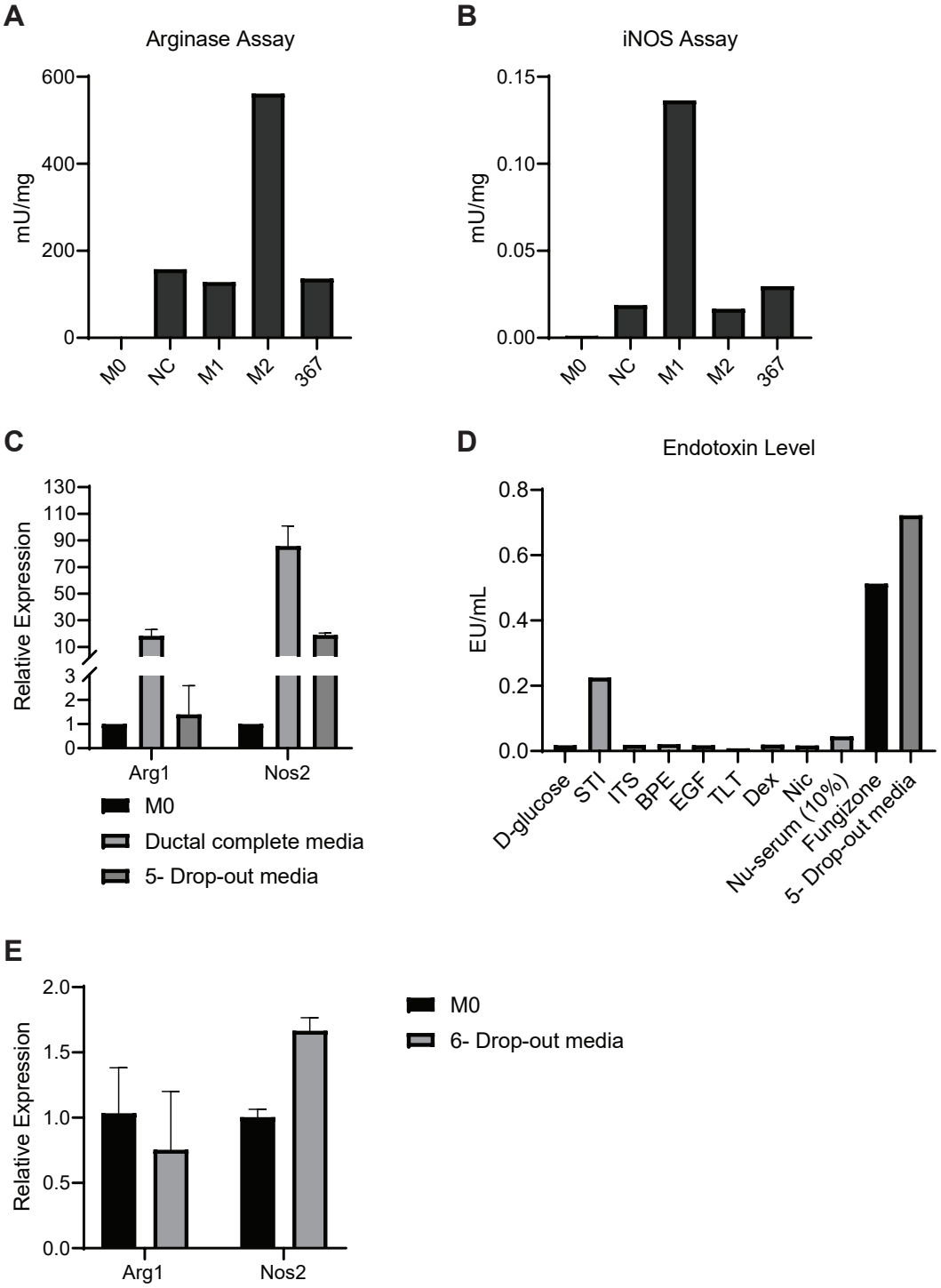

Figure 4.2 Pancreatic ductal cell medium optimization for macrophage polarization experiment.

(A) Arginase activity of RAW 264.7 macrophages measured as mU per mg of total protein in different polarization groups. (n=1 per group).

(B) Nitric oxide synthase (iNOS) activity of RAW 264.7 macrophages measured as mU per mg of total protein in different polarization groups. (n=1 per group).

(C) Relative expression level of *Arg1* and *Nos2* (iNOS) of RAW 264.7 macrophages polarized by the complete pancreatic ductal medium and the 5 drop-out media (pancreatic ductal medium without BSA, BPE, STI, ITS, and cholera toxin) compared to the M0 control measured by qPCR. (n=2 per group)

(D) Endotoxin level of each component of the pancreatic ducal medium measured by LAL assay as Endotoxin Unit (EU) per ml. (n=1 per group)

(E) Relative expression level of *Arg1* and *Nos2* of RAW 264.7 macrophages polarized by the 6 drop-out media (pancreatic ductal medium without BSA, BPE, STI, ITS, fungizone, and cholera toxin) compared to the M0 control measured by qPCR. (n=3 per group)

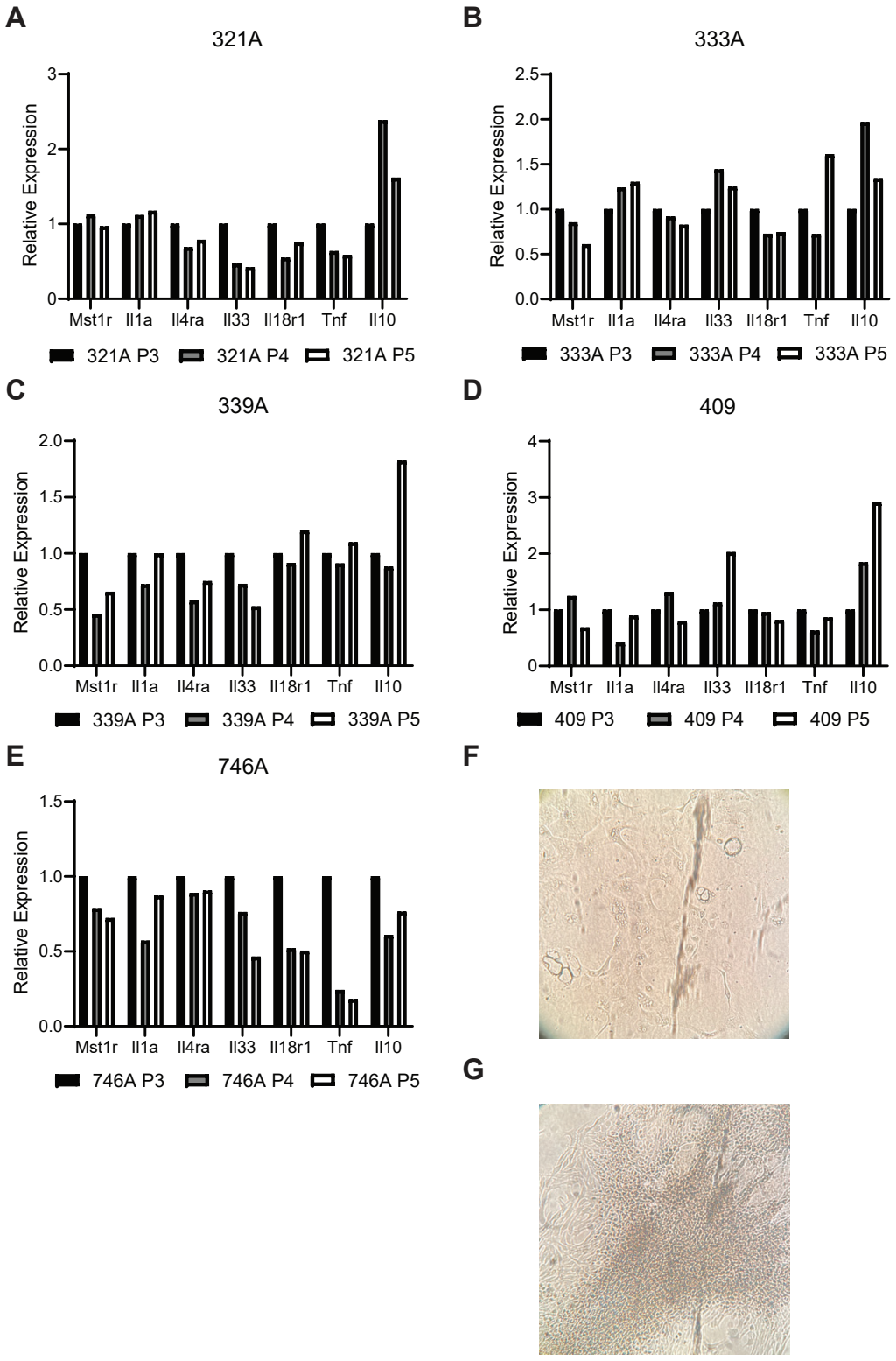

Figure 4.3 PDAC cell lines showed stabilized cytokine expressions after 5 passages in the Drop-out media.

(A-E) Selected cytokine expressions in *KPten*$^{\Delta Acinar}$ and *KPten*$^{\Delta Duct}$ PDAC cell lines stabilized starting at passage 3 (P3) when cultured in the 6-Drop-out ductal media by qPCR. Data is normalized to the gene expression from passage 3. (n=1 per cell line)

(F) *KPten*$^{\Delta Duct}$ PDAC cell line 367 showed senescent features at P3 in the 6-Drop-out ductal media (enlarged and flattened cell morphology) when cultured in the 6-Drop-out ductal media. Original magnification: 40X.

(G) *KPten*$^{\Delta Duct}$ PDAC cell lines 409 and 746A showed loss of cell contact inhibition and mesenchymal morphology when cultured in the 6-Drop-out ductal media. Original magnification: 40X.

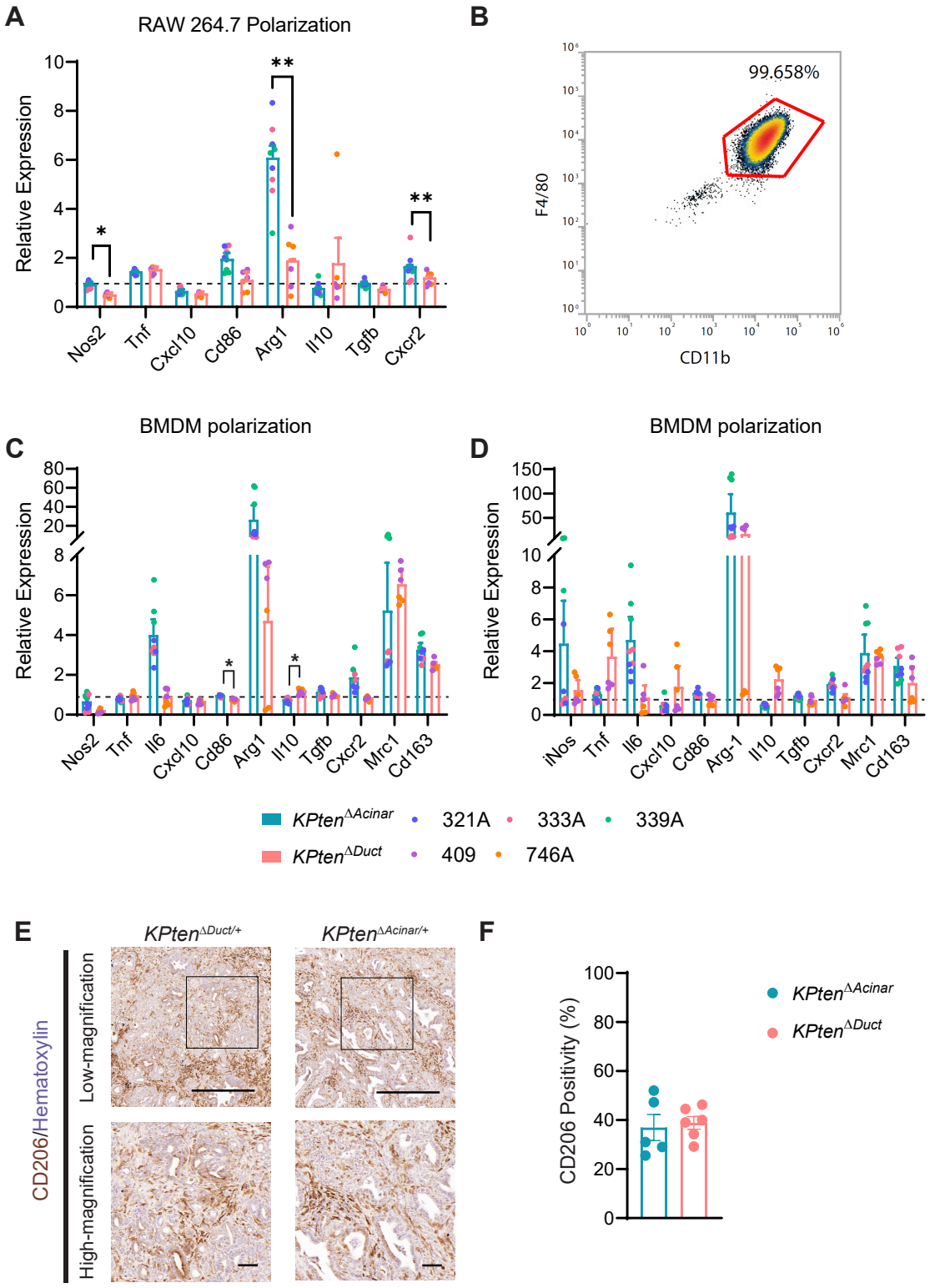

Figure 4.4 *KPten*$^{\Delta Acinar}$ and *KPten*$^{\Delta Duct}$ PDAC cells polarized RAW 264.7 macrophages and BMDMs with an M2-like phenotype.

(A) Relative expression of genes in RAW 264.7 macrophages polarized by *KPten*$^{\Delta Acinar}$ and *KPten*$^{\Delta Duct}$ conditioned media normalized to the negative control (NC). Experiment was performed with 3 replicates (same color) for each cell line, and each cell line was represented as a different color (the color for each cell line can be seen in the legend underneath C and D, there are three *KPten*$^{\Delta Acinar}$ cell lines and two *KPten*$^{\Delta Duct}$ cell lines). Dotted line indicates NC baseline. (n=3 cell lines for *KPten*$^{\Delta Acinar}$, n=2 cell lines for *KPten*$^{\Delta Duct}$) Mann–Whitney U test was used for statistic calculation.

(B) Representative flow cytometry graph showing BMDMs being double positive for CD11b and F4/80 markers.

(C) Relative expression of genes in BMDMs polarized by *KPten*$^{\Delta Acinar}$ and *KPten*$^{\Delta Duct}$ conditioned media normalized to the negative control (NC). Experiment was performed with 3 replicates (same color) for each cell line, and each cell line was represented as a different color (the color for each cell line can be seen in the legend underneath C and D, there are three *KPten*$^{\Delta Acinar}$ cell lines and two *KPten*$^{\Delta Duct}$ cell lines). Dotted line indicates NC baseline. (n=3 cell lines for *KPten*$^{\Delta Acinar}$, n=2 cell lines for *KPten*$^{\Delta Duct}$) Mann–Whitney U test was used for statistic calculation.

(D) Repeated BMDM polarization experiment using a second batch of conditioned media generated from *KPten*$^{\Delta Acinar}$ and *KPten*$^{\Delta Duct}$ PDAC cell lines. Relative expression of genes was normalized to NC. Experiment was performed with 3 replicates (same color) for each cell line, and each cell line was represented as a different color (the color for each cell line can be seen in the legend underneath C and D, there are three *KPten*$^{\Delta Acinar}$ cell lines and two *KPten*$^{\Delta Duct}$ cell lines). Dotted line indicates NC baseline. (n=3 cell lines for *KPten*$^{\Delta Acinar}$, n=2 cell lines for

KPten$^{\Delta Duct}$) Figure legend for each cell line for figure A, C, and D are indicated at the bottom of graph C and D. Mann–Whitney U test was used for statistic calculation.

(E) Low-magnification (top row) and high-magnification (bottom row) images of immunohistochemistry for CD206 in *KPten*$^{\Delta Duct/+}$ and *KPten*$^{\Delta Acinar/+}$ PDAC.

(F) Quantification of CD206 staining positivity in *KPten*$^{\Delta Duct/+}$ and *KPten*$^{\Delta Acinar/+}$ PDAC (n=5-6). All values shown as mean±SEM. *P<0.05, **P<0.01. Scale bar: 400 μm (D top), 50 μm (D bottom).

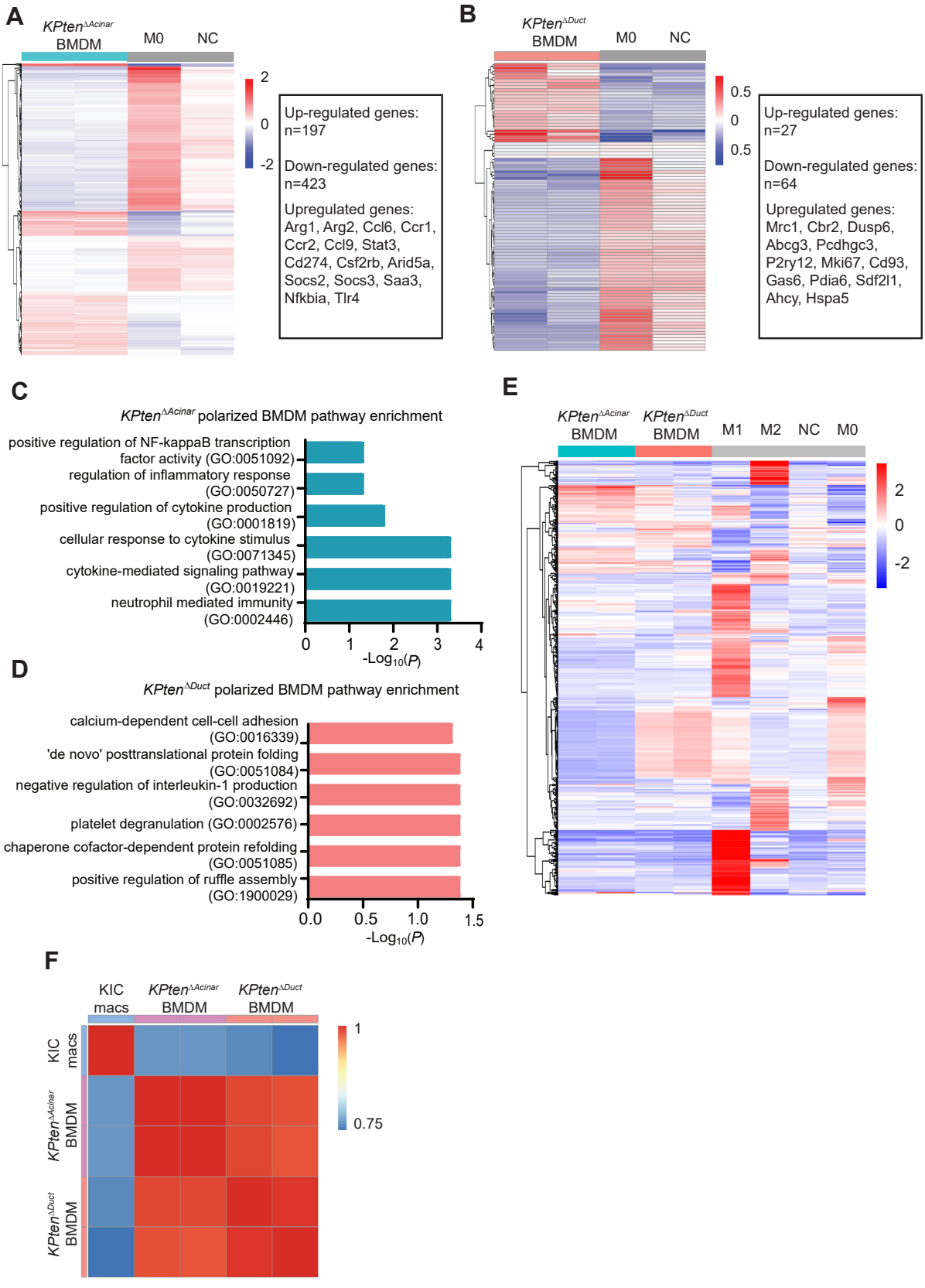
A
KPtenΔAcinar BMDM
M0
NC
2
0
-2
Up-regulated genes: n=197
Down-regulated genes: n=423
Upregulated genes: Arg1, Arg2, Ccl6, Ccr1, Ccr2, Ccl9, Stat3, Cd274, Csf2rb, Arid5a, Socs2, Socs3, Saa3, Nfkbia, Tlr4
B
KPtenΔDuct BMDM
M0
NC
0.5
0
0.5
Up-regulated genes: n=27
Down-regulated genes: n=64
Upregulated genes: Mrc1, Cbr2, Dusp6, Abcg3, Pcdhgc3, P2ry12, Mki67, Cd93, Gas6, Pdia6, Sdf2l1, Ahcy, Hspa5
C
KPtenΔAcinar polarized BMDM pathway enrichment
positive regulation of NF-kappaB transcription factor activity (GO:0051092)
regulation of inflammatory response (GO:0050727)
positive regulation of cytokine production (GO:0001819)
cellular response to cytokine stimulus (GO:0071345)
cytokine-mediated signaling pathway (GO:0019221)
neutrophil mediated immunity (GO:0002446)
0 1 2 3 4
-Log10(P)
D
KPtenΔDuct polarized BMDM pathway enrichment
calcium-dependent cell-cell adhesion (GO:0016339)
'de novo' posttranslational protein folding (GO:0051084)
negative regulation of interleukin-1 production (GO:0032692)
platelet degranulation (GO:0002576)
chaperone cofactor-dependent protein refolding (GO:0051085)
positive regulation of ruffle assembly (GO:1900029)
0.0 0.5 1.0 1.5
-Log10(P)
E
KPtenΔAcinar BMDM
KPtenΔDuct BMDM
M1
M2
NC
M0
2
0
-2
F
KIC macs
KPtenΔAcinar BMDM
KPtenΔDuct BMDM
1
0.75

Figure 4.5 BMDMs polarized by *KPten*$^{\Delta Acinar}$ PDAC cells show greater similarity to *in vivo* TAMs.

(A) Heat map of the differentially expressed genes in *KPten*$^{\Delta Acinar}$ PDAC polarized BMDMs compared to M0 and NC groups.

(B) Heat map of the differentially expressed genes in *KPten*$^{\Delta Duct}$ PDAC polarized BMDMs compared to M0 and NC groups.

(C) Expression signatures enriched in *KPten*$^{\Delta Acinar}$ PDAC polarized BMDMs relative to M0 and NC groups, as identified by Enrichr analysis. These enriched pathways also overlap with those enriched in late KIC macrophages described in Hosein et al.

(D) Expression signatures enriched in *KPten*$^{\Delta Duct}$ PDAC polarized BMDMs relative to M0 and NC groups, as identified by Enrichr analysis. Platelet degradation (GO: 0002576) pathway overlaps with late KIC macrophages described in Hosein et al.

(E) Heat map showing the top 500 most variable genes in each of the BMDM groups. Note the transcriptomic difference between *KPten*$^{\Delta Acinar}$ BMDMs, *KPten*$^{\Delta Duct}$ BMDMs, and the M1 and M2 control BMDMs.

(F) Heat map showing the Spearman correlation between *KPten*$^{\Delta Acinar}$ PDAC polarized BMDMs, *KPten*$^{\Delta Duct}$ PDAC polarized BMDMs, and late KIC macrophages described in Hosein et al.

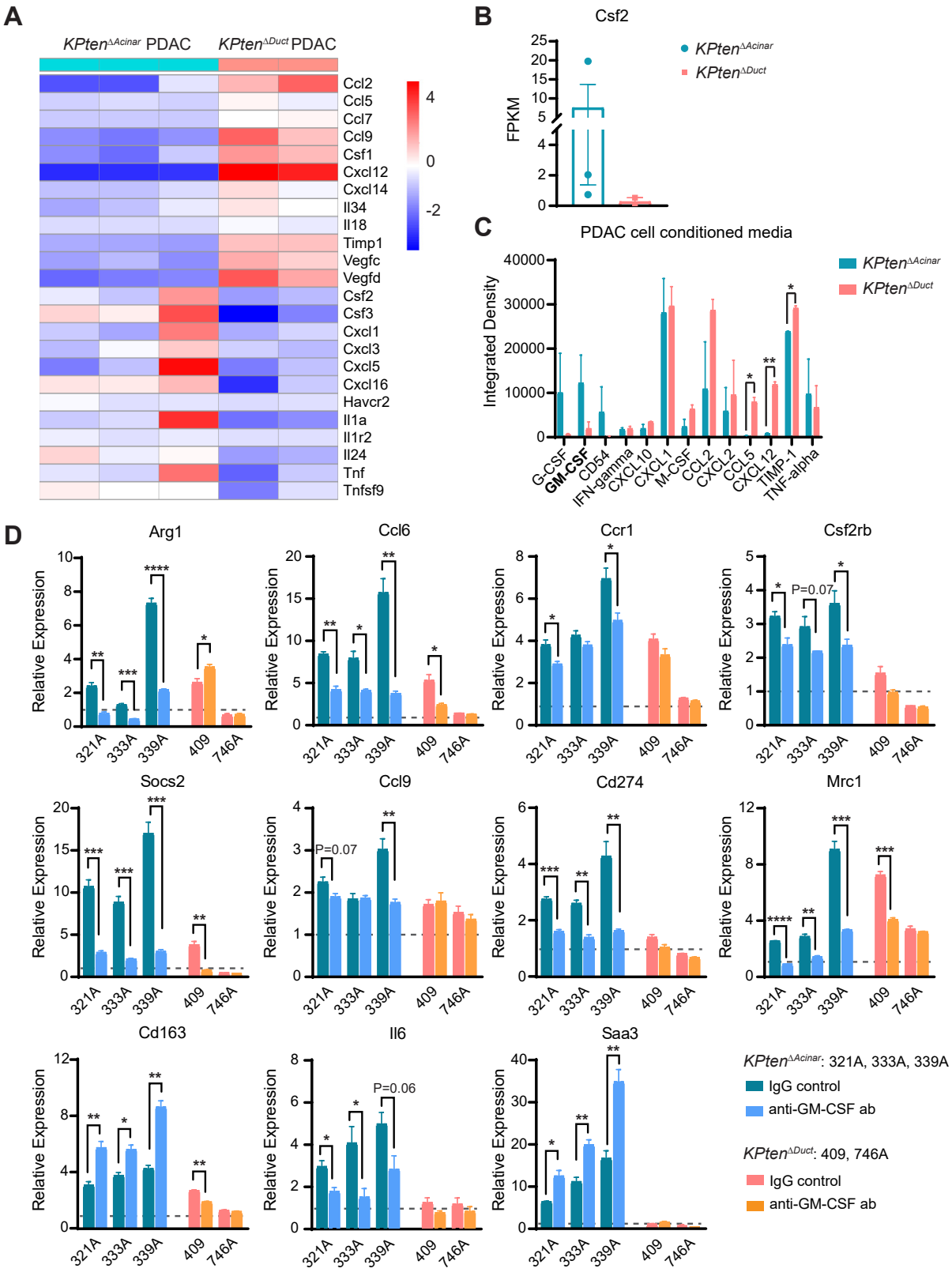

Figure 4.6 *KPten*$^{\Delta Acinar}$ PDAC cells polarized BMDMs through GM-CSF signaling pathway.

(A) Heat map of the differentially expressed chemokines and cytokines in *KPten*$^{\Delta Acinar}$ and *KPten*$^{\Delta Duct}$ PDAC cell lines.

(B) Quantification of *Csf2* expression in *KPten*$^{\Delta Acinar}$ and *KPten*$^{\Delta Duct}$ PDAC cell lines. (n=3 for *KPten*$^{\Delta Acinar}$, n=2 for *KPten*$^{\Delta Duct}$)

(C) Quantification of cytokines and chemokines secretion level in the conditioned media generated from *KPten*$^{\Delta Acinar}$ and *KPten*$^{\Delta Duct}$ PDAC cell lines by cytokine array assay. (n=2 for *KPten*$^{\Delta Acinar}$, n=2 for *KPten*$^{\Delta Duct}$) Unpaired student-t test was uased for statistic calculation.

(D) Relative expression of genes related to GM-CSF signaling in *KPten*$^{\Delta Acinar}$ and *KPten*$^{\Delta Duct}$ BMDMs neutralized with anti-GM-CSF antibody or isotype control by qPCR. All gene expressions were normalized to the negative control (NC), which expression levels were indicated as dotted line at fold change equals to 1. Legend at the lower right corner indicates the cellular origin for each PDAC cell polarized BMDM group. Unpaired student-t test was used for statistic calculation.

All values shown as mean±SEM. *P<0.05, **P<0.01, ***P<0.001, ****P<0.0001.

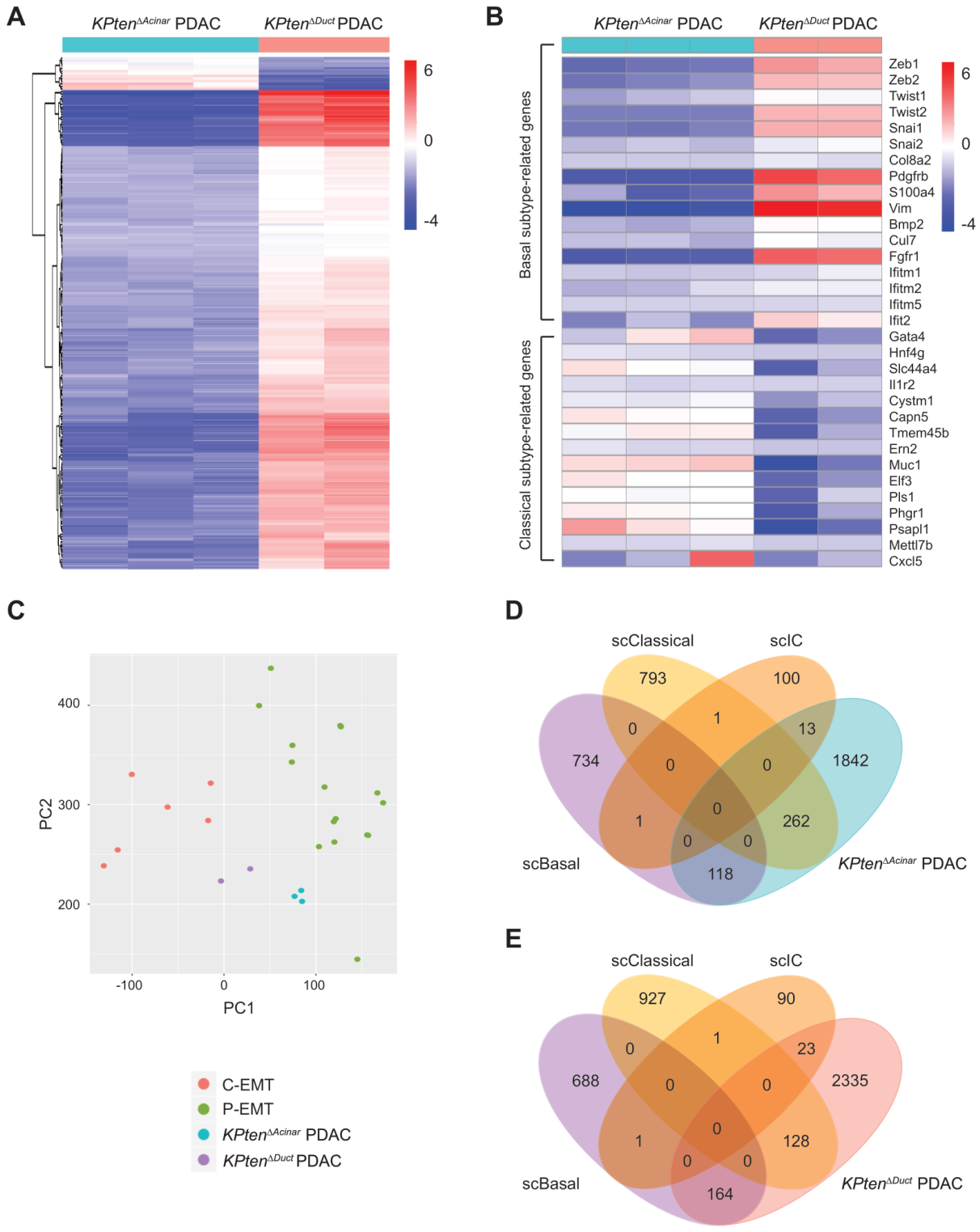

Figure 4.7 *KPten*$^{\Delta Acinar}$ and *KPten*$^{\Delta Duct}$ PDAC cells express distinct molecular subtypes.

(A) Heat map of top 200 differentially expressed genes in *KPten*$^{\Delta Acinar}$ and *KPten*$^{\Delta Duct}$ PDAC cell lines.

(B) Heat map of differentially expressed basal- and classical-PDAC subtype related markers in in *KPten*$^{\Delta Acinar}$ and *KPten*$^{\Delta Duct}$ PDAC cell lines.

(C) Principal component analysis (PCA) plot of *KPten*$^{\Delta Acinar}$ and *KPten*$^{\Delta Duct}$ PDAC cell lines in relation to C-EMT and P-EMT cell lines from Aiello et al.

(D) Venn diagram showing the overlap gene signatures between *KPten*$^{\Delta Acinar}$ PDAC cell lines differentially expressed genes and scBasal, scClassical, and scIC transcriptional states signatures described in Raghavan et al.

(E) Venn diagram showing the overlap gene signatures between *KPten*$^{\Delta Duct}$ PDAC cell lines differentially expressed genes and scBasal, scClassical, and scIC transcriptional states signatures described in Raghavan et al.

Chapter 5: Discussion

I show here that with the same genetic mutations, acinar and ductal cells resulted in distinct precursor lesions, which ultimately led to diverse evolution of the PDAC immune landscape. I found that *KPten*$^{\Delta Acinar/+}$ mice tended to have more immune cell infiltration at the precursor lesion stage compared to *KPten*$^{\Delta Duct/+}$ mice, but at the PDAC stage the infiltration of Tregs, CD8+ T cells, and TAMs were lower in *KPten*$^{\Delta Acinar/+}$ mice. In addition, secreted factors from *KPten*$^{\Delta Acinar}$ PDAC cells had a greater effect on BMDMs and induced both a pro-tumoral phenotype and pro-inflammatory properties. *KPten*$^{\Delta Duct}$ PDAC cells on the other hand had less effect on the BMDM transcriptome, potentially due to lower expression of GM-CSF. In addition, the transcriptome of *KPten*$^{\Delta Acinar}$ PDAC cells was very similar to the classical molecular PDAC subtype, whereas *KPten*$^{\Delta Duct}$ PDAC cells had an intermediate-to-basal-like molecular subtype. In summary, I have shown for the first time that PDAC cellular origins can affect the immune cell infiltration, as well as its evolution and transcriptional phenotype. These results suggest the importance of taking cellular origin into account when studying the immune microenvironment of PDAC and potentially developing therapeutics.

5.1 Cellular origin affects immune landscape evolution from precursor lesion to PDAC

To study the effects of cellular origin on the PDAC immune microenvironment, I investigated the immune infiltration of CD8+ T cells, Tregs, and macrophages into pancreatic lesion areas in *KPten*$^{\Delta Duct/+}$ and *KPten*$^{\Delta Acinar/+}$ mice. Interestingly, I found the infiltration of these immune cells populations is the most abundant in ADM lesion in both models. Macrophages have been shown to drive ADM process by secreting inflammatory cytokines, and their population is abundant and easily detected at the earliest stages of tumorigenesis (Liou et al., 2013; Schlesinger et al., 2020).

Consistent with previous data (Pitarresi et al., 2016; S. Yang et al., 2021), the recruitment of Tregs positively correlates with macrophage infiltration, and it was readily detectable at the ADM stage. It was previously found that with the release of chemokines into the microenvironment, the infiltration of CD8+ T cells also started at an early stage of PDAC tumorigenesis (Foucher et al., 2018), consistent with our findings. It should be noted that the ADM formed in *KPten*$^{\Delta Duct/+}$ mice was the result of inflammation caused by the pancreatic duct blockage and was accompanied the atrophy of acinar cells, whereas the ADM formed in *KPten*$^{\Delta Acinar/+}$ mice was primarily the result of the effects of the oncogenic *Kras* mutation in acinar cells. Interestingly, I observed that immune cell infiltration is higher in *KPten*$^{\Delta Acinar/+}$ ADM than *KPten*$^{\Delta Duct/+}$ ADM, indicating that additional pro-inflammatory signaling driven by Ras activation might promote more immune infiltration than inflammation alone, consistent with previous results (Storz & Crawford, 2020). I also observed macrophage infiltration in IPMN is almost exclusively in the stalk area where the nodule attached to the wall of the cyst and not within the fibrovascular stalk of the nodule itself. Since cancer-associated fibroblasts have been shown to play an important role in the recruitment of macrophages (Gunaydin, 2021), this indicates a potential difference in the stromal composition between the IPMN stalk and the nodule.

I found that the *KPten*$^{\Delta Acinar/+}$ pancreas tends to be more immune-active at precursor lesion stage, whereas in *KPten*$^{\Delta Duct/+}$ pancreas the infiltration of CD8+ T cells, Tregs, and macrophages only increased when IPMN became invasive and formed PDAC. This increased incidence of T cells at PDAC stage was also observed in another IPMN mouse model with *Kras*^{G12D} and loss of *Rnf43* (Hosein et al., 2022). I also observed an inverse relationship between T cell infiltration and its

distance to neoplastic ductal cells, confirming the negative role of stroma on impeding the infiltration of T cells in tumors (Joyce & Fearon, 2015). Interestingly, I found the CD8+ T cells are significantly closer to tumor cells in *KPten*$^{\Delta Duct/+}$ PDAC with higher infiltration compared to *KPten*$^{\Delta Acinar/+}$ PDAC. As spatial distribution of CD8+ T cells in proximity to PDAC correlates with increased overall patient survival (Carstens et al., 2017), this indicates IPMN-derived PDAC might correlate with a better prognosis compared to PanIN-derived PDAC, confirming previous observation (McGinnis et al., 2020). In addition, a high intratumoral CD8+ T cells to macrophage ratio has been shown to correlate with a longer median survival, and patients with lymphoid rich tumors have significantly improved survival outcome after surgery (Liudahl et al., 2021), again suggesting a better outcome for patients with IPMN-derived PDAC.

Previous clinical studies specifically examining the IPMN immune landscape showed that the infiltration of CD8+ T cells decreased as IPMN progressed to become invasive, contrary to our study (Bernard et al., 2019; Roth et al., 2020). It should be noted that these studies did not compare IPMNs within the same histological subtype (Bernard et al., 2019; Roth et al., 2020), whereas in our study the IPMNs formed are predominately pancreatobiliary (PB-IPMN) (Kopp et al., 2018). Our results might indicate the relatively low level of CD8+ T cell infiltration in PB-IPMN contributes to its worst clinical prognosis among all IPMN subtypes (Marius Distler et al., 2013). Overall, our studies show that the immune landscape evolution is fundamentally different between acinar and ductal derived lesions and PDAC. Future studies using multiplex IHC are necessary to further dissect the differences in the immune cell landscape as tumors develop from different cellular origins.

5.2 Cellular origin affects *in vitro* BMDM polarization

I have shown here that BMDMs exposed to conditioned media from *KPten*$^{\Delta Acinar}$ and *KPten*$^{\Delta Duct}$ PDAC cells showed an M2-like phenotype, which I also confirmed was present *in vivo* with IHC staining for CD206. Furthermore, my RNA-seq analysis revealed that both acinar- and ductal-cell-derived PDAC media induced BMDM to express pro-tumoral markers. Specifically, *KPten*$^{\Delta Acinar}$-exposed BMDMs expressed *Arg1*, *Ccr1*, *Ccr2*, *Ccl6*, and *Ccl9*. These genes were previously associated with a pro-tumoral function of TAMs *in vivo* and are reported to be involved in enhancing tumor migration and survival (Grossman et al., 2018; Grzywa et al., 2020; Masetti et al., 2021; Yan et al., 2015; Yaqing Zhang et al., 2020). In addition, the expression of SAA in human TAMs in breast cancer tissue was associated with poor prognosis (M. Yang et al., 2016). The expression of *Cd274* (PD-L1) on TAMs is critical for the immunosuppression of CD8+ T cells *in vivo*, thereby enhancing tumor progression (Petty et al., 2021). As the expression of PD-L1 correlates with worse prognosis and survival for PDAC patients (Birnbaum et al., 2016; Liang et al., 2018; Yamaki et al., 2017; Yue Zhang et al., 2022), this might indicate the TAMs in our acinar cell model also contribute to an unfavourable outcome. However, *KPten*$^{\Delta Acinar}$ BMDMs were polarized to a greater extent compared to *KPten*$^{\Delta Duct}$ BMDMs, indicated by the larger number of differentially expressed genes and enrichment of immune response-related GO pathways. Interestingly, I observed the increased expression of proliferation marker *Mki67* in *KPten*$^{\Delta Duct}$ BMDMs, indicating the ductal-cell-derived PDAC might induce proliferation instead of a strong M2-like phenotype in the BMDMs. On the other hand, *KPten*$^{\Delta Acinar}$ BMDMs showed downregulation in genes related to cell division and cell cycle compared to the negative control group. It has been shown that M2-macrophages derived from the bone marrow lost their immunosuppressive phenotype with increased proliferation *in vitro*,

whereas bone marrow-derived M2-macrophages that were non-proliferative were able to maintain their immunosuppressive phenotype (Cao et al., 2014). This suggests a potential inverse relationship between macrophage polarization and proliferation, which could potentially explain the difference in polarization and proliferation between *KPten*$^{\Delta Duct}$ BMDMs and *KPten*$^{\Delta Acinar}$ BMDMs. In sum, my results strongly suggest that the cellular origin of PDAC can affect macrophage polarization and their proliferation.

When we compared our conditioned BMDMs with markers from late KIC macrophages (Hosein et al., 2019), which were *in vivo* TAMs, I found that *KPten*$^{\Delta Acinar}$ BMDMs showed a greater correlation with *in vivo* TAMs compared to *KPten*$^{\Delta Duct}$ BMDMs. This was also confirmed by the higher gene expression levels of KIC macrophage markers in *KPten*$^{\Delta Acinar}$ BMDMs compared to *KPten*$^{\Delta Duct}$ BMDMs. In addition, KIC macrophages exhibited a pro-inflammatory phenotype (Hosein et al., 2019) and had enriched pathways related to regulation of inflammatory response, which the *KPten*$^{\Delta Acinar}$ BMDMs also shared. This indicates *KPten*$^{\Delta Acinar}$ BMDMs not only showed pro-tumoral properties but exhibited the pro-inflammatory features as well. This shows the complexity of macrophage polarization and that pro-tumoral macrophages do not necessarily express only M2-related markers. Future studies on macrophage polarization are necessary to further dissect this combined effect of polarization that produces both phenotypes at the same time. It should be noted that our conditioned BMDMs do not represent the entire population of *in vivo* TAMs, because a significant population of TAMs in pancreatic tumor *in vivo* are tissue-resident macrophages, which showed a more pro-fibrotic transcriptional profile compared to monocyte-derived TAMs (Baer et al., 2022; Y. Zhu et al., 2017). Our *in vitro* BMDM system could only model monocyte-derived TAMs, thereby excluding the tissue-resident macrophage

population that are found *in vivo* (Toda et al., 2021). As a result, future studies using induced pluripotent stem cell (iPSCs)-derived primitive macrophages would be necessary to further dissect the role of PDAC cellular origin on the polarization of tissue-resident macrophages (Takata et al., 2017). Nonetheless, my study shows that $KPten^{\Delta Acinar}$ PDAC cells polarized BMDMs with a greater similarity to *in vivo* TAM, therefore validating our BMDM polarization system.

Compared to $KPten^{\Delta Acinar}$ BMDMs, $KPten^{\Delta Duct}$ BMDMs showed relatively little overlap with *in vivo* TAMs, potentially since $KPten^{\Delta Duct}$ BMDMs are more similar to the negative control group (M0 and NC BMDMs) and not very polarized in nature. This indicates that unlike the acinar cellular origin, the ductal cell derived-PDAC cells do not play as big of a role in polarizing macrophages and express very few M2-TAM markers according to the RNA-seq data. Interestingly, our previous observation on the increased TAM infiltration in $KPten^{\Delta Duct/+}$ and $KPten^{\Delta Duct/\Delta Duct}$ mice at the PDAC stage and not at the IPMN stage might suggest the increased desmoplastic stroma played a more important role in recruiting TAMs and not the tumor cells themselves. Recent publications suggest cancer associated-fibroblasts (CAFs) play an important role in recruiting and polarizing TAMs towards a pro-tumoral phenotype (Raskov, Orhan, Gaggar, et al., 2021; Velez-Delgado et al., 2022; A. Zhang et al., 2017). This might indicate CAFs play a major role in not only recruiting, but also polarizing TAMs in the ductal cell-derived PDAC, whereas in the acinar cell-derived PDAC both CAFs and the tumor cells could recruit and polarize TAMs. Future studies that incorporate CAFs into the *in vitro* polarization system are necessary to further investigate if CAFs could indeed polarize macrophages better than PDAC cells alone in the ductal cell model.

5.3 Cellular origin differences in BMDM polarization are facilitated by GM-CSF signaling

I have shown here that the expression of many pro-tumoral genes in *KPten*$^{\Delta Acinar}$ BMDMs are facilitated by GM-CSF signaling, which played an important role in the larger polarization effect seen in *KPten*$^{\Delta Acinar}$ BMDMs. GM-CSF has been shown to promote PDAC tumorigenesis and the development of an immunosuppressive myeloid cell population in the PDAC TME (Bayne et al., 2012; Pylayeva-Gupta et al., 2012). Recently, Boyer and colleagues showed GM-CSF could polarize BMDMs with a pro-tumoral phenotype, which was mediated at least partially through metabolic changes (Boyer et al., 2022). Here, I have shown that the pro-tumoral effects by GM-CSF signaling was mediated through many downstream signaling pathways including STAT3 and STAT5, confirming previous results (Ruffolo et al., 2021; Thorn et al., 2016). Interestingly, I found the expression of pro-tumoral markers *Cd163* and *Saa3* increased with the GM-CSF neutralization. The expression of *Cd163* was shown to be inhibited by pro-inflammatory genes such as *Il6* as the result of the activation of NF-κB signaling (Z. Zhu et al., 2020). In our model, the neutralization of GM-CSF dampened the NF-κB signaling, as shown in the decreased expression of *Il6*, which may have subsequently resulted in the increased expression of *Cd163*. As for *Saa3*, its expression was shown to inhibit the effects of GM-CSF signaling through decreasing its receptor transcription (Kim et al., 2017). Therefore, the decreased expression of *Csf2rb* might be the result of increased *Saa3* expression. However, it is still unknown what caused the increased in *Saa3* expression with the neutralization of GM-CSF.

The paradoxical pro-inflammatory and immunosuppressive properties of GM-CSF have been documented (Zhan et al., 2019). This dual role of GM-CSF, with its positive regulation of NF-κB, might contribute to the proinflammatory properties I observed in *KPten*$^{\Delta Acinar}$ BMDMs when compared to the KIC macrophages (Parajuli et al., 2012). Zhan and colleagues suggested that the biological outcome of GM-CSF signaling, and which selective downstream pathway is activated is dependent on its signaling strength (Zhan et al., 2019). According to the cytokine array data, *KPten*$^{\Delta Acinar}$ 339A had the most GM-CSF secreted in the conditioned media, *KPten*$^{\Delta Duct}$ 409 secreted less GM-CSF compared to *KPten*$^{\Delta Acinar}$ PDAC cells, and *KPten*$^{\Delta Duct}$ 746A had almost no GM-CSF in the conditioned media (Appendix B.1). This is reflected in the GM-CSF neutralization data, where *KPten*$^{\Delta Acinar}$ BMDMs had a greater response to neutralization than *KPten*$^{\Delta Duct}$ BMDMs; *KPten*$^{\Delta Duct}$ 409 BMDMs had response in some gene expressions; and 746A BMDMs was not affected by the neutralization at all. This difference in GM-CSF concentration could partially explain the opposite outcomes seen in the expression of *Arg1* and *Cd163* with the neutralization of GM-CSF from the *KPten*$^{\Delta Duct}$ 409 polarized BMDMs compared with *KPten*$^{\Delta Acinar}$ BMDMs. How exactly different doses of GM-CSF orchestrates multiple downstream signaling pathways and regulates specific gene expression still remains unknown (Zhan et al., 2019). In the case of *KPten*$^{\Delta Acinar}$ 339A, its GM-CSF secretion levels were the highest among all PDAC cell lines, perhaps near the saturation level for the assay (Appendix B.1). In addition, *KPten*$^{\Delta Acinar}$ 339A polarized BMDMs expressed the highest amounts of all genes I investigated with my qPCR analysis and had the most changes in those gene's expression with the GM-CSF neutralization. This might suggest that at a very high dosage, GM-CSF could trigger the upregulation of all its downstream signaling pathways, producing a strong add-on effect on the macrophage polarization. Future studies investigating how GM-CSF dosage can

affect macrophage polarization are necessary to further dissect the mechanism behind the paradoxical role of GM-CSF.

Although GM-CSF played an important role in the polarization of *KPten*$^{\Delta Acinar}$ BMDMs, the mechanism behind the small effects of *KPten*$^{\Delta Duct}$ conditioned media on BMDMs is still unknown. As *KPten*$^{\Delta Duct}$ PDAC cells secreted more M-CSF, CXCL12, and CCL5 in the conditioned media, and previous evidence suggests each of these cytokines has an effect on polarizing macrophages into a pro-tumoral phenotype (Babazadeh et al., 2021; Y. Zhu et al., 2014; Zhuang et al., 2021), I neutralized these cytokines and examined changes in gene expression. Unfortunately, I found that neutralization of each of these factors had little effects on expression of gene related to polarization (Appendix B.2-B.4). Nevertheless, I have shown that the difference in GM-CSF expression between *KPten*$^{\Delta Acinar}$ and *KPten*$^{\Delta Duct}$ PDAC cells played a critical role in causing the difference in magnitude of the *Arg1* expression between BMDMs exposed to conditioned media from tumors of two different cellular origins. Future studies are necessary to tease out the mechanism behind the polarization of *KPten*$^{\Delta Duct}$ BMDMs, as well as the interesting induction of BMDM proliferation.

5.4 Cellular origin affects PDAC molecular subtypes

I have shown that the transcriptional profiles of PDAC cells derived from acinar and ductal cellular origins are vastly different, and the two cellular origins resembled different molecular subtypes. While *KPten*$^{\Delta Acinar}$ PDAC cells strongly express classical subtype genes, *KPten*$^{\Delta Duct}$ PDAC cells gene expression resembles an intermediate-to-basal-like subtype. Espinet and colleagues found that a cell-intrinsic activation of an interferon response gene signatures in

PDAC was correlated with a basal-like subtype and a ductal cellular origin (Espinet et al., 2021). We indeed found a higher expression of interferon response-related gene signatures in *KPten*$^{\Delta Duct}$ PDAC cells, confirming previous findings. In addition, Flowers and colleagues recently demonstrated that ductal cell-derived and acinar cell-derived tumor signatures are enriched in basal-like and classical-like subtypes, respectively, by using mouse models, again confirming that cellular origin could impact the molecular subtype of PDAC from an early tumorigenesis stage (Flowers et al., 2021). However, in our study, we found that *KPten*$^{\Delta Duct}$ PDAC cells exhibit a strong intermediate subtype, in addition to their basal-like program such as EMT, as their scBasal and scClassical signatures are both relatively abundant with a higher scIC signatures as well.

Raghavan and colleagues recently identified a IC state of PDAC subtype that expresses both basal and classical markers, indicating the traditional classification of either a basal or classical subtype is limited and doesn't represent the molecular heterogeneity of PDAC at a cellular level (Raghavan et al., 2021). Indeed, from our RNA-seq data we found that both *KPten*$^{\Delta Acinar}$ and *KPten*$^{\Delta Duct}$ PDAC cells express gene signatures related to basal and classical subtype, but the direction of tendency towards each subtype is different. *KPten*$^{\Delta Duct}$ PDAC cells express a significant number of classical-related gene signatures in addition to their basal-related gene signatures. This might explain the lower magnitude in fold change in genes differentially expressed by *KPten*$^{\Delta Acinar}$ PDAC cells, as both cellular origins expressing genes associated with a classical phenotype, albeit with *KPten*$^{\Delta Acinar}$ PDAC cells express them at slightly higher levels than *KPten*$^{\Delta Duct}$ PDAC cells. On the other hand, the basal-like programs, such as EMT, that *KPten*$^{\Delta Duct}$ PDAC cells acquired are uniquely and strongly expressed by these cells only,

therefore producing a higher magnitude in fold change. In addition, Raghavan et al. also found scBasal PDAC had higher infiltration of *C1QC*+ TAMs, whereas scClassical PDAC had higher infiltration of *SPP1*+ TAMs (Raghavan et al., 2021). Interestingly, *KPten*$^{\Delta Duct}$ BMDMs had higher transcriptional levels (FPKM) of both *C1qc* (*KPten*$^{\Delta Duct}$ BMDMs:1893.51, 1726.88; *KPten*$^{\Delta Acinar}$ BMDMs:1615.7, 1600.69) and *Spp1* (*KPten*$^{\Delta Duct}$ BMDMs: 1450.6, 2133.94; *KPten*$^{\Delta Acinar}$ BMDMs: 691.126, 730.49), again indicating a more scIC-like subtype of the *KPten*$^{\Delta Duct}$ PDAC cell lines.

In addition, Raghavan and colleagues discovered that the TME of IC subtype PDAC is enriched in T cells, including CD8+ T cells and Tregs (Raghavan et al., 2021). This correlates with our previous findings that *KPten*$^{\Delta Duct/+}$ PDAC has more CD8+ T cell and Treg infiltration compared to *KPten*$^{\Delta Acinar/+}$ PDAC. Since the idea of an intermediate PDAC molecular subtype is still relatively new, how it and its T cells rich TME correlates with patient prognosis is still unknown. Future studies are necessary to investigate its correlation with prognosis and dissect the mechanism behind the potential correlation. I did not identify any studies linking GM-CSF expression with any of the PDAC molecular subtypes. Our study is the first to show the correlation between GM-CSF expression and a classical PDAC subtype. Future studies will be necessary to further investigate the correlation between PDAC molecular subtype and the expression of GM-CSF. Another limitation of our study is the small sample size for cell lines, and it is unknown how the PDAC molecular subtype and the polarized BMDMs phenotype might be with additional samples. As a result, future studies need to include additional samples to investigate the effect of cellular origin on PDAC molecular subtype and BMDM polarization more vigorously. Nonetheless, our results confirmed that cellular origin indeed affects molecular

subtype, with an acinar cell of origin strongly correlating with a classical PDAC phenotype and the ductal cell of origin having tendency towards a basal-like phenotype.

5.5 Closing remarks and future directions

I have shown the importance of cellular origin in the recruitment and progression of immune cell infiltration, the phenotype of macrophages, and the fundamental transcriptome of the PDAC cells. This might partially explain the immune heterogeneity seen in PDAC patients, as they have various degrees in the infiltration of myeloid cells and lymphocytes, with different levels of immune checkpoint expressions (Liudahl et al., 2021; Narayanan et al., 2021; Steele et al., 2020). As a result, it may be important to take the cellular origin into account when developing targeted immunotherapies for PDAC, as it might give clues about the patient's immune microenvironment. The limitations of our study are that our ductal mouse model developed primarily PB-IPMN as the precursor lesions, but ductal cells could also give rise to PanIN and other types of IPMN based on the genetic background (Collet et al., 2020; Kopp et al., 2018; Lee et al., 2019). As a result, future studies need to investigate if differences in precursor lesion histology play an important role in determining the immune microenvironment in PDAC derived from the ductal cell origin. In addition, studies using clinical samples are necessary to confirm our observation of the immune infiltration we found in PB-IPMN and the PDAC derived from it. It is still unknown if cellular origin and the differences in immune microenvironment have a role in determining prognosis clinically. Thus, future studies using scRNA-seq are crucial to investigate the cellular origin and the immune cell population of clinical PDAC samples.

References

Aguirre, A. J., Nowak, J. A., Camarda, N. D., Moffitt, R. A., Ghazani, A. A., Hazar-Rethinam, M., Raghavan, S., Kim, J., Brais, L. K., Ragon, D., Welch, M. W., Reilly, E., McCabe, D., Marini, L., Anderka, K., Helvie, K., Oliver, N., Babic, A., Da Silva, A., … Wolpin, B. M. (2018). Real-time Genomic Characterization of Advanced Pancreatic Cancer to Enable Precision Medicine. *Cancer Discovery*, *8*(9), 1096–1111. https://doi.org/10.1158/2159-8290.CD-18-0275

Aiello, N. M., Maddipati, R., Norgard, R. J., Balli, D., Li, J., Yuan, S., Yamazoe, T., Black, T., Sahmoud, A., Furth, E. E., Bar-Sagi, D., & Stanger, B. Z. (2018). EMT Subtype Influences Epithelial Plasticity and Mode of Cell Migration. *Developmental Cell*, *45*(6), 681-695.e4. https://doi.org/10.1016/j.devcel.2018.05.027

Asano, T., Yao, Y., Zhu, J., Li, D., Abbruzzese, J. L., & Reddy, S. A. G. (2004). The PI 3-kinase/Akt signaling pathway is activated due to aberrant Pten expression and targets transcription factors NF-κB and c-Myc in pancreatic cancer cells. *Oncogene*, *23*(53), 8571–8580. https://doi.org/10.1038/sj.onc.1207902

Babazadeh, S., Nassiri, S. M., Siavashi, V., Sahlabadi, M., Hajinasrollah, M., & Zamani-Ahmadmahmudi, M. (2021). Macrophage polarization by MSC-derived CXCL12 determines tumor growth. *Cellular & Molecular Biology Letters*, *26*(1), 30. https://doi.org/10.1186/s11658-021-00273-w

Baer, J. M., Zuo, C., Kang, L.-I., Alarcon de la Lastra, A., Borcherding, N. C., Knolhoff, B. L., Bogner, S. J., Zhu, Y., Lewis, M. A., Zhang, N., Kim, K.-W., Fields, R. C., Mills, J. C., Ding, L., Randolph, G. J., & DeNardo, D. G. (2022). Pancreas resident macrophage-induced fibrosis has divergent roles in pancreas inflammatory injury and PDAC. *BioRxiv*, 2022.02.09.479745. https://doi.org/10.1101/2022.02.09.479745

Bailey, J. M., Hendley, A. M., Lafaro, K. J., Pruski, M. A., Jones, N. C., Alsina, J., Younes, M., Maitra, A., McAllister, F., Iacobuzio-Donahue, C. A., & Leach, S. D. (2016). p53 mutations cooperate with oncogenic Kras to promote adenocarcinoma from pancreatic ductal cells. *Oncogene*, *35*(32), 4282–4288. https://doi.org/10.1038/onc.2015.441

Bailey, P., Chang, D. K., Nones, K., Johns, A. L., Patch, A.-M., Gingras, M.-C., Miller, D. K., Christ, A. N., Bruxner, T. J. C., Quinn, M. C., Nourse, C., Murtaugh, L. C., Harliwong, I., Idrisoglu, S., Manning, S., Nourbakhsh, E., Wani, S., Fink, L., Holmes, O., … Initiative, A. P. C. G. (2016). Genomic analyses identify molecular subtypes of pancreatic cancer. *Nature*, *531*(7592), 47–52. https://doi.org/10.1038/nature16965

Balachandran, V. P., Łuksza, M., Zhao, J. N., Makarov, V., Moral, J. A., Remark, R., Herbst, B., Askan, G., Bhanot, U., Senbabaoglu, Y., Wells, D. K., Cary, C. I. O., Grbovic-Huezo, O., Attiyeh, M., Medina, B., Zhang, J., Loo, J., Saglimbeni, J., Abu-Akeel, M., … Cancer, A.-N. C. for A. R. on. (2017). Identification of unique neoantigen qualities in long-term survivors of pancreatic cancer. *Nature*, *551*(7681), 512–516. https://doi.org/10.1038/nature24462

Basturk, O., Hong, S.-M., Wood, L. D., Adsay, N. V., Albores-Saavedra, J., Biankin, A. V, Brosens, L. A. A., Fukushima, N., Goggins, M., Hruban, R. H., Kato, Y., Klimstra, D. S., Klöppel, G., Krasinskas, A., Longnecker, D. S., Matthaei, H., Offerhaus, G. J. A., Shimizu, M., Takaori, K., … Meeting, B. C. (2015). A Revised Classification System and Recommendations From the Baltimore Consensus Meeting for Neoplastic Precursor Lesions in the Pancreas. *The American Journal of Surgical Pathology*, *39*(12), 1730–1741.

https://doi.org/10.1097/PAS.0000000000000533
Bayne, L. J., Beatty, G. L., Jhala, N., Clark, C. E., Rhim, A. D., Stanger, B. Z., & Vonderheide, R. H. (2012). Tumor-derived granulocyte-macrophage colony-stimulating factor regulates myeloid inflammation and T cell immunity in pancreatic cancer. *Cancer Cell*, *21*(6), 822–835. https://doi.org/10.1016/j.ccr.2012.04.025
Beatty, G. L., Winograd, R., Evans, R. A., Long, K. B., Luque, S. L., Lee, J. W., Clendenin, C., Gladney, W. L., Knoblock, D. M., Guirnalda, P. D., & Vonderheide, R. H. (2015a). Exclusion of T Cells From Pancreatic Carcinomas in Mice Is Regulated by Ly6Clow F4/80+ Extratumoral Macrophages. *Gastroenterology*, *149*(1), 201–210. https://doi.org/https://doi.org/10.1053/j.gastro.2015.04.010
Beatty, G. L., Winograd, R., Evans, R. A., Long, K. B., Luque, S. L., Lee, J. W., Clendenin, C., Gladney, W. L., Knoblock, D. M., Guirnalda, P. D., & Vonderheide, R. H. (2015b). Exclusion of T Cells From Pancreatic Carcinomas in Mice Is Regulated by Ly6C(low) F4/80(+) Extratumoral Macrophages. *Gastroenterology*, *149*(1), 201–210. https://doi.org/10.1053/j.gastro.2015.04.010
Bernard, V., Semaan, A., Huang, J., San Lucas, F. A., Mulu, F. C., Stephens, B. M., Guerrero, P. A., Huang, Y., Zhao, J., Kamyabi, N., Sen, S., Scheet, P. A., Taniguchi, C. M., Kim, M. P., Tzeng, C.-W., Katz, M. H., Singhi, A. D., Maitra, A., & Alvarez, H. A. (2019). Single-Cell Transcriptomics of Pancreatic Cancer Precursors Demonstrates Epithelial and Microenvironmental Heterogeneity as an Early Event in Neoplastic Progression. *Clinical Cancer Research*, *25*(7), 2194 LP – 2205. https://doi.org/10.1158/1078-0432.CCR-18-1955
Birnbaum, D. J., Finetti, P., Lopresti, A., Gilabert, M., Poizat, F., Turrini, O., Raoul, J.-L., Delpero, J.-R., Moutardier, V., Birnbaum, D., Mamessier, E., & Bertucci, F. (2016). Prognostic value of PDL1 expression in pancreatic cancer. *Oncotarget*, *7*(44), 71198–71210. https://doi.org/10.18632/oncotarget.11685
Blankenstein, T., Coulie, P. G., Gilboa, E., & Jaffee, E. M. (2012). The determinants of tumour immunogenicity. *Nature Reviews. Cancer*, *12*(4), 307–313. https://doi.org/10.1038/nrc3246
Borst, J., Ahrends, T., Bąbała, N., Melief, C. J. M., & Kastenmüller, W. (2018). CD4+ T cell help in cancer immunology and immunotherapy. *Nature Reviews Immunology*, *18*(10), 635–647. https://doi.org/10.1038/s41577-018-0044-0
Boyer, S., Lee, H.-J., Steele, N., Zhang, L., Sajjakulnukit, P., Andren, A., Ward, M. H., Singh, R., Basrur, V., Zhang, Y., Nesvizhskii, A. I., Pasca di Magliano, M., Halbrook, C. J., & Lyssiotis, C. A. (2022). Multiomic characterization of pancreatic cancer-associated macrophage polarization reveals deregulated metabolic programs driven by the GM-CSF–PI3K pathway. *ELife*, *11*, e73796. https://doi.org/10.7554/eLife.73796
Brasier, A. R. (2010). The nuclear factor-kappaB-interleukin-6 signalling pathway mediating vascular inflammation. *Cardiovascular Research*, *86*(2), 211–218. https://doi.org/10.1093/cvr/cvq076
Brenner, D. R., Weir, H. K., Demers, A. A., Ellison, L. F., Louzado, C., Shaw, A., Turner, D., Woods, R. R., & Smith, L. M. (2020). Projected estimates of cancer in Canada in 2020. *Canadian Medical Association Journal*, *192*(9), E199 LP-E205. https://doi.org/10.1503/cmaj.191292
Brouwer, T. P., Vahrmeijer, A. L., & de Miranda, N. F. C. C. (2021). Immunotherapy for pancreatic cancer: chasing the light at the end of the tunnel. *Cellular Oncology*, *44*(2), 261–278. https://doi.org/10.1007/s13402-021-00587-z
Bryant, K. L., Mancias, J. D., Kimmelman, A. C., & Der, C. J. (2014). KRAS: feeding pancreatic

cancer proliferation. *Trends in Biochemical Sciences*, *39*(2), 91–100. https://doi.org/10.1016/j.tibs.2013.12.004

Cao, Q., Wang, Y., Zheng, D., Sun, Y., Wang, C., Wang, X. M., Lee, V. W. S., Wang, Y., Zheng, G., Tan, T. K., Wang, Y. M., Alexander, S. I., & Harris, D. C. H. (2014). Failed renoprotection by alternatively activated bone marrow macrophages is due to a proliferation-dependent phenotype switch in vivo. *Kidney International*, *85*(4), 794–806. https://doi.org/10.1038/ki.2013.341

Carstens, J. L., Correa de Sampaio, P., Yang, D., Barua, S., Wang, H., Rao, A., Allison, J. P., LeBleu, V. S., & Kalluri, R. (2017). Spatial computation of intratumoral T cells correlates with survival of patients with pancreatic cancer. *Nature Communications*, *8*(1), 15095. https://doi.org/10.1038/ncomms15095

Chan-Seng-Yue, M., Kim, J. C., Wilson, G. W., Ng, K., Figueroa, E. F., O'Kane, G. M., Connor, A. A., Denroche, R. E., Grant, R. C., McLeod, J., Wilson, J. M., Jang, G. H., Zhang, A., Dodd, A., Liang, S.-B., Borgida, A., Chadwick, D., Kalimuthu, S., Lungu, I., … Notta, F. (2020). Transcription phenotypes of pancreatic cancer are driven by genomic events during tumor evolution. *Nature Genetics*, *52*(2), 231–240. https://doi.org/10.1038/s41588-019-0566-9

Choi, J. W., Kim, Y. J., Yun, K. A., Won, C. H., Lee, M. W., Choi, J. H., Chang, S. E., & Lee, W. J. (2020). The prognostic significance of VISTA and CD33-positive myeloid cells in cutaneous melanoma and their relationship with PD-1 expression. *Scientific Reports*, *10*(1), 14372. https://doi.org/10.1038/s41598-020-71216-2

Clark, C. E., Hingorani, S. R., Mick, R., Combs, C., Tuveson, D. A., & Vonderheide, R. H. (2007). Dynamics of the Immune Reaction to Pancreatic Cancer from Inception to Invasion. *Cancer Research*, *67*(19), 9518 LP – 9527. https://doi.org/10.1158/0008-5472.CAN-07-0175

Collet, L., Ghurburrun, E., Meyers, N., Assi, M., Pirlot, B., Leclercq, I. A., Couvelard, A., Komuta, M., Cros, J., Demetter, P., Lemaigre, F. P., Borbath, I., & Jacquemin, P. (2020). Kras and Lkb1 mutations synergistically induce intraductal papillary mucinous neoplasm derived from pancreatic duct cells. *Gut*, *69*(4), 704 LP – 714. https://doi.org/10.1136/gutjnl-2018-318059

Collisson, E. A., Sadanandam, A., Olson, P., Gibb, W. J., Truitt, M., Gu, S., Cooc, J., Weinkle, J., Kim, G. E., Jakkula, L., Feiler, H. S., Ko, A. H., Olshen, A. B., Danenberg, K. L., Tempero, M. A., Spellman, P. T., Hanahan, D., & Gray, J. W. (2011). Subtypes of pancreatic ductal adenocarcinoma and their differing responses to therapy. *Nature Medicine*, *17*(4), 500–503. https://doi.org/10.1038/nm.2344

Connor, A. A., & Gallinger, S. (2022). Pancreatic cancer evolution and heterogeneity: integrating omics and clinical data. *Nature Reviews Cancer*, *22*(3), 131–142. https://doi.org/10.1038/s41568-021-00418-1

Croxford, A. L., Lanzinger, M., Hartmann, F. J., Schreiner, B., Mair, F., Pelczar, P., Clausen, B. E., Jung, S., Greter, M., & Becher, B. (2015). The Cytokine GM-CSF Drives the Inflammatory Signature of $CCR2^{+}$ Monocytes and Licenses Autoimmunity. *Immunity*, *43*(3), 502–514. https://doi.org/10.1016/j.immuni.2015.08.010

Dal Molin, M., Hong, S.-M., Hebbar, S., Sharma, R., Scrimieri, F., de Wilde, R. F., Mayo, S. C., Goggins, M., Wolfgang, C. L., Schulick, R. D., Lin, M.-T., Eshleman, J. R., Hruban, R. H., Maitra, A., & Matthaei, H. (2012). Loss of expression of the SWI/SNF chromatin remodeling subunit BRG1/SMARCA4 is frequently observed in intraductal papillary

mucinous neoplasms of the pancreas. *Human Pathology*, *43*(4), 585–591. https://doi.org/10.1016/j.humpath.2011.06.009

Daniluk, J., Liu, Y., Deng, D., Chu, J., Huang, H., Gaiser, S., Cruz-Monserrate, Z., Wang, H., Ji, B., & Logsdon, C. D. (2012). An NF-κB pathway–mediated positive feedback loop amplifies Ras activity to pathological levels in mice. *The Journal of Clinical Investigation*, *122*(4), 1519–1528. https://doi.org/10.1172/JCI59743

Davies, L. C., Jenkins, S. J., Allen, J. E., & Taylor, P. R. (2013). Tissue-resident macrophages. *Nature Immunology*, *14*(10), 986–995. https://doi.org/10.1038/ni.2705

Distler, M, Aust, D., Weitz, J., Pilarsky, C., & Grützmann, R. (2014). Precursor Lesions for Sporadic Pancreatic Cancer: PanIN, IPMN, and MCN. *BioMed Research International*, *2014*, 474905. https://doi.org/10.1155/2014/474905

Distler, Marius, Kersting, S., Niedergethmann, M., Aust, D. E., Franz, M., Rückert, F., Ehehalt, F., Pilarsky, C., Post, S., Saeger, H.-D., & Grützmann, R. (2013). Pathohistological Subtype Predicts Survival in Patients With Intraductal Papillary Mucinous Neoplasm (IPMN) of the Pancreas. *Annals of Surgery*, *258*(2). https://journals.lww.com/annalsofsurgery/Fulltext/2013/08000/Pathohistological_Subtype_Predicts_Survival_in.20.aspx

Djurec, M., Graña, O., Lee, A., Troulé, K., Espinet, E., Cabras, L., Navas, C., Blasco, M. T., Martín-Díaz, L., Burdiel, M., Li, J., Liu, Z., Vallespinós, M., Sanchez-Bueno, F., Sprick, M. R., Trumpp, A., Sainz, B., Al-Shahrour, F., Rabadan, R., … Barbacid, M. (2018). Saa3 is a key mediator of the protumorigenic properties of cancer-associated fibroblasts in pancreatic tumors. *Proceedings of the National Academy of Sciences*, *115*(6), E1147 LP-E1156. https://doi.org/10.1073/pnas.1717802115

Ene-Obong, A., Clear, A. J., Watt, J., Wang, J., Fatah, R., Riches, J. C., Marshall, J. F., Chin-Aleong, J., Chelala, C., Gribben, J. G., Ramsay, A. G., & Kocher, H. M. (2013). Activated pancreatic stellate cells sequester CD8+ T cells to reduce their infiltration of the juxtatumoral compartment of pancreatic ductal adenocarcinoma. *Gastroenterology*, *145*(5), 1121–1132. https://doi.org/10.1053/j.gastro.2013.07.025

Eser, S., Schnieke, A., Schneider, G., & Saur, D. (2014). Oncogenic KRAS signalling in pancreatic cancer. *British Journal of Cancer*, *111*(5), 817–822. https://doi.org/10.1038/bjc.2014.215

Espinet, E., Gu, Z., Imbusch, C. D., Giese, N. A., Büscher, M., Safavi, M., Weisenburger, S., Klein, C., Vogel, V., Falcone, M., Insua-Rodríguez, J., Reitberger, M., Thiel, V., Kossi, S. O., Muckenhuber, A., Sarai, K., Lee, A. Y. L., Backx, E., Zarei, S., … Trumpp, A. (2021). Aggressive PDACs Show Hypomethylation of Repetitive Elements and the Execution of an Intrinsic IFN Program Linked to a Ductal Cell of Origin. *Cancer Discovery*, *11*(3), 638 LP – 659. https://doi.org/10.1158/2159-8290.CD-20-1202

Fan, J., Wang, M.-F., Chen, H.-L., Shang, D., Das, J. K., & Song, J. (2020). Current advances and outlooks in immunotherapy for pancreatic ductal adenocarcinoma. *Molecular Cancer*, *19*(1), 32. https://doi.org/10.1186/s12943-020-01151-3

Ferreira, R. M. M., Sancho, R., Messal, H. A., Nye, E., Spencer-Dene, B., Stone, R. K., Stamp, G., Rosewell, I., Quaglia, A., & Behrens, A. (2017). Duct- and Acinar-Derived Pancreatic Ductal Adenocarcinomas Show Distinct Tumor Progression and Marker Expression. *Cell Reports*, *21*(4), 966–978. https://doi.org/10.1016/j.celrep.2017.09.093

Flowers, B. M., Xu, H., Mulligan, A. S., Hanson, K. J., Seoane, J. A., Vogel, H., Curtis, C., Wood, L. D., & Attardi, L. D. (2021). Cell of Origin Influences Pancreatic Cancer Subtype.

Cancer Discovery, *11*(3), 660 LP – 677. https://doi.org/10.1158/2159-8290.CD-20-0633
Font-Burgada, J., Shalapour, S., Ramaswamy, S., Hsueh, B., Rossell, D., Umemura, A., Taniguchi, K., Nakagawa, H., Valasek, M. A., Ye, L., Kopp, J. L., Sander, M., Carter, H., Deisseroth, K., Verma, I. M., & Karin, M. (2015). Hybrid Periportal Hepatocytes Regenerate the Injured Liver without Giving Rise to Cancer. *Cell*, *162*(4), 766–779. https://doi.org/10.1016/j.cell.2015.07.026
Foucher, E. D., Ghigo, C., Chouaib, S., Galon, J., Iovanna, J., & Olive, D. (2018). Pancreatic Ductal Adenocarcinoma: A Strong Imbalance of Good and Bad Immunological Cops in the Tumor Microenvironment . In *Frontiers in Immunology* (Vol. 9, p. 1044). https://www.frontiersin.org/article/10.3389/fimmu.2018.01044
Gidekel Friedlander, S. Y., Chu, G. C., Snyder, E. L., Girnius, N., Dibelius, G., Crowley, D., Vasile, E., DePinho, R. A., & Jacks, T. (2009). Context-dependent transformation of adult pancreatic cells by oncogenic K-Ras. *Cancer Cell*, *16*(5), 379–389. https://doi.org/10.1016/j.ccr.2009.09.027
Gonzalez, H., Hagerling, C., & Werb, Z. (2018). Roles of the immune system in cancer: from tumor initiation to metastatic progression. *Genes & Development*, *32*(19–20), 1267–1284. https://doi.org/10.1101/gad.314617.118
Grant, T. J., Hua, K., & Singh, A. (2016). Molecular Pathogenesis of Pancreatic Cancer. *Progress in Molecular Biology and Translational Science*, *144*, 241–275. https://doi.org/10.1016/bs.pmbts.2016.09.008
Grossman, J. G., Nywening, T. M., Belt, B. A., Panni, R. Z., Krasnick, B. A., DeNardo, D. G., Hawkins, W. G., Goedegebuure, S. P., Linehan, D. C., & Fields, R. C. (2018). Recruitment of CCR2(+) tumor associated macrophage to sites of liver metastasis confers a poor prognosis in human colorectal cancer. *Oncoimmunology*, *7*(9), e1470729–e1470729. https://doi.org/10.1080/2162402X.2018.1470729
Grzywa, T. M., Sosnowska, A., Matryba, P., Rydzynska, Z., Jasinski, M., Nowis, D., & Golab, J. (2020). Myeloid Cell-Derived Arginase in Cancer Immune Response . In *Frontiers in Immunology* (Vol. 11). https://www.frontiersin.org/article/10.3389/fimmu.2020.00938
Gunaydin, G. (2021). CAFs Interacting With TAMs in Tumor Microenvironment to Enhance Tumorigenesis and Immune Evasion. *Frontiers in Oncology*, *11*, 668349. https://doi.org/10.3389/fonc.2021.668349
Guo, Q., Minnier, J., Burchard, J., Chiotti, K., Spellman, P., & Schedin, P. (2017). Physiologically activated mammary fibroblasts promote postpartum mammary cancer. *JCI Insight*, *2*(6), e89206–e89206. https://doi.org/10.1172/jci.insight.89206
Habbe, N., Shi, G., Meguid, R. A., Fendrich, V., Esni, F., Chen, H., Feldmann, G., Stoffers, D. A., Konieczny, S. F., Leach, S. D., & Maitra, A. (2008). Spontaneous induction of murine pancreatic intraepithelial neoplasia (mPanIN) by acinar cell targeting of oncogenic Kras in adult mice. *Proceedings of the National Academy of Sciences of the United States of America*, *105*(48), 18913–18918. https://doi.org/10.1073/pnas.0810097105
Haque, A. S. M. R., Moriyama, M., Kubota, K., Ishiguro, N., Sakamoto, M., Chinju, A., Mochizuki, K., Sakamoto, T., Kaneko, N., Munemura, R., Maehara, T., Tanaka, A., Hayashida, J.-N., Kawano, S., Kiyoshima, T., & Nakamura, S. (2019). CD206+ tumor-associated macrophages promote proliferation and invasion in oral squamous cell carcinoma via EGF production. *Scientific Reports*, *9*(1), 14611. https://doi.org/10.1038/s41598-019-51149-1
Hegde, S., Krisnawan, V. E., Herzog, B. H., Zuo, C., Breden, M. A., Knolhoff, B. L., Hogg, G.

D., Tang, J. P., Baer, J. M., Mpoy, C., Lee, K. B., Alexander, K. A., Rogers, B. E., Murphy, K. M., Hawkins, W. G., Fields, R. C., DeSelm, C. J., Schwarz, J. K., & DeNardo, D. G. (2020). Dendritic Cell Paucity Leads to Dysfunctional Immune Surveillance in Pancreatic Cancer. *Cancer Cell*, *37*(3), 289-307.e9. https://doi.org/10.1016/j.ccell.2020.02.008

Hennighausen, L., & Robinson, G. W. (2008). Interpretation of cytokine signaling through the transcription factors STAT5A and STAT5B. *Genes & Development*, *22*(6), 711–721. https://doi.org/10.1101/gad.1643908

Hill, R., Calvopina, J. H., Kim, C., Wang, Y., Dawson, D. W., Donahue, T. R., Dry, S., & Wu, H. (2010). PTEN loss accelerates KrasG12D-induced pancreatic cancer development. *Cancer Research*, *70*(18), 7114–7124. https://doi.org/10.1158/0008-5472.CAN-10-1649

Hingorani, S. R., Wang, L., Multani, A. S., Combs, C., Deramaudt, T. B., Hruban, R. H., Rustgi, A. K., Chang, S., & Tuveson, D. A. (2005). Trp53^{R172H} and <em>Kras^{G12D} cooperate to promote chromosomal instability and widely metastatic pancreatic ductal adenocarcinoma in mice. *Cancer Cell*, *7*(5), 469–483. https://doi.org/10.1016/j.ccr.2005.04.023

Hiraoka, N., Onozato, K., Kosuge, T., & Hirohashi, S. (2006). Prevalence of FOXP3 Regulatory T Cells Increases During the Progression of Pancreatic Ductal Adenocarcinoma and Its Premalignant Lesions. *Clinical Cancer Research*, *12*(18), 5423 LP – 5434. https://doi.org/10.1158/1078-0432.CCR-06-0369

Hosein, A. N., Dangol, G., Okumura, T., Roszik, J., Rajapakshe, K., Siemann, M., Zaid, M., Ghosh, B., Monberg, M., Guerrero, P. A., Singhi, A., Haymaker, C. L., Clevers, H., Abou-Elkacem, L., Woermann, S. M., & Maitra, A. (2022). Loss of Rnf43 Accelerates Kras-Mediated Neoplasia and Remodels the Tumor Immune Microenvironment in Pancreatic Adenocarcinoma. *Gastroenterology*. https://doi.org/10.1053/j.gastro.2021.12.273

Hosein, A. N., Huang, H., Wang, Z., Parmar, K., Du, W., Huang, J., Maitra, A., Olson, E., Verma, U., & Brekken, R. A. (2019). Cellular heterogeneity during mouse pancreatic ductal adenocarcinoma progression at single-cell resolution. *JCI Insight*, *4*(16). https://doi.org/10.1172/jci.insight.129212

Huang, H., Daniluk, J., Liu, Y., Chu, J., Li, Z., Ji, B., & Logsdon, C. D. (2014). Oncogenic K-Ras requires activation for enhanced activity. *Oncogene*, *33*(4), 532–535. https://doi.org/10.1038/onc.2012.619

Huen, S. C., Huynh, L., Marlier, A., Lee, Y., Moeckel, G. W., & Cantley, L. G. (2015). GM-CSF Promotes Macrophage Alternative Activation after Renal Ischemia/Reperfusion Injury. *Journal of the American Society of Nephrology : JASN*, *26*(6), 1334–1345. https://doi.org/10.1681/ASN.2014060612

Inman, K. S., Francis, A. A., & Murray, N. R. (2014). Complex role for the immune system in initiation and progression of pancreatic cancer. *World Journal of Gastroenterology*, *20*(32), 11160–11181. https://doi.org/10.3748/wjg.v20.i32.11160

Jarmin, D. I., Nibbs, R. J. B., Jamieson, T., de Bono, J. S., & Graham, G. J. (1999). Granulocyte macrophage colony-stimulating factor and interleukin-3 regulate chemokine and chemokine receptor expression in bone marrow macrophages. *Experimental Hematology*, *27*(12), 1735–1745. https://doi.org/10.1016/S0301-472X(99)00115-0

Ji, S., Qin, Y., Shi, S., Liu, X., Hu, H., Zhou, H., Gao, J., Zhang, B., Xu, W., Liu, J., Liang, D., Liu, L., Liu, C., Long, J., Zhou, H., Chiao, P. J., Xu, J., Ni, Q., Gao, D., & Yu, X. (2015). ERK kinase phosphorylates and destabilizes the tumor suppressor FBW7 in pancreatic

cancer. *Cell Research*, *25*(5), 561–573. https://doi.org/10.1038/cr.2015.30
Jones, L. M., Broz, M. L., Ranger, J. J., Ozcelik, J., Ahn, R., Zuo, D., Ursini-Siegel, J., Hallett, M. T., Krummel, M., & Muller, W. J. (2016). STAT3 Establishes an Immunosuppressive Microenvironment during the Early Stages of Breast Carcinogenesis to Promote Tumor Growth and Metastasis. *Cancer Research*, *76*(6), 1416–1428. https://doi.org/10.1158/0008-5472.CAN-15-2770
Joyce, J. A., & Fearon, D. T. (2015). T cell exclusion, immune privilege, and the tumor microenvironment. In *Science* (Vol. 348, Issue 6230, pp. 74–80). American Association for the Advancement of Science. https://doi.org/10.1126/science.aaa6204
Juiz, N. A., Iovanna, J., & Dusetti, N. (2019). Pancreatic Cancer Heterogeneity Can Be Explained Beyond the Genome. *Frontiers in Oncology*, *9*, 246. https://doi.org/10.3389/fonc.2019.00246
Ka, M., Daumas, A., Textoris, J., & Mege, J.-L. (2014). Phenotypic Diversity and Emerging New Tools to Study Macrophage Activation in Bacterial Infectious Diseases. *Frontiers in Immunology*, *5*, 500. https://doi.org/10.3389/fimmu.2014.00500
Karamitopoulou, E. (2019). Tumour microenvironment of pancreatic cancer: immune landscape is dictated by molecular and histopathological features. *British Journal of Cancer*, *121*(1), 5–14. https://doi.org/10.1038/s41416-019-0479-5
Khabipov, A., Käding, A., Liedtke, K., Freund, E., Partecke, L., & Bekeschus, S. (2019). RAW 264.7 Macrophage Polarization by Pancreatic Cancer Cells – A Model for Studying Tumour-promoting Macrophages. *Anticancer Research*, *39*, 2871–2882. https://doi.org/10.21873/anticanres.13416
Kim, J. C., Jung, Y. S., Lee, H. Y., Park, J. S., & Bae, Y.-S. (2017). Serum amyloid A inhibits dendritic cell differentiation by suppressing GM-CSF receptor expression and signaling. *Experimental & Molecular Medicine*, *49*(8), e369–e369. https://doi.org/10.1038/emm.2017.120
Kleeff, J., Korc, M., Apte, M., La Vecchia, C., Johnson, C. D., Biankin, A. V, Neale, R. E., Tempero, M., Tuveson, D. A., Hruban, R. H., & Neoptolemos, J. P. (2016). Pancreatic cancer. *Nature Reviews Disease Primers*, *2*(1), 16022. https://doi.org/10.1038/nrdp.2016.22
Kopinke, D., Brailsford, M., Pan, F. C., Magnuson, M. A., Wright, C. V. E., & Murtaugh, L. C. (2012). Ongoing Notch signaling maintains phenotypic fidelity in the adult exocrine pancreas. *Developmental Biology*, *362*(1), 57–64. https://doi.org/10.1016/j.ydbio.2011.11.010
Kopp, J. L., Dubois, C. L., Schaeffer, D. F., Samani, A., Taghizadeh, F., Cowan, R. W., Rhim, A. D., Stiles, B. L., Valasek, M., & Sander, M. (2018). Loss of Pten and Activation of Kras Synergistically Induce Formation of Intraductal Papillary Mucinous Neoplasia From Pancreatic Ductal Cells in Mice. *Gastroenterology*, *154*(5), 1509-1523.e5. https://doi.org/10.1053/j.gastro.2017.12.007
Kopp, J. L., von Figura, G., Mayes, E., Liu, F.-F., Dubois, C. L., Morris, J. P., Pan, F. C., Akiyama, H., Wright, C. V. E., Jensen, K., Hebrok, M., & Sander, M. (2012). Identification of Sox9-Dependent Acinar-to-Ductal Reprogramming as the Principal Mechanism for Initiation of Pancreatic Ductal Adenocarcinoma. *Cancer Cell*, *22*(6), 737–750. https://doi.org/https://doi.org/10.1016/j.ccr.2012.10.025
Kurtulus, S., Sakuishi, K., Ngiow, S.-F., Joller, N., Tan, D. J., Teng, M. W. L., Smyth, M. J., Kuchroo, V. K., & Anderson, A. C. (2015). TIGIT predominantly regulates the immune response via regulatory T cells. *The Journal of Clinical Investigation*, *125*(11), 4053–4062.

https://doi.org/10.1172/JCI81187
Lang, G. A., Iwakuma, T., Suh, Y.-A., Liu, G., Rao, V. A., Parant, J. M., Valentin-Vega, Y. A., Terzian, T., Caldwell, L. C., Strong, L. C., El-Naggar, A. K., & Lozano, G. (2004). Gain of Function of a p53 Hot Spot Mutation in a Mouse Model of Li-Fraumeni Syndrome. *Cell*, *119*(6), 861–872. https://doi.org/10.1016/j.cell.2004.11.006
Lankadasari, M. B., Mukhopadhyay, P., Mohammed, S., & Harikumar, K. B. (2019). TAMing pancreatic cancer: combat with a double edged sword. *Molecular Cancer*, *18*(1), 48. https://doi.org/10.1186/s12943-019-0966-6
Laskin, D. L., Heck, D. E., Gardner, C. R., Feder, L. S., & Laskin, J. D. (1994). Distinct patterns of nitric oxide production in hepatic macrophages and endothelial cells following acute exposure of rats to endotoxin. *Journal of Leukocyte Biology*, *56*(6), 751–758. https://doi.org/https://doi.org/10.1002/jlb.56.6.751
Lee, A. Y. L., Dubois, C. L., Sarai, K., Zarei, S., Schaeffer, D. F., Sander, M., & Kopp, J. L. (2019). Cell of origin affects tumour development and phenotype in pancreatic ductal adenocarcinoma. *Gut*, *68*(3), 487 LP – 498. https://doi.org/10.1136/gutjnl-2017-314426
Lesche, R., Groszer, M., Gao, J., Wang, Y., Messing, A., Sun, H., Liu, X., & Wu, H. (2002). Cre/loxP-mediated inactivation of the murine Pten tumor suppressor gene. *Genesis*, *32*(2), 148–149. https://doi.org/https://doi.org/10.1002/gene.10036
Lewis, D. E., & Blutt, S. E. (2019). *2 - Organization of the Immune System* (R. R. Rich, T. A. Fleisher, W. T. Shearer, H. W. Schroeder, A. J. Frew, & C. M. B. T.-C. I. (Fifth E. Weyand (eds.); pp. 19-38.e1). Elsevier. https://doi.org/https://doi.org/10.1016/B978-0-7020-6896-6.00002-8
Li, K.-Y., Yuan, J.-L., Trafton, D., Wang, J.-X., Niu, N., Yuan, C.-H., Liu, X.-B., & Zheng, L. (2020). Pancreatic ductal adenocarcinoma immune microenvironment and immunotherapy prospects. *Chronic Diseases and Translational Medicine*, *6*(1), 6–17. https://doi.org/10.1016/j.cdtm.2020.01.002
Liang, X., Sun, J., Wu, H., Luo, Y., Wang, L., Lu, J., Zhang, Z., Guo, J., Liang, Z., & Liu, T. (2018). PD-L1 in pancreatic ductal adenocarcinoma: a retrospective analysis of 373 Chinese patients using an in vitro diagnostic assay. *Diagnostic Pathology*, *13*(1), 5. https://doi.org/10.1186/s13000-017-0678-4
Liou, G.-Y., Bastea, L., Fleming, A., Döppler, H., Edenfield, B. H., Dawson, D. W., Zhang, L., Bardeesy, N., & Storz, P. (2017). The Presence of Interleukin-13 at Pancreatic ADM/PanIN Lesions Alters Macrophage Populations and Mediates Pancreatic Tumorigenesis. *Cell Reports*, *19*(7), 1322–1333. https://doi.org/10.1016/j.celrep.2017.04.052
Liou, G.-Y., Döppler, H., Necela, B., Krishna, M., Crawford, H. C., Raimondo, M., & Storz, P. (2013). Macrophage-secreted cytokines drive pancreatic acinar-to-ductal metaplasia through NF-κB and MMPs. *The Journal of Cell Biology*, *202*(3), 563–577. https://doi.org/10.1083/jcb.201301001
Liu, L., Zhao, G., Wu, W., Rong, Y., Jin, D., Wang, D., Lou, W., & Qin, X. (2016). Low intratumoral regulatory T cells and high peritumoral CD8+ T cells relate to long-term survival in patients with pancreatic ductal adenocarcinoma after pancreatectomy. *Cancer Immunology, Immunotherapy*, *65*(1), 73–82. https://doi.org/10.1007/s00262-015-1775-4
Liudahl, S. M., Betts, C. B., Sivagnanam, S., Morales-Oyarvide, V., da Silva, A., Yuan, C., Hwang, S., Grossblatt-Wait, A., Leis, K. R., Larson, W., Lavoie, M. B., Robinson, P., Dias Costa, A., Väyrynen, S. A., Clancy, T. E., Rubinson, D. A., Link, J., Keith, D., Horton, W., … Coussens, L. M. (2021). Leukocyte Heterogeneity in Pancreatic Ductal

Adenocarcinoma: Phenotypic and Spatial Features Associated with Clinical Outcome. *Cancer Discovery*. https://doi.org/10.1158/2159-8290.CD-20-0841

Lohneis, P., Sinn, M., Bischoff, S., Jühling, A., Pelzer, U., Wislocka, L., Bahra, M., Sinn, B. V, Denkert, C., Oettle, H., Bläker, H., Riess, H., Jöhrens, K., & Striefler, J. K. (2017). Cytotoxic tumour-infiltrating T lymphocytes influence outcome in resected pancreatic ductal adenocarcinoma. *European Journal of Cancer*, *83*, 290–301. https://doi.org/https://doi.org/10.1016/j.ejca.2017.06.016

Magnuson, M. A., & Osipovich, A. B. (2013). Pancreas-specific Cre driver lines and considerations for their prudent use. *Cell Metabolism*, *18*(1), 9–20. https://doi.org/10.1016/j.cmet.2013.06.011

Martens, S., Lefesvre, P., Nicolle, R., Biankin, A. V, Puleo, F., Van Laethem, J. L., & Rooman, I. (2019). Different shades of pancreatic ductal adenocarcinoma, different paths towards precision therapeutic applications. *Annals of Oncology*, *30*(9), 1428–1436. https://doi.org/10.1093/annonc/mdz181

Marzec, M., Zhang, Q., Goradia, A., Raghunath, P. N., Liu, X., Paessler, M., Wang, H. Y., Wysocka, M., Cheng, M., Ruggeri, B. A., & Wasik, M. A. (2008). Oncogenic kinase NPM/ALK induces through STAT3 expression of immunosuppressive protein CD274 (PD-L1, B7-H1). *Proceedings of the National Academy of Sciences*, *105*(52), 20852 LP – 20857. https://doi.org/10.1073/pnas.0810958105

Masetti, M., Carriero, R., Portale, F., Marelli, G., Morina, N., Pandini, M., Iovino, M., Partini, B., Erreni, M., Ponzetta, A., Magrini, E., Colombo, P., Elefante, G., Colombo, F. S., den Haan, J. M. M., Peano, C., Cibella, J., Termanini, A., Kunderfranco, P., … Di Mitri, D. (2021). Lipid-loaded tumor-associated macrophages sustain tumor growth and invasiveness in prostate cancer. *Journal of Experimental Medicine*, *219*(2), e20210564. https://doi.org/10.1084/jem.20210564

McGinnis, T., Bantis, L. E., Madan, R., Dandawate, P., Kumer, S., Schmitt, T., Paluri, R. K., & Kasi, A. (2020). Survival Outcomes of Pancreatic Intraepithelial Neoplasm (PanIN) versus Intraductal Papillary Mucinous Neoplasm (IPMN) Associated Pancreatic Adenocarcinoma. *Journal of Clinical Medicine*, *9*(10), 3102. https://doi.org/10.3390/jcm9103102

Mino-Kenudson, M., Fernández-del Castillo, C., Baba, Y., Valsangkar, N. P., Liss, A. S., Hsu, M., Correa-Gallego, C., Ingkakul, T., Perez Johnston, R., Turner, B. G., Androutsopoulos, V., Deshpande, V., McGrath, D., Sahani, D. V, Brugge, W. R., Ogino, S., Pitman, M. B., Warshaw, A. L., & Thayer, S. P. (2011). Prognosis of invasive intraductal papillary mucinous neoplasm depends on histological and precursor epithelial subtypes. *Gut*, *60*(12), 1712–1720. https://doi.org/10.1136/gut.2010.232272

Moffitt, R. A., Marayati, R., Flate, E. L., Volmar, K. E., Loeza, S. G. H., Hoadley, K. A., Rashid, N. U., Williams, L. A., Eaton, S. C., Chung, A. H., Smyla, J. K., Anderson, J. M., Kim, H. J., Bentrem, D. J., Talamonti, M. S., Iacobuzio-Donahue, C. A., Hollingsworth, M. A., & Yeh, J. J. (2015). Virtual microdissection identifies distinct tumor- and stroma-specific subtypes of pancreatic ductal adenocarcinoma. *Nature Genetics*, *47*(10), 1168–1178. https://doi.org/10.1038/ng.3398

Murakami, T., Hiroshima, Y., Matsuyama, R., Homma, Y., Hoffman, R. M., & Endo, I. (2019). Role of the tumor microenvironment in pancreatic cancer. *Annals of Gastroenterological Surgery*, *3*(2), 130–137. https://doi.org/10.1002/ags3.12225

Narayanan, S., Vicent, S., & Ponz-Sarvisé, M. (2021). PDAC as an Immune Evasive Disease: Can 3D Model Systems Aid to Tackle This Clinical Problem? . In *Frontiers in Cell and*

Developmental Biology (Vol. 9). https://www.frontiersin.org/article/10.3389/fcell.2021.787249

Noë, M., Niknafs, N., Fischer, C. G., Hackeng, W. M., Beleva Guthrie, V., Hosoda, W., Debeljak, M., Papp, E., Adleff, V., White, J. R., Luchini, C., Pea, A., Scarpa, A., Butturini, G., Zamboni, G., Castelli, P., Hong, S.-M., Yachida, S., Hiraoka, N., … Wood, L. D. (2020). Genomic characterization of malignant progression in neoplastic pancreatic cysts. *Nature Communications*, *11*(1), 4085. https://doi.org/10.1038/s41467-020-17917-8

Nyati, K. K., Agarwal, R. G., Sharma, P., & Kishimoto, T. (2019). Arid5a Regulation and the Roles of Arid5a in the Inflammatory Response and Disease . In *Frontiers in Immunology* (Vol. 10). https://www.frontiersin.org/article/10.3389/fimmu.2019.02790

Ohue, Y., & Nishikawa, H. (2019). Regulatory T (Treg) cells in cancer: Can Treg cells be a new therapeutic target? *Cancer Science*, *110*(7), 2080–2089. https://doi.org/10.1111/cas.14069

Oleinika, K., Nibbs, R. J., Graham, G. J., & Fraser, A. R. (2013). Suppression, subversion and escape: the role of regulatory T cells in cancer progression. *Clinical and Experimental Immunology*, *171*(1), 36–45. https://doi.org/10.1111/j.1365-2249.2012.04657.x

Orecchioni, M., Ghosheh, Y., Pramod, A. B., & Ley, K. (2019). Macrophage Polarization: Different Gene Signatures in M1(LPS+) vs. Classically and M2(LPS–) vs. Alternatively Activated Macrophages . In *Frontiers in Immunology* (Vol. 10, p. 1084). https://www.frontiersin.org/article/10.3389/fimmu.2019.01084

Otero, K., Turnbull, I. R., Poliani, P. L., Vermi, W., Cerutti, E., Aoshi, T., Tassi, I., Takai, T., Stanley, S. L., Miller, M., Shaw, A. S., & Colonna, M. (2009). Macrophage colony-stimulating factor induces the proliferation and survival of macrophages via a pathway involving DAP12 and beta-catenin. *Nature Immunology*, *10*(7), 734–743. https://doi.org/10.1038/ni.1744

Parajuli, B., Sonobe, Y., Kawanokuchi, J., Doi, Y., Noda, M., Takeuchi, H., Mizuno, T., & Suzumura, A. (2012). GM-CSF increases LPS-induced production of proinflammatory mediators via upregulation of TLR4 and CD14 in murine microglia. *Journal of Neuroinflammation*, *9*(1), 268. https://doi.org/10.1186/1742-2094-9-268

Passarelli, A., Mannavola, F., Stucci, L. S., Tucci, M., & Silvestris, F. (2017). Immune system and melanoma biology: a balance between immunosurveillance and immune escape. *Oncotarget*, *8*(62), 106132–106142. https://doi.org/10.18632/oncotarget.22190

Patil, S., Dou, Y., & Kopp, J. L. (2021). Cell Type of Pancreatic Ductal Adenocarcinoma Origin: Implications for Prognosis and Clinical Outcomes. *Visceral Medicine*. https://doi.org/10.1159/000520946

Petty, A. J., Dai, R., Lapalombella, R., Baiocchi, R. A., Benson, D. M., Li, Z., Huang, X., & Yang, Y. (2021). Hedgehog-induced PD-L1 on tumor-associated macrophages is critical for suppression of tumor-infiltrating CD8+ T cell function. *JCI Insight*, *6*(6). https://doi.org/10.1172/jci.insight.146707

Pitarresi, J. R., Liu, X., Sharma, S. M., Cuitiño, M. C., Kladney, R. D., Mace, T. A., Donohue, S., Nayak, S. G., Qu, C., Lee, J., Woelke, S. A., Trela, S., LaPak, K., Yu, L., McElroy, J., Rosol, T. J., Shakya, R., Ludwig, T., Lesinski, G. B., … Ostrowski, M. C. (2016). Stromal ETS2 Regulates Chemokine Production and Immune Cell Recruitment during Acinar-to-Ductal Metaplasia. *Neoplasia*, *18*(9), 541–552. https://doi.org/https://doi.org/10.1016/j.neo.2016.07.006

Pulido, R. (2018). PTEN Inhibition in Human Disease Therapy. *Molecules (Basel, Switzerland)*, *23*(2), 285. https://doi.org/10.3390/molecules23020285

Pylayeva-Gupta, Y., Lee, K. E., Hajdu, C. H., Miller, G., & Bar-Sagi, D. (2012). Oncogenic Kras-induced GM-CSF production promotes the development of pancreatic neoplasia. *Cancer Cell*, *21*(6), 836–847. https://doi.org/10.1016/j.ccr.2012.04.024

Qualls, J. E., & Murray, P. J. (2011). Chapter ten - Tumor Macrophages: Protective and Pathogenic Roles in Cancer Development. In M. A. B. T.-C. T. in D. B. Dyer (Ed.), *Cancer and Development* (Vol. 94, pp. 309–328). Academic Press. https://doi.org/https://doi.org/10.1016/B978-0-12-380916-2.00010-3

Raghavan, S., Winter, P. S., Navia, A. W., Williams, H. L., DenAdel, A., Lowder, K. E., Galvez-Reyes, J., Kalekar, R. L., Mulugeta, N., Kapner, K. S., Raghavan, M. S., Borah, A. A., Liu, N., Väyrynen, S. A., Costa, A. D., Ng, R. W. S., Wang, J., Hill, E. K., Ragon, D. Y., … Shalek, A. K. (2021). Microenvironment drives cell state, plasticity, and drug response in pancreatic cancer. *Cell*, *184*(25), 6119-6137.e26. https://doi.org/10.1016/j.cell.2021.11.017

Raskov, H., Orhan, A., Christensen, J. P., & Gögenur, I. (2021). Cytotoxic CD8+ T cells in cancer and cancer immunotherapy. *British Journal of Cancer*, *124*(2), 359–367. https://doi.org/10.1038/s41416-020-01048-4

Raskov, H., Orhan, A., Gaggar, S., & Gögenur, I. (2021). Cancer-Associated Fibroblasts and Tumor-Associated Macrophages in Cancer and Cancer Immunotherapy . In *Frontiers in Oncology* (Vol. 11). https://www.frontiersin.org/article/10.3389/fonc.2021.668731

Reichert, M., Takano, S., Heeg, S., Bakir, B., Botta, G. P., & Rustgi, A. K. (2013). Isolation, culture and genetic manipulation of mouse pancreatic ductal cells. *Nature Protocols*, *8*(7), 1354–1365. https://doi.org/10.1038/nprot.2013.079

Rhim, A. D., & Stanger, B. Z. (2010). Molecular biology of pancreatic ductal adenocarcinoma progression: aberrant activation of developmental pathways. *Progress in Molecular Biology and Translational Science*, *97*, 41–78. https://doi.org/10.1016/B978-0-12-385233-5.00002-7

Riva, G., Pea, A., Pilati, C., Fiadone, G., Lawlor, R. T., Scarpa, A., & Luchini, C. (2018). Histo-molecular oncogenesis of pancreatic cancer: From precancerous lesions to invasive ductal adenocarcinoma. *World Journal of Gastrointestinal Oncology*, *10*(10), 317–327. https://doi.org/10.4251/wjgo.v10.i10.317

Rossi Sebastiano, M., Pozzato, C., Saliakoura, M., Yang, Z., Peng, R.-W., Galié, M., Oberson, K., Simon, H.-U., Karamitopoulou, E., & Konstantinidou, G. (2020). ACSL3-PAI-1 signaling axis mediates tumor-stroma cross-talk promoting pancreatic cancer progression. *Science Advances*, *6*. https://doi.org/10.1126/sciadv.abb9200

Rőszer, T. (2015). Understanding the Mysterious M2 Macrophage through Activation Markers and Effector Mechanisms. *Mediators of Inflammation*, *2015*, 816460. https://doi.org/10.1155/2015/816460

Roth, S., Zamzow, K., Gaida, M. M., Heikenwälder, M., Tjaden, C., Hinz, U., Bose, P., Michalski, C. W., & Hackert, T. (2020). Evolution of the immune landscape during progression of pancreatic intraductal papillary mucinous neoplasms to invasive cancer. *EBioMedicine*, *54*, 102714. https://doi.org/10.1016/j.ebiom.2020.102714

Roy, N., Malik, S., Villanueva, K. E., Urano, A., Lu, X., Von Figura, G., Seeley, E. S., Dawson, D. W., Collisson, E. A., & Hebrok, M. (2015). Brg1 promotes both tumor-suppressive and oncogenic activities at distinct stages of pancreatic cancer formation. *Genes & Development*, *29*(6), 658–671. https://doi.org/10.1101/gad.256628.114

Ruffolo, L. I., Jackson, K. M., Kuhlers, P. C., Dale, B. S., Figueroa Guilliani, N. M., Ullman, N. A., Burchard, P. R., Qin, S. S., Juviler, P. G., Keilson, J. M., Morrison, A. B., Georger, M.,

Jewell, R., Calvi, L. M., Nywening, T. M., O'Dell, M. R., Hezel, A. F., De Las Casas, L., Lesinski, G. B., … Linehan, D. C. (2021). GM-CSF drives myelopoiesis, recruitment and polarisation of tumour-associated macrophages in cholangiocarcinoma and systemic blockade facilitates antitumour immunity. *Gut*, gutjnl-2021-324109. https://doi.org/10.1136/gutjnl-2021-324109

Schizas, D., Charalampakis, N., Kole, C., Economopoulou, P., Koustas, E., Gkotsis, E., Ziogas, D., Psyrri, A., & Karamouzis, M. V. (2020). Immunotherapy for pancreatic cancer: A 2020 update. *Cancer Treatment Reviews*, *86*. https://doi.org/10.1016/j.ctrv.2020.102016

Schlesinger, Y., Yosefov-Levi, O., Kolodkin-Gal, D., Granit, R. Z., Peters, L., Kalifa, R., Xia, L., Nasereddin, A., Shiff, I., Amran, O., Nevo, Y., Elgavish, S., Atlan, K., Zamir, G., & Parnas, O. (2020). Single-cell transcriptomes of pancreatic preinvasive lesions and cancer reveal acinar metaplastic cells' heterogeneity. *Nature Communications*, *11*(1), 4516. https://doi.org/10.1038/s41467-020-18207-z

Shain, A. H., Giacomini, C. P., Matsukuma, K., Karikari, C. A., Bashyam, M. D., Hidalgo, M., Maitra, A., & Pollack, J. R. (2012). Convergent structural alterations define SWItch/Sucrose NonFermentable (SWI/SNF) chromatin remodeler as a central tumor suppressive complex in pancreatic cancer. *Proceedings of the National Academy of Sciences*, *109*(5), E252 LP-E259. https://doi.org/10.1073/pnas.1114817109

Shapouri-Moghaddam, A., Mohammadian, S., Vazini, H., Taghadosi, M., Esmaeili, S.-A., Mardani, F., Seifi, B., Mohammadi, A., Afshari, J. T., & Sahebkar, A. (2018). Macrophage plasticity, polarization, and function in health and disease. *Journal of Cellular Physiology*, *233*(9), 6425–6440. https://doi.org/https://doi.org/10.1002/jcp.26429

Shiraishi, D., Fujiwara, Y., Horlad, H., Saito, Y., Iriki, T., Tsuboki, J., Cheng, P., Nakagata, N., Mizuta, H., Bekki, H., Nakashima, Y., Oda, Y., Takeya, M., & Komohara, Y. (2018). CD163 Is Required for Protumoral Activation of Macrophages in Human and Murine Sarcoma. *Cancer Research*, *78*(12), 3255–3266. https://doi.org/10.1158/0008-5472.CAN-17-2011

Siegel, R. L., Miller, K. D., Fuchs, H. E., & Jemal, A. (2021). Cancer Statistics, 2021. *CA: A Cancer Journal for Clinicians*, *71*(1), 7–33. https://doi.org/https://doi.org/10.3322/caac.21654

Singhi, A. D., & Wood, L. D. (2021). Early detection of pancreatic cancer using DNA-based molecular approaches. *Nature Reviews Gastroenterology & Hepatology*, *18*(7), 457–468. https://doi.org/10.1038/s41575-021-00470-0

Sivakumar, S., Abu-Shah, E., Ahern, D. J., Arbe-Barnes, E. H., Jainarayanan, A. K., Mangal, N., Reddy, S., Rendek, A., Easton, A., Kurz, E., Silva, M., Soonawalla, Z., Heij, L. R., Bashford-Rogers, R., Middleton, M. R., & Dustin, M. L. (2021). Activated Regulatory T-Cells, Dysfunctional and Senescent T-Cells Hinder the Immunity in Pancreatic Cancer. *Cancers*, *13*(8), 1776. https://doi.org/10.3390/cancers13081776

Sottnik, J. L., Dai, J., Zhang, H., Campbell, B., & Keller, E. T. (2015). Tumor-induced pressure in the bone microenvironment causes osteocytes to promote the growth of prostate cancer bone metastases. *Cancer Research*, *75*(11), 2151–2158. https://doi.org/10.1158/0008-5472.CAN-14-2493

Srinivas, S., Watanabe, T., Lin, C. S., William, C. M., Tanabe, Y., Jessell, T. M., & Costantini, F. (2001). Cre reporter strains produced by targeted insertion of EYFP and ECFP into the ROSA26 locus. *BMC Developmental Biology*, *1*, 4. https://doi.org/10.1186/1471-213x-1-4

Stanger, B. Z., Stiles, B., Lauwers, G. Y., Bardeesy, N., Mendoza, M., Wang, Y., Greenwood,

A., Cheng, K., McLaughlin, M., Brown, D., DePinho, R. A., Wu, H., Melton, D. A., & Dor, Y. (2005). Pten constrains centroacinar cell expansion and malignant transformation in the pancreas. *Cancer Cell*, *8*(3), 185–195. https://doi.org/10.1016/j.ccr.2005.07.015

Steele, N. G., Carpenter, E. S., Kemp, S. B., Sirihorachai, V. R., The, S., Delrosario, L., Lazarus, J., Amir, E. D., Gunchick, V., Espinoza, C., Bell, S., Harris, L., Lima, F., Irizarry-Negron, V., Paglia, D., Macchia, J., Chu, A. K. Y., Schofield, H., Wamsteker, E.-J., … Pasca di Magliano, M. (2020). Multimodal mapping of the tumor and peripheral blood immune landscape in human pancreatic cancer. *Nature Cancer*, *1*(11), 1097–1112. https://doi.org/10.1038/s43018-020-00121-4

Storz, P., & Crawford, H. C. (2020). Carcinogenesis of Pancreatic Ductal Adenocarcinoma. *Gastroenterology*, *158*(8), 2072–2081. https://doi.org/https://doi.org/10.1053/j.gastro.2020.02.059

Stromnes, I. M., Hulbert, A., Pierce, R. H., Greenberg, P. D., & Hingorani, S. R. (2017). T-cell Localization, Activation, and Clonal Expansion in Human Pancreatic Ductal Adenocarcinoma. *Cancer Immunology Research*, *5*(11), 978–991. https://doi.org/10.1158/2326-6066.CIR-16-0322

Takata, K., Kozaki, T., Lee, C. Z. W., Thion, M. S., Otsuka, M., Lim, S., Utami, K. H., Fidan, K., Park, D. S., Malleret, B., Chakarov, S., See, P., Low, D., Low, G., Garcia-Miralles, M., Zeng, R., Zhang, J., Goh, C. C., Gul, A., … Ginhoux, F. (2017). Induced-Pluripotent-Stem-Cell-Derived Primitive Macrophages Provide a Platform for Modeling Tissue-Resident Macrophage Differentiation and Function. *Immunity*, *47*(1), 183-198.e6. https://doi.org/10.1016/j.immuni.2017.06.017

Takeya, M., & Komohara, Y. (2016). Role of tumor-associated macrophages in human malignancies: friend or foe?: TAMs in human malignancies. *Pathology International*, *66*. https://doi.org/10.1111/pin.12440

Talbert, E. E., Cuitiño, M. C., Ladner, K. J., Rajasekerea, P. V, Siebert, M., Shakya, R., Leone, G. W., Ostrowski, M. C., Paleo, B., Weisleder, N., Reiser, P. J., Webb, A., Timmers, C. D., Eiferman, D. S., Evans, D. C., Dillhoff, M. E., Schmidt, C. R., & Guttridge, D. C. (2019). Modeling Human Cancer-induced Cachexia. *Cell Reports*, *28*(6), 1612-1622.e4. https://doi.org/10.1016/j.celrep.2019.07.016

Thorn, M., Guha, P., Cunetta, M., Espat, N. J., Miller, G., Junghans, R. P., & Katz, S. C. (2016). Tumor-associated GM-CSF overexpression induces immunoinhibitory molecules via STAT3 in myeloid-suppressor cells infiltrating liver metastases. *Cancer Gene Therapy*, *23*(6), 188–198. https://doi.org/10.1038/cgt.2016.19

Tiberti, S., & Nezi, L. (2020). Accumulation of Long-Chain Fatty Acids in the Tumor Microenvironment Drives Dysfunction in Intrapancreatic CD8+ T Cells. *Journal of Experimental Medicine*, *217*. https://doi.org/10.1084/jem.20191920

Toda, G., Yamauchi, T., Kadowaki, T., & Ueki, K. (2021). Preparation and culture of bone marrow-derived macrophages from mice for functional analysis. *STAR Protocols*, *2*(1), 100246. https://doi.org/https://doi.org/10.1016/j.xpro.2020.100246

Tsuda, M., Fukuda, A., Roy, N., Hiramatsu, Y., Leonhardt, L., Kakiuchi, N., Hoyer, K., Ogawa, S., Goto, N., Ikuta, K., Kimura, Y., Matsumoto, Y., Takada, Y., Yoshioka, T., Maruno, T., Yamaga, Y., Kim, G. E., Akiyama, H., Ogawa, S., … Seno, H. (2018). The BRG1/SOX9 axis is critical for acinar cell-derived pancreatic tumorigenesis. *The Journal of Clinical Investigation*, *128*(8), 3475–3489. https://doi.org/10.1172/JCI94287

Tu, M., Klein, L., Espinet, E., Georgomanolis, T., Wegwitz, F., Li, X., Urbach, L., Danieli-Mackay, A., Küffer, S., Bojarczuk, K., Mizi, A., Günesdogan, U., Chapuy, B., Gu, Z., Neesse, A., Kishore, U., Ströbel, P., Hessmann, E., Hahn, S. A., … Singh, S. K. (2021). TNF-α-producing macrophages determine subtype identity and prognosis via AP1 enhancer reprogramming in pancreatic cancer. *Nature Cancer*, *2*(11), 1185–1203. https://doi.org/10.1038/s43018-021-00258-w

Tuveson, D. A., Shaw, A. T., Willis, N. A., Silver, D. P., Jackson, E. L., Chang, S., Mercer, K. L., Grochow, R., Hock, H., Crowley, D., Hingorani, S. R., Zaks, T., King, C., Jacobetz, M. A., Wang, L., Bronson, R. T., Orkin, S. H., DePinho, R. A., & Jacks, T. (2004). Endogenous oncogenic K-ras^{G12D} stimulates proliferation and widespread neoplastic and developmental defects. *Cancer Cell*, *5*(4), 375–387. https://doi.org/10.1016/S1535-6108(04)00085-6

van Dalen, F. J., van Stevendaal, M. H. M. E., Fennemann, F. L., Verdoes, M., & Ilina, O. (2018). Molecular Repolarisation of Tumour-Associated Macrophages. *Molecules (Basel, Switzerland)*, *24*(1), 9. https://doi.org/10.3390/molecules24010009

Velez-Delgado, A., Donahue, K. L., Brown, K. L., Du, W., Irizarry-Negron, V., Menjivar, R. E., Lasse Opsahl, E. L., Steele, N. G., The, S., Lazarus, J., Sirihorachai, V. R., Yan, W., Kemp, S. B., Kerk, S. A., Bollampally, M., Yang, S., Scales, M. K., Avritt, F. R., Lima, F., … Pasca di Magliano, M. (2022). Extrinsic KRAS Signaling Shapes the Pancreatic Microenvironment Through Fibroblast Reprogramming. *Cellular and Molecular Gastroenterology and Hepatology*, *13*(6), 1673–1699. https://doi.org/10.1016/j.jcmgh.2022.02.016

von Figura, G., Fukuda, A., Roy, N., Liku, M. E., Morris Iv, J. P., Kim, G. E., Russ, H. A., Firpo, M. A., Mulvihill, S. J., Dawson, D. W., Ferrer, J., Mueller, W. F., Busch, A., Hertel, K. J., & Hebrok, M. (2014). The chromatin regulator Brg1 suppresses formation of intraductal papillary mucinous neoplasm and pancreatic ductal adenocarcinoma. *Nature Cell Biology*, *16*(3), 255–267. https://doi.org/10.1038/ncb2916

Vuilleumier, R., Lian, T., Flibotte, S., Khan, Z. N., Fuchs, A., Pyrowolakis, G., & Allan, D. W. (2019). Retrograde BMP signaling activates neuronal gene expression through widespread deployment of a conserved BMP-responsive cis-regulatory activation element. *Nucleic Acids Research*, *47*(2), 679–699. https://doi.org/10.1093/nar/gky1135

Waddell, N., Pajic, M., Patch, A.-M., Chang, D. K., Kassahn, K. S., Bailey, P., Johns, A. L., Miller, D., Nones, K., Quek, K., Quinn, M. C. J., Robertson, A. J., Fadlullah, M. Z. H., Bruxner, T. J. C., Christ, A. N., Harliwong, I., Idrisoglu, S., Manning, S., Nourse, C., … Service, G. G. & C. N. H. (2015). Whole genomes redefine the mutational landscape of pancreatic cancer. *Nature*, *518*(7540), 495–501. https://doi.org/10.1038/nature14169

Wartenberg, M., Cibin, S., Zlobec, I., Vassella, E., Eppenberger-Castori, S., Terracciano, L., Eichmann, M. D., Worni, M., Gloor, B., Perren, A., & Karamitopoulou, E. (2018). Integrated Genomic and Immunophenotypic Classification of Pancreatic Cancer Reveals Three Distinct Subtypes with Prognostic/Predictive Significance. *Clinical Cancer Research*, *24*(18), 4444 LP – 4454. https://doi.org/10.1158/1078-0432.CCR-17-3401

Wu, K., Lin, K., Li, X., Yuan, X., Xu, P., Ni, P., & Xu, D. (2020). Redefining Tumor-Associated Macrophage Subpopulations and Functions in the Tumor Microenvironment . In *Frontiers in Immunology* (Vol. 11). https://www.frontiersin.org/article/10.3389/fimmu.2020.01731

Xiang, X., Wang, J., Lu, D., & Xu, X. (2021). Targeting tumor-associated macrophages to synergize tumor immunotherapy. *Signal Transduction and Targeted Therapy*, *6*(1), 75.

https://doi.org/10.1038/s41392-021-00484-9
Xie, Z., Bailey, A., Kuleshov, M. V, Clarke, D. J. B., Evangelista, J. E., Jenkins, S. L., Lachmann, A., Wojciechowicz, M. L., Kropiwnicki, E., Jagodnik, K. M., Jeon, M., & Ma'ayan, A. (2021). Gene Set Knowledge Discovery with Enrichr. *Current Protocols*, *1*(3), e90. https://doi.org/https://doi.org/10.1002/cpz1.90
Xu, Y., Liu, J., Nipper, M., & Wang, P. (2019). Ductal vs. acinar? Recent insights into identifying cell lineage of pancreatic ductal adenocarcinoma. *Annals of Pancreatic Cancer*, *2*, 11. https://doi.org/10.21037/apc.2019.06.03
Xue, J., Schmidt, S. V, Sander, J., Draffehn, A., Krebs, W., Quester, I., De Nardo, D., Gohel, T. D., Emde, M., Schmidleithner, L., Ganesan, H., Nino-Castro, A., Mallmann, M. R., Labzin, L., Theis, H., Kraut, M., Beyer, M., Latz, E., Freeman, T. C., … Schultze, J. L. (2014). Transcriptome-based network analysis reveals a spectrum model of human macrophage activation. *Immunity*, *40*(2), 274–288. https://doi.org/10.1016/j.immuni.2014.01.006
Yamaki, S., Yanagimoto, H., Tsuta, K., Ryota, H., & Kon, M. (2017). PD-L1 expression in pancreatic ductal adenocarcinoma is a poor prognostic factor in patients with high CD8+ tumor-infiltrating lymphocytes: highly sensitive detection using phosphor-integrated dot staining. *International Journal of Clinical Oncology*, *22*(4), 726–733. https://doi.org/10.1007/s10147-017-1112-3
Yamamoto, T., Yanagimoto, H., Satoi, S., Toyokawa, H., Hirooka, S., Yamaki, S., Yui, R., Yamao, J., Kim, S., & Kwon, A.-H. (2012). Circulating CD4+CD25+ Regulatory T Cells in Patients With Pancreatic Cancer. *Pancreas*, *41*(3). https://journals.lww.com/pancreasjournal/Fulltext/2012/04000/Circulating_CD4_CD25__Regulatory_T_Cells_in.8.aspx
Yan, H. H., Jiang, J., Pang, Y., Achyut, B. R., Lizardo, M., Liang, X., Hunter, K., Khanna, C., Hollander, C., & Yang, L. (2015). CCL9 Induced by TGFβ Signaling in Myeloid Cells Enhances Tumor Cell Survival in the Premetastatic Organ. *Cancer Research*, *75*(24), 5283–5298. https://doi.org/10.1158/0008-5472.CAN-15-2282-T
Yang, M., Liu, F., Higuchi, K., Sawashita, J., Fu, X., Zhang, L., Zhang, L., Fu, L., Tong, Z., & Higuchi, K. (2016). Serum amyloid A expression in the breast cancer tissue is associated with poor prognosis. *Oncotarget*, *7*(24), 35843–35852. https://doi.org/10.18632/oncotarget.8561
Yang, S., Liu, Q., & Liao, Q. (2021). Tumor-Associated Macrophages in Pancreatic Ductal Adenocarcinoma: Origin, Polarization, Function, and Reprogramming. *Frontiers in Cell and Developmental Biology*, *8*, 607209. https://doi.org/10.3389/fcell.2020.607209
Yang, T., Xie, Z., Li, H., Yue, L., Pang, Z., MacNeil, A. J., Tremblay, M. L., Tang, J.-T., & Lin, T.-J. (2016). Protein tyrosine phosphatase 1B (PTP1B) is dispensable for IgE-mediated cutaneous reaction in vivo. *Cellular Immunology*, *306–307*, 9–16. https://doi.org/https://doi.org/10.1016/j.cellimm.2016.05.005
Ying, H., Elpek, K. G., Vinjamoori, A., Zimmerman, S. M., Chu, G. C., Yan, H., Fletcher-Sananikone, E., Zhang, H., Liu, Y., Wang, W., Ren, X., Zheng, H., Kimmelman, A. C., Paik, J., Lim, C., Perry, S. R., Jiang, S., Malinn, B., Protopopov, A., … DePinho, R. A. (2011). PTEN is a major tumor suppressor in pancreatic ductal adenocarcinoma and regulates an NF-κB-cytokine network. *Cancer Discovery*, *1*(2), 158–169. https://doi.org/10.1158/2159-8290.CD-11-0031
Zhan, Y., Lew, A. M., & Chopin, M. (2019). The Pleiotropic Effects of the GM-CSF Rheostat on Myeloid Cell Differentiation and Function: More Than a Numbers Game . In *Frontiers in*

Immunology (Vol. 10). https://www.frontiersin.org/article/10.3389/fimmu.2019.02679
Zhang, A. M. Y., Magrill, J., de Winter, T. J. J., Hu, X., Skovsø, S., Schaeffer, D. F., Kopp, J. L., & Johnson, J. D. (2019). Endogenous Hyperinsulinemia Contributes to Pancreatic Cancer Development. *Cell Metabolism*, *30*(3), 403–404. https://doi.org/10.1016/j.cmet.2019.07.003
Zhang, A., Qian, Y., Ye, Z., Chen, H., Xie, H., Zhou, L., Shen, Y., & Zheng, S. (2017). Cancer-associated fibroblasts promote M2 polarization of macrophages in pancreatic ductal adenocarcinoma. *Cancer Medicine*, *6*(2), 463–470. https://doi.org/10.1002/cam4.993
Zhang, Yaqing, Lazarus, J., Steele, N. G., Yan, W., Lee, H.-J., Nwosu, Z. C., Halbrook, C. J., Menjivar, R. E., Kemp, S. B., Sirihorachai, V. R., Velez-Delgado, A., Donahue, K., Carpenter, E. S., Brown, K. L., Irizarry-Negron, V., Nevison, A. C., Vinta, A., Anderson, M. A., Crawford, H. C., … Pasca di Magliano, M. (2020). Regulatory T-cell Depletion Alters the Tumor Microenvironment and Accelerates Pancreatic Carcinogenesis. *Cancer Discovery*, *10*(3), 422 LP – 439. https://doi.org/10.1158/2159-8290.CD-19-0958
Zhang, Yaqing, Velez-Delgado, A., Mathew, E., Li, D., Mendez, F. M., Flannagan, K., Rhim, A. D., Simeone, D. M., Beatty, G. L., & Pasca di Magliano, M. (2017). Myeloid cells are required for PD-1/PD-L1 checkpoint activation and the establishment of an immunosuppressive environment in pancreatic cancer. *Gut*, *66*(1), 124–136. https://doi.org/10.1136/gutjnl-2016-312078
Zhang, Yue, Chen, X., Mo, S., Ma, H., Lu, Z., Yu, S., & Chen, J. (2022). PD-L1 and PD-L2 expression in pancreatic ductal adenocarcinoma and their correlation with immune infiltrates and DNA damage response molecules. *The Journal of Pathology: Clinical Research*, *8*(3), 257–267. https://doi.org/https://doi.org/10.1002/cjp2.259
Zhang, Z., Zheng, M., Ding, Q., & Liu, M. (2022). CD93 Correlates With Immune Infiltration and Impacts Patient Immunotherapy Efficacy: A Pan-Cancer Analysis . In *Frontiers in Cell and Developmental Biology* (Vol. 10). https://www.frontiersin.org/article/10.3389/fcell.2022.817965
Zhu, Y., Herndon, J. M., Sojka, D. K., Kim, K.-W., Knolhoff, B. L., Zuo, C., Cullinan, D. R., Luo, J., Bearden, A. R., Lavine, K. J., Yokoyama, W. M., Hawkins, W. G., Fields, R. C., Randolph, G. J., & DeNardo, D. G. (2017). Tissue-Resident Macrophages in Pancreatic Ductal Adenocarcinoma Originate from Embryonic Hematopoiesis and Promote Tumor Progression. *Immunity*, *47*(2), 323-338.e6. https://doi.org/10.1016/j.immuni.2017.07.014
Zhu, Y., Knolhoff, B. L., Meyer, M. A., Nywening, T. M., West, B. L., Luo, J., Wang-Gillam, A., Goedegebuure, S. P., Linehan, D. C., & DeNardo, D. G. (2014). CSF1/CSF1R blockade reprograms tumor-infiltrating macrophages and improves response to T-cell checkpoint immunotherapy in pancreatic cancer models. *Cancer Research*, *74*(18), 5057–5069. https://doi.org/10.1158/0008-5472.CAN-13-3723
Zhu, Z., Zhang, H., Zhang, X., He, S., Dong, W., Wang, X., Chen, Y., Liu, X., & Guo, C. (2020). Lipopolysaccharide Downregulates CD163 Expression to Inhibit PRRSV Infection via TLR4-NF-κB Pathway . In *Frontiers in Microbiology* (Vol. 11). https://www.frontiersin.org/article/10.3389/fmicb.2020.00501
Zhuang, Y., Zhao, X., Yuan, B., Zeng, Z., & Chen, Y. (2021). Blocking the CCL5-CCR5 Axis Using Maraviroc Promotes M1 Polarization of Macrophages Cocultured with Irradiated Hepatoma Cells. *Journal of Hepatocellular Carcinoma*, *8*, 599–611. https://doi.org/10.2147/JHC.S300165

Appendices

Appendix A BMDM RNA-seq

A.1 *KPten*$^{\Delta Acinar}$ BMDM differentially expressed genes

The table below lists differentially expressed genes of *KPten*$^{\Delta Acinar}$ BMDMs compared to M0 and NC BMDM controls. Genes are ranked by significance. Genes that are highlighted are shared with *KPten*$^{\Delta Duct}$ BMDMs

gene_id	gene_name	log2FoldChange	log2CPM	baseMean
ENSMUSG00000052336	Cx3cr1	-2.87	6.07	1797.38
ENSMUSG00000026580	Selp	5.3	4.09	453.64
ENSMUSG00000029082	Bst1	3.02	5.95	1670.09
ENSMUSG00000037095	Lrg1	6.18	2.97	211.37
ENSMUSG00000015766	Eps8	2.48	6.45	2359.23
ENSMUSG00000029413	Naaa	1.79	5.74	1446.93
ENSMUSG00000020027	Socs2	2.14	3.52	308.86
ENSMUSG00000029553	Tfec	1.51	5.72	1428.86
ENSMUSG00000003541	Ier3	1.41	5.47	1197.34
ENSMUSG00000039899	Fgl2	1.3	5.55	1271.07
ENSMUSG00000018927	Ccl6	2.59	9.86	25272.79
ENSMUSG00000026365	Cfh	1.4	7.8	6007.84
ENSMUSG00000027848	Olfml3	-3.96	1.67	82.98
ENSMUSG00000026656	Fcgr2b	1.59	7.66	5504.21
ENSMUSG00000008318	Relt	1.34	4.5	610.33
ENSMUSG00000071068	Treml2	1.87	3.42	288.38
ENSMUSG00000040253	Gbp7	1.52	5.84	1562.04
ENSMUSG00000026605	Cenpf	-1.86	4.71	702.83
ENSMUSG00000020641	Rsad2	-1.61	4.58	641.24
ENSMUSG00000092021	Gbp11	6.19	0.83	46.37
ENSMUSG00000031444	F10	2.96	3.41	287.35
ENSMUSG00000025804	Ccr1	2.33	6.48	2423.92
ENSMUSG00000045932	Ifit2	-1.84	4.93	821.87
ENSMUSG00000025429	Pstpip2	1.58	4.94	829.98
ENSMUSG00000032724	Abtb2	2.18	3.26	256.67
ENSMUSG00000021990	Spata13	-1.98	3.27	257.44
ENSMUSG00000037224	Zfyve28	-1.43	4.5	604.7
ENSMUSG00000053113	Socs3	2.24	6.14	1906.54
ENSMUSG00000030748	Il4ra	1.56	9.14	15292.03
ENSMUSG00000039753	Fbxl5	1.43	6.41	2272.15

ENSMUSG00000026558	Uck2	0.96	6.1	1846.63
ENSMUSG00000003032	Klf4	1.3	5.49	1213.3
ENSMUSG00000041773	Enc1	-1.23	6.25	2047.86
ENSMUSG00000051339	2900026A02Rik	-1.54	4.17	481.05
ENSMUSG00000048264	Dip2c	1.55	4.28	523.03
ENSMUSG00000047222	Rnase2a	6.58	0.3	31.36
ENSMUSG00000074896	Ifit3	-2.38	4	429.96
ENSMUSG00000107260	NA	8.57	1.88	94.03
ENSMUSG00000036362	P2ry13	1.83	3.15	238.69
ENSMUSG00000071713	Csf2rb	1.05	9.24	16402.21
ENSMUSG00000015852	Fcrls	-1.52	7.15	3841.5
ENSMUSG00000040229	Gpr34	-1.95	2.84	191.23
ENSMUSG00000050075	Gpr171	1.99	2.7	174.04
ENSMUSG00000019256	Ahr	1.28	3.95	415.75
ENSMUSG00000073902	Gm1966	1.79	4.27	525.98
ENSMUSG00000002602	Axl	-1.99	4.38	559.35
ENSMUSG00000045092	S1pr1	-1.17	6.2	1976.98
ENSMUSG00000056498	Tmem154	1.44	7.6	5256.57
ENSMUSG00000024053	Emilin2	1.25	9.15	15360.05
ENSMUSG00000031613	Hpgd	-1	5.2	986.85
ENSMUSG00000055541	Lair1	-1.29	5.99	1683.09
ENSMUSG00000052512	Nav2	-1.16	4.49	596.83
ENSMUSG00000037447	Arid5a	1.31	5.71	1393.11
ENSMUSG00000050212	Eva1b	0.99	5.05	893.82
ENSMUSG00000033952	Aspm	-1.54	4.3	524.15
ENSMUSG00000032218	Ccnb2	-1.82	4.95	830.23
ENSMUSG00000023008	Fmnl3	-1.12	5.86	1565.64
ENSMUSG00000015396	Cd83	-1.36	5.12	934.94
ENSMUSG00000045312	Lhfpl2	-1.01	7.37	4460.68
ENSMUSG00000025324	Atp10a	1.44	3.31	267.17
ENSMUSG00000046223	Plaur	0.94	5.44	1175.32
ENSMUSG00000056758	Hmga2	-0.85	6.53	2489.87
ENSMUSG00000003882	Il7r	-1.44	6.02	1747.58
ENSMUSG00000057337	Chst3	-1.62	3.07	221.92
ENSMUSG00000022218	Tgm1	1.94	1.95	103.3
ENSMUSG00000023349	Clec4n	1.19	6.83	3024.25
ENSMUSG00000045328	Cenpe	-1.58	4.99	853.92
ENSMUSG00000047250	Ptgs1	0.97	6.31	2140.44
ENSMUSG00000032661	Oas3	-1.07	6.42	2304.83

ENSMUSG00000030786	Itgam	1.09	10.29	27694.8
ENSMUSG00000045917	Tmem268	1.44	6.05	1791.72
ENSMUSG00000059089	Fcgr4	1.29	6.51	2474.42
ENSMUSG00000018920	Cxcl16	-1.45	6.71	2774.89
ENSMUSG00000035683	Melk	-2.17	3.15	237.08
ENSMUSG00000032076	Cadm1	-1.03	6.4	2226.87
ENSMUSG00000022494	Shisa9	-2.34	1.99	104.97
ENSMUSG00000000318	Clec10a	1.54	5.52	1221.66
ENSMUSG00000003779	Kif20a	-1.67	5.22	1004.09
ENSMUSG00000028716	Pdzk1ip1	-1.99	3.11	229.49
ENSMUSG00000020638	Cmpk2	-1.39	3.89	398.43
ENSMUSG00000054342	Kcnn4	-2.22	5.89	1571.6
ENSMUSG00000026785	Pkn3	-1.64	2.69	170.93
ENSMUSG00000021250	Fos	-1.26	6.31	2134.96
ENSMUSG00000034656	Cacna1a	-1.33	5.11	925.83
ENSMUSG00000049866	Arl4c	-0.78	7.72	5695.25
ENSMUSG00000030717	Nupr1	1.16	3.52	304.07
ENSMUSG00000031274	Col4a5	-2.23	3.08	225.98
ENSMUSG00000034459	Ifit1	-1.76	3.49	300.56
ENSMUSG00000021338	Carmil1	-1.76	2.13	115.92
ENSMUSG00000024451	Arap3	-1.53	5.97	1694.1
ENSMUSG00000006205	Htra1	1.97	1.77	90.54
ENSMUSG00000040855	Reps2	-0.88	5.3	1058.79
ENSMUSG00000035673	Sbno2	0.89	8.15	7689.21
ENSMUSG00000034858	Fam214a	-0.88	5.03	878.76
ENSMUSG00000019122	Ccl9	0.99	9.69	22347.92
ENSMUSG00000022508	Bcl6	-0.79	5.81	1516.1
ENSMUSG00000089665	Fcor	2.39	2.48	155.97
ENSMUSG00000027715	Ccna2	-1.84	5.16	966.44
ENSMUSG00000058290	Espl1	-1.63	3.85	387.91
ENSMUSG00000038390	Gpr162	-2.64	4.54	613.42
ENSMUSG00000012443	Kif11	-1.75	4.68	692.13
ENSMUSG00000041498	Kif14	-2.05	2.4	139.66
ENSMUSG00000018334	Ksr1	1.11	4.44	584.63
ENSMUSG00000047592	Nxpe5	1	6.82	3060.55
ENSMUSG00000047798	Cd300lf	1.2	7.27	4144.11
ENSMUSG00000058818	Pirb	0.97	9.88	25153.7
ENSMUSG00000042842	Serpinb6b	-2.94	2.82	188.18
ENSMUSG00000027331	Knstrn	-1.47	4.46	536.21

ENSMUSG00000021624	Cd180	-1.86	6.78	2952.96
ENSMUSG00000061132	Blnk	-1.44	6.21	2001.45
ENSMUSG00000028068	Iqgap3	-1.98	4.33	540.38
ENSMUSG00000030737	Slco2b1	-1.24	3.69	345.18
ENSMUSG00000032578	Cish	1.5	3.04	199.7
ENSMUSG00000024989	Cep55	-1.62	3.67	341.46
ENSMUSG00000004105	Angptl2	-1.68	5.95	1586.97
ENSMUSG00000021069	Pygl	0.95	8.3	8488.47
ENSMUSG00000021665	Hexb	-0.83	8.16	7724.23
ENSMUSG00000025582	Nptx1	-3.2	2.93	204.2
ENSMUSG00000000386	Mx1	-2.06	2.85	201.71
ENSMUSG00000002233	Rhoc	-1.4	4.91	793.52
ENSMUSG00000033355	Rtp4	-1.15	5.28	1044.16
ENSMUSG00000096054	Syne1	-1.24	4.69	694.62
ENSMUSG00000021728	Emb	1.2	9.27	16754.02
ENSMUSG00000004562	Arhgef40	-1.75	2.44	143.18
ENSMUSG00000022021	Diaph3	-1.92	3.76	362.96
ENSMUSG00000027469	Tpx2	-1.46	5.09	913.01
ENSMUSG00000040829	Zmynd15	-1.52	2.61	160.72
ENSMUSG00000004609	Cd33	1.86	6.5	2584.6
ENSMUSG00000022469	Rapgef3	-2.11	1.41	68.97
ENSMUSG00000029304	Spp1	-1.19	10.37	35734.75
ENSMUSG00000026628	Atf3	-1.16	7.54	5030.37
ENSMUSG00000042476	Abcb4	-1.12	5.1	923.95
ENSMUSG00000053101	Gpr141	1.17	4.9	808.13
ENSMUSG00000019987	Arg1	4.77	-0.81	13.87
ENSMUSG00000102051	I830127L07Rik	3.71	-0.23	21.61
ENSMUSG00000009654	Oit3	-1.75	2.82	187.65
ENSMUSG00000017754	Pltp	-0.99	8.76	11612.84
ENSMUSG00000026955	Sapcd2	-2.77	1.25	60.9
ENSMUSG00000099398	Ms4a14	-1	4.83	767.41
ENSMUSG00000028459	Cd72	-2.7	6.31	2109.59
ENSMUSG00000030867	Plk1	-1.72	4.43	580.31
ENSMUSG00000059824	Dbp	-1.07	5.59	1292.16
ENSMUSG00000026683	Nuf2	-1.67	4.03	437.75
ENSMUSG00000070407	Hs3st3b1	3.01	1.31	64.91
ENSMUSG00000072620	Slfn2	0.87	8.83	12305.04
ENSMUSG00000019818	Cd164	1.09	7.63	5352.94
ENSMUSG00000020689	Itgb3	-2.25	3.77	366.98

ENSMUSG00000022305	Lrp12	0.7	7.39	4533.37
ENSMUSG00000029516	Cit	-1.63	3.27	254.93
ENSMUSG00000051212	Gpr183	-2.07	3.44	291.33
ENSMUSG00000033066	Gas7	0.73	8.18	7846.09
ENSMUSG00000020658	Efr3b	-2.39	2.41	140.71
ENSMUSG00000000489	Pdgfb	-2.26	4.9	824.7
ENSMUSG00000038379	Ttk	-1.85	2.54	154.37
ENSMUSG00000036086	Zranb3	-2.11	4.38	561.39
ENSMUSG00000031584	Gsr	1.2	7.31	4296.89
ENSMUSG00000008305	Tle1	-1.36	3.89	392.62
ENSMUSG00000006398	Cdc20	-1.5	4.64	670.15
ENSMUSG00000032254	Kif23	-1.7	5.02	875.72
ENSMUSG00000020914	Top2a	-1.61	6.51	2469.78
ENSMUSG00000020493	Prr11	-1.59	3.79	371.93
ENSMUSG00000022322	Shcbp1	-1.94	2.68	171.12
ENSMUSG00000001517	Foxm1	-1.61	4.08	449.85
ENSMUSG00000029333	Rasgef1b	-1.31	5.66	1367.7
ENSMUSG00000089929	Bcl2a1b	0.79	6.5	3203.21
ENSMUSG00000071637	Cebpd	1.07	5.89	1614.61
ENSMUSG00000059108	Ifitm6	1.51	3.65	341.67
ENSMUSG00000037725	Ckap2	-1.68	3.35	272.87
ENSMUSG00000051378	Kif18b	-1.87	3.09	227.48
ENSMUSG00000072082	Ccnf	-1.78	4.28	524.34
ENSMUSG00000032035	Ets1	-2.81	1.8	91.48
ENSMUSG00000041642	Kif21b	-0.86	5.66	1359.9
ENSMUSG00000004347	Pde1c	-3.51	1.4	68.73
ENSMUSG00000023015	Racgap1	-1.73	5.1	919.54
ENSMUSG00000029414	Kntc1	-2.29	3.15	235.94
ENSMUSG00000062488	Ifit3b	-2.88	1.65	93.62
ENSMUSG00000028339	Col15a1	-1.48	1.84	94.14
ENSMUSG00000027035	Cers6	1.11	7.08	3642.02
ENSMUSG00000029490	Mfsd7a	0.96	3.89	399.83
ENSMUSG00000053063	Clec12a	-1.61	7.81	6067.35
ENSMUSG00000056749	Nfil3	1.44	6.12	1884.08
ENSMUSG00000026581	Sell	4.19	5.3	1065.96
ENSMUSG00000014786	Slc9a5	-1.34	3.53	309.04
ENSMUSG00000048537	Phldb1	-1.11	3.96	416.88
ENSMUSG00000005583	Mef2c	-1.03	5.61	1323.01
ENSMUSG00000046186	Cd109	-1.65	3.25	254.89

ENSMUSG00000072437	Nanos1	-2.91	2.61	163.14
ENSMUSG00000035835	Plppr3	1.88	2.58	160.35
ENSMUSG00000074305	Peak1	-0.79	6.02	1746.21
ENSMUSG00000024242	Map4k3	-0.84	5.51	1225.3
ENSMUSG00000040852	Plekhh2	-2.47	1.64	81.44
ENSMUSG00000020897	Aurkb	-1.29	4.1	453.06
ENSMUSG00000034023	Fancd2	-1.82	2.48	147.93
ENSMUSG00000022122	Ednrb	1.72	5.51	1240.03
ENSMUSG00000040774	Cept1	0.8	7.04	3537.03
ENSMUSG00000028678	Kif2c	-1.7	4	425.96
ENSMUSG00000040084	Bub1b	-1.73	4.78	740.46
ENSMUSG00000026012	Cd28	-1.04	6.44	2347.34
ENSMUSG00000071042	Rasgrp3	-1.32	5.21	997.4
ENSMUSG00000009418	Nav1	-0.82	6.57	2515.48
ENSMUSG00000029561	Oasl2	-1.07	6.02	1579.2
ENSMUSG00000028312	Smc2	-1.38	5.18	980.78
ENSMUSG00000044468	Fam46c	-1.08	3.85	387.75
ENSMUSG00000038252	Ncapd2	-1.3	5.55	1255.26
ENSMUSG00000024421	Lama3	-1.69	2.54	154.79
ENSMUSG00000033207	Mamdc2	-2.49	2.44	144.63
ENSMUSG00000027379	Bub1	-1.38	4.03	438.38
ENSMUSG00000024672	Ms4a7	-1.12	8.24	8103.37
ENSMUSG00000024795	Kif20b	-1.24	4.53	622.28
ENSMUSG00000029207	Apbb2	-1.15	4.65	668.87
ENSMUSG00000020808	Fam64a	-2.04	3.76	364.54
ENSMUSG00000003617	Cp	1.77	1.07	54.47
ENSMUSG00000037849	Ifi206	-1.92	1.2	59.74
ENSMUSG00000045362	Tnfrsf26	0.86	5.13	942.82
ENSMUSG00000029108	Pcdh7	-1.34	5.6	1188.35
ENSMUSG00000049103	Ccr2	0.8	5.96	1654.61
ENSMUSG00000074519	Zfp971	1.15	3.43	290.41
ENSMUSG00000036452	Arhgap26	0.89	3.81	341.92
ENSMUSG00000031004	Mki67	-0.72	7.09	3673.6
ENSMUSG00000058624	Gda	2.9	8.75	11681.85
ENSMUSG00000062510	Nsl1	-1.82	2.72	175.75
ENSMUSG00000032350	Gclc	0.66	6.29	2120.07
ENSMUSG00000043336	Filip1l	1.27	5.74	1440.38
ENSMUSG00000054676	1600014C10Rik	1.46	6.71	2834.68
ENSMUSG00000030649	Anapc15	-0.79	5.48	1180.98

ENSMUSG00000035914	Cd276	-2.61	1.64	82.05
ENSMUSG00000025491	Ifitm1	1.37	3.58	322.21
ENSMUSG00000024052	Lpin2	-0.65	6.28	2052.25
ENSMUSG00000024590	Lmnb1	-1.82	4.47	598.72
ENSMUSG00000046295	Ankle1	-2.37	1.79	89.73
ENSMUSG00000054843	Atrnl1	1.58	6.68	2785.84
ENSMUSG00000026548	Slamf9	-3.13	2.58	159.56
ENSMUSG00000002227	Mov10	-1.23	4.37	553.98
ENSMUSG00000026207	Speg	-1.1	6.36	2210.55
ENSMUSG00000026822	Lcn2	3.02	2.47	146.65
ENSMUSG00000032221	Mns1	-2.12	1.62	79.93
ENSMUSG00000032741	Tpcn1	-0.72	7.71	5632.2
ENSMUSG00000026579	F5	2.04	3.61	329.43
ENSMUSG00000042724	Map3k9	-1.16	3.95	415.14
ENSMUSG00000024534	Sncaip	-3.39	1.01	51.67
ENSMUSG00000028927	Padi2	-1.35	5	864.8
ENSMUSG00000032666	1700025G04Rik	-1.24	4.43	580.68
ENSMUSG00000066800	Rnasel	0.7	7.86	5713.5
ENSMUSG00000032911	Cspg4	-4.06	-0.15	21.97
ENSMUSG00000001403	Ube2c	-1.52	4.46	591.17
ENSMUSG00000036478	Btg1	0.68	8.31	8542.23
ENSMUSG00000060591	Ifitm2	0.68	8.71	11372.75
ENSMUSG00000026358	Rgs1	-1.11	5.43	1049.12
ENSMUSG00000040751	Lat2	-1.42	6.98	3343.01
ENSMUSG00000002055	Spag5	-1.58	3.96	416.62
ENSMUSG00000023034	Nr4a1	-1.19	3.79	371.89
ENSMUSG00000024730	Ms4a8a	3.63	1.72	79.58
ENSMUSG00000034206	Polq	-1.67	1.77	88.96
ENSMUSG00000057729	Prtn3	2.32	0.38	33.31
ENSMUSG00000078763	Slfn1	2.28	0.07	26.56
ENSMUSG00000038943	Prc1	-1.68	5.08	898
ENSMUSG00000079339	Ifit1bl1	-3.2	1.12	56.25
ENSMUSG00000021485	Mxd3	-2.44	0.94	49.42
ENSMUSG00000023505	Cdca3	-1.71	4.47	590.71
ENSMUSG00000028657	Ppt1	0.75	8.17	7779.92
ENSMUSG00000026622	Nek2	-1.54	4.15	473.8
ENSMUSG00000023262	Acy1	1.14	3.12	232.38
ENSMUSG00000026023	Cdk15	-2.72	0.97	51.04
ENSMUSG00000023473	Celsr3	1.09	3.29	272.36

ENSMUSG00000026437	Cdk18	-1.37	6.95	3329.74
ENSMUSG00000022995	Enah	2.06	0.82	46.06
ENSMUSG00000040957	Cables1	1.32	3.02	217.28
ENSMUSG00000039187	Fanci	-1.8	2.4	139.52
ENSMUSG00000029534	St7	1.1	3.56	315.76
ENSMUSG00000031971	Ccsap	-1.54	2.72	175.02
ENSMUSG00000002204	Napsa	0.89	6.77	2931.56
ENSMUSG00000039994	Timeless	-1.65	2.98	208.9
ENSMUSG00000007613	Tgfbr1	-0.66	7.18	3878.32
ENSMUSG00000044197	Gpr146	0.99	7.12	3612.29
ENSMUSG00000105504	Gbp5	0.9	3.66	339.82
ENSMUSG00000020053	Igf1	-1.17	8.31	8577.89
ENSMUSG00000034311	Kif4	-1.84	3.56	318.77
ENSMUSG00000048327	Ckap2l	-1.55	3.79	370.99
ENSMUSG00000027326	Knl1	-1.53	3.06	220.63
ENSMUSG00000028037	Ifi44	-2.37	0.41	33.38
ENSMUSG00000027078	Ube2l6	-1.4	5.21	905.08
ENSMUSG00000022372	Sla	1.6	7.18	3868.84
ENSMUSG00000074886	Grk6	0.68	6.17	1950.44
ENSMUSG00000013698	Pea15a	-1.26	7.64	5328.51
ENSMUSG00000029177	Cenpa	-1.3	5.76	1436.88
ENSMUSG00000027306	Nusap1	-1.58	4.16	478.58
ENSMUSG00000052688	Rab7b	-1.15	7.2	3607.99
ENSMUSG00000024640	Psat1	-1.22	3.71	318.69
ENSMUSG00000036181	Hist1h1c	-0.59	6.87	3146.47
ENSMUSG00000030530	Furin	0.67	7.97	6758.74
ENSMUSG00000044201	Cdc25c	-2.22	1.85	94.92
ENSMUSG00000056394	Lig1	-1.84	4.76	727.43
ENSMUSG00000047415	Gpr68	-1.99	1.54	76.07
ENSMUSG00000034906	Ncaph	-1.36	4.34	543.85
ENSMUSG00000020330	Hmmr	-1.36	4.61	657.63
ENSMUSG00000031825	Crispld2	2.71	-0.09	24.46
ENSMUSG00000058794	Nfe2	1.61	1.87	87.74
ENSMUSG00000029153	Ociad2	-1.66	1.52	75.21
ENSMUSG00000060550	H2-Q7	-1.23	3.48	290.63
ENSMUSG00000061589	Dot1l	-0.67	5.75	1438.47
ENSMUSG00000060703	Cd302	0.58	5.99	1716.53
ENSMUSG00000020023	Tmcc3	-1.09	4.05	444.2
ENSMUSG00000022415	Syngr1	-1.12	6.2	1976.44

ENSMUSG00000025355	Mmp19	1.33	6.56	2554.28
ENSMUSG00000036777	Anln	-1.5	4.89	800.33
ENSMUSG00000024056	Ndc80	-1.91	3.77	365.95
ENSMUSG00000024397	Aif1	-1.3	3.79	370.75
ENSMUSG00000019823	Mical1	-0.89	5.69	1381.42
ENSMUSG00000019961	Tmpo	-0.99	6.22	2008.26
ENSMUSG00000031391	L1cam	-1.54	4.49	597.16
ENSMUSG00000035439	Haus8	-0.77	6.08	1653.08
ENSMUSG00000040026	Saa3	4.82	6.88	3233.5
ENSMUSG00000017716	Birc5	-1.89	4.5	609.4
ENSMUSG00000063506	Arhgap22	-0.57	7.08	3633.18
ENSMUSG00000078452	Raet1d	-1.59	2.28	133.18
ENSMUSG00000042607	Asb4	1.18	2.39	140.27
ENSMUSG00000030148	Clec4a2	0.63	5.69	1337.56
ENSMUSG00000033031	C330027C09Rik	-1.24	4.14	474.02
ENSMUSG00000025268	Maged2	-1.47	3.47	292.89
ENSMUSG00000032232	Cgnl1	-0.91	5.56	1268.75
ENSMUSG00000016756	Cmah	-2.08	2.64	188.92
ENSMUSG00000017417	Plxdc1	-0.69	5.14	948.73
ENSMUSG00000074874	Ctla2b	-0.58	6.21	1996.86
ENSMUSG00000001435	Col18a1	-0.8	5.49	1208.37
ENSMUSG00000068923	Syt11	-0.66	5.88	1565.85
ENSMUSG00000069607	Cd300ld3	-1.58	5.77	2180.25
ENSMUSG00000021720	Rnf180	-1.04	3.42	286.79
ENSMUSG00000042644	Itpr3	-0.59	5.97	1693.4
ENSMUSG00000034641	Cd300ld	-1	6.81	3024.51
ENSMUSG00000027068	Dhrs9	-1.75	3.41	284.9
ENSMUSG00000024180	Tmem8	0.6	7.28	4269.25
ENSMUSG00000041431	Ccnb1	-1.29	4.63	663.31
ENSMUSG00000025574	Tk1	-2.28	3.94	445.19
ENSMUSG00000059714	Flot1	0.57	6.72	2795.26
ENSMUSG00000048498	Cd300e	-2.78	0.35	32.16
ENSMUSG00000040715	Rsc1a1	5	1.67	776.79
ENSMUSG00000019852	Arfgef3	-0.9	3.21	248.21
ENSMUSG00000051220	Ercc6l	-1.68	2.81	186.98
ENSMUSG00000043909	Trp53bp1	-0.67	4.87	710.65
ENSMUSG00000034908	Sidt2	0.94	8.35	8733.32
ENSMUSG00000021697	Depdc1b	-1.61	1.54	76.29
ENSMUSG00000004891	Nes	-4.13	4.2	493.3

ENSMUSG00000027540	Ptpn1	0.66	8.85	12491.84
ENSMUSG00000027087	Itgav	-0.57	6.42	2081.28
ENSMUSG00000028661	Epha8	-2.78	0.98	51.48
ENSMUSG00000037697	Ddhd1	1.64	5.55	1248.54
ENSMUSG00000021360	Gcnt2	2.6	3.58	347.76
ENSMUSG00000041064	Pif1	-1.84	2.59	158.91
ENSMUSG00000036381	P2ry14	0.86	4.18	443.5
ENSMUSG00000035246	Pcyt1b	-2.81	1.46	71.59
ENSMUSG00000048922	Cdca2	-1.52	3.47	294.17
ENSMUSG00000001542	Ell2	-0.82	5.52	1240.03
ENSMUSG00000027699	Ect2	-1.28	3.82	379.79
ENSMUSG00000044006	Cilp2	-1.06	3.22	248.38
ENSMUSG00000042659	Arrdc4	0.79	6.31	2141.49
ENSMUSG00000020077	Srgn	0.79	7.43	4225.93
ENSMUSG00000039629	Strip2	2.4	0.64	40.49
ENSMUSG00000037544	Dlgap5	-1.58	4.08	451.04
ENSMUSG00000030342	Cd9	-1.73	7.49	6764.51
ENSMUSG00000020435	Osbp2	-1.46	2.48	148.14
ENSMUSG00000032220	Myo1e	-1.62	6.78	3051.17
ENSMUSG00000059013	Sh2d3c	-0.97	4.78	741.77
ENSMUSG00000026463	Atp2b4	-1.2	2.55	155.01
ENSMUSG00000049871	Nlrc3	-1.01	3.32	267.59
ENSMUSG00000060470	Adgrg3	-2.26	-0.07	31.1
ENSMUSG00000038244	Mical2	-0.73	4.01	431.11
ENSMUSG00000051517	Arhgef39	-1.34	2.72	173.91
ENSMUSG00000038811	Gngt2	-0.7	5.47	1188.12
ENSMUSG00000027323	Rad51	-2.06	2.87	193.85
ENSMUSG00000028207	Asph	-1.09	6.82	3058.02
ENSMUSG00000102440	Pcdhga9	-6.92	-1.56	19.08
ENSMUSG00000039115	Itga9	-1.27	2.61	161.94
ENSMUSG00000030946	Lhpp	-0.84	4.43	521.79
ENSMUSG00000035342	Lzts2	-0.92	4.16	479.07
ENSMUSG00000021125	Arg2	1.9	2.98	212.12
ENSMUSG00000034917	Tjp3	-0.87	3.45	308.82
ENSMUSG00000039774	Galnt12	-1.4	4.1	461.61
ENSMUSG00000030793	Pycard	0.57	6.38	2302.57
ENSMUSG00000002957	Ap2a2	0.69	8.38	9135.65
ENSMUSG00000078783	Gm9733	1.96	0.22	35.31
ENSMUSG00000005410	Mcm5	-2.06	4.92	1176.75

ENSMUSG00000030107	Usp18	-0.79	3.78	368.86
ENSMUSG00000029254	Stap1	-1.47	5.25	1017.39
ENSMUSG00000044783	Hjurp	-0.84	5.62	1312.38
ENSMUSG00000053835	H2-T24	-0.99	3.68	343.72
ENSMUSG00000001930	Vwf	-1.01	7.62	5284.86
ENSMUSG00000046432	Bex3	-0.71	4.92	739.73
ENSMUSG00000040699	Limd2	-0.55	7.19	3555.31
ENSMUSG00000032589	Bsn	-0.88	4.08	453.76
ENSMUSG00000037466	4930427A07Rik	-1.5	2.47	147.03
ENSMUSG00000040204	Pclaf	-2.37	3.84	462.45
ENSMUSG00000015749	Anp32e	-0.97	5.83	1387.86
ENSMUSG00000000693	Loxl3	-1.08	2.37	139.25
ENSMUSG00000025498	Irf7	-0.98	5	788.11
ENSMUSG00000047180	Neurl3	-0.69	8	6923.47
ENSMUSG00000028832	Stmn1	-1.57	6.5	2272.23
ENSMUSG00000059498	Fcgr3	0.96	10.11	27122.73
ENSMUSG00000038894	Irs2	0.73	4.66	723.9
ENSMUSG00000008496	Pou2f2	-0.59	6.04	1767.03
ENSMUSG00000026764	Kif5c	-1.37	2.48	148.32
ENSMUSG00000045934	Mtmr11	-1.24	2.81	184.24
ENSMUSG00000034285	Nipsnap1	-0.88	3.15	236.93
ENSMUSG00000032038	St3gal4	0.58	5.07	921.64
ENSMUSG00000017493	Igfbp4	-0.64	8.25	8176.89
ENSMUSG00000061878	Sphk1	1.69	2.3	118.31
ENSMUSG00000036526	Card11	-4.03	2.36	157.28
ENSMUSG00000042348	Arl15	1.16	4.36	563.79
ENSMUSG00000031337	Mtm1	0.61	5.26	1036.97
ENSMUSG00000036469	March1	0.65	6.3	1998.55
ENSMUSG00000026779	Mastl	-1.73	2.75	179.71
ENSMUSG00000027496	Aurka	-1.18	4.1	460.58
ENSMUSG00000024665	Fads2	-1.86	1.54	76.36
ENSMUSG00000043832	Clec4a3	0.72	6.17	1938.65
ENSMUSG00000000562	Adora3	1.59	1.7	91.33
ENSMUSG00000028702	Rad54l	-1.53	3.24	252.01
ENSMUSG00000034640	Tiparp	0.62	5.01	880.17
ENSMUSG00000000058	Cav2	-0.68	5.7	1396.77
ENSMUSG00000053469	Tg	3.29	-0.48	20.91
ENSMUSG00000016496	Cd274	0.62	5.13	976.4
ENSMUSG00000030208	Emp1	-1.29	7.06	2881

ENSMUSG00000069793	Slfn9	-0.9	4.35	545.53
ENSMUSG00000044674	Fzd1	0.94	3.24	253.42
ENSMUSG00000038151	Prdm1	-0.81	4.3	529.53
ENSMUSG00000037242	Clic4	-1.37	7.72	5774.62
ENSMUSG00000045273	Cenph	-1.89	1.41	69.6
ENSMUSG00000028873	Cdca8	-1.22	4.62	659.64
ENSMUSG00000022353	Mtss1	-0.94	6.24	2033.83
ENSMUSG00000035314	Gdpd5	-0.61	4.9	821.42
ENSMUSG00000043895	S1pr2	-0.8	6.5	2447.04
ENSMUSG00000022505	Emp2	-1.55	4.05	450.97
ENSMUSG00000020661	Dnmt3a	-0.87	7.28	3802.35
ENSMUSG00000026817	Ak1	-1.21	3.16	236.48
ENSMUSG00000037992	Rara	0.86	5.28	1061.85
ENSMUSG00000019966	Kitl	-1.61	4.03	444.26
ENSMUSG00000030122	Ptms	-0.97	8.4	8128.89
ENSMUSG00000035455	Fignl1	-1.99	2.85	193.02
ENSMUSG00000035448	Ccr3	-3.13	1.26	62.45
ENSMUSG00000039005	Tlr4	0.8	7.06	3271.88
ENSMUSG00000027952	Pmvk	0.71	3.88	401.92
ENSMUSG00000041488	Stx3	0.56	6.08	1843.85
ENSMUSG00000078921	Tgtp2	-1.4	1.61	98.53
ENSMUSG00000024750	Zfand5	0.53	7.35	4273.51
ENSMUSG00000026104	Stat1	-0.56	6.84	3216.16
ENSMUSG00000079553	Kifc1	-1.55	4.52	612.98
ENSMUSG00000042489	Clspn	-1.59	3.58	321.42
ENSMUSG00000015468	Notch4	-1.46	1.78	88.8
ENSMUSG00000018449	Rpain	0.7	5.12	851.62
ENSMUSG00000032754	Slc8b1	0.72	7.26	5355.97
ENSMUSG00000026728	Vim	-1.03	9.8	24903.76
ENSMUSG00000078566	Bnip3	0.65	5.73	1410.17
ENSMUSG00000044340	Phlpp1	-0.87	4.6	653.71
ENSMUSG00000021176	Efcab11	-2.16	0.59	41.46
ENSMUSG00000057329	Bcl2	-1.66	1.98	103.82
ENSMUSG00000025151	Maged1	-0.56	6.28	2067.64
ENSMUSG00000035692	Isg15	-1.42	3.43	289.95
ENSMUSG00000026669	Mcm10	-1.44	3.34	268.77
ENSMUSG00000079049	Serpinb1c	-3.22	0.58	38.5
ENSMUSG00000053580	Tanc2	-0.73	5.11	930.07
ENSMUSG00000051457	Spn	-1.17	5.13	942.29

ENSMUSG00000036432	Siah2	0.84	4.06	456.18
ENSMUSG00000026355	Mcm6	-1.28	6.13	1913.23
ENSMUSG00000074505	Fat3	-1.87	2.65	165.61
ENSMUSG00000021403	Serpinb9b	-3.1	1.14	57.64
ENSMUSG00000085399	Foxd2os	-1.69	1.05	55.58
ENSMUSG00000021687	Scamp1	0.61	6.2	2013.5
ENSMUSG00000047534	Mis18bp1	-1.02	3.53	280.29
ENSMUSG00000028555	Ttc39a	-1.94	0.82	49.82
ENSMUSG00000027883	Gpsm2	-1.07	3.51	276.73
ENSMUSG00000013089	Etv5	-2.45	3.34	300.15
ENSMUSG00000020961	Ston2	1.33	1.37	97.28
ENSMUSG00000024778	Fas	0.68	3.98	431.84
ENSMUSG00000032122	Slc37a2	-0.92	8.28	8210.59
ENSMUSG00000035352	Ccl12	1.52	0.76	64.33
ENSMUSG00000026640	Plxna2	-0.67	4.8	765.08
ENSMUSG00000029821	Dfna5	-1.75	2.35	134.07
ENSMUSG00000036768	Kif15	-1.32	3.53	310.2
ENSMUSG00000021965	Ska3	-1.7	2.09	114.3
ENSMUSG00000033323	Ctdp1	0.52	5.94	1684.24
ENSMUSG00000021579	Lrrc14b	-1.21	1.94	171.7
ENSMUSG00000006800	Sulf2	-1.75	5.29	1200.87
ENSMUSG00000034738	Nostrin	-1.16	4.13	481.26
ENSMUSG00000020340	Cyfip2	-0.54	6.14	1935.18
ENSMUSG00000029910	Mad2l1	-1.27	4.47	594.07
ENSMUSG00000021025	Nfkbia	0.84	7.63	5325.81
ENSMUSG00000031808	Slc27a1	-0.52	7.78	6127.28
ENSMUSG00000005233	Spc25	-2.05	3.68	352.86
ENSMUSG00000031097	Tnni2	-1.03	2.89	210.66
ENSMUSG00000020422	Tns3	-0.53	8.01	7126.59
ENSMUSG00000032528	Vipr1	-1.35	1.51	86.89
ENSMUSG00000034612	Chst11	-0.99	3.72	353.7
ENSMUSG00000090675	Olfr111	-3.55	-0.57	17.35
ENSMUSG00000039062	Anpep	-1.1	8.85	12577.01
ENSMUSG00000026034	Clk1	0.72	6.77	2778.61
ENSMUSG00000016382	Pls3	-0.7	5.48	1071.6
ENSMUSG00000020589	Fam49a	-0.65	5.51	1230.88
ENSMUSG00000022235	Cmbl	-3.94	-0.67	16.85
ENSMUSG00000022864	D16Ertd472e	1.04	2.72	175.88
ENSMUSG00000094777	Hist1h2ap	-1.46	4.54	578.36

ENSMUSG00000007080	Pole	-1.48	2.94	205.22
ENSMUSG00000037313	Tacc3	-1.26	5.09	830.43
ENSMUSG00000073555	Gm4951	1.28	1.99	105.46
ENSMUSG00000031756	Cenpn	-1.4	2.48	153.01
ENSMUSG00000037995	Igsf9	-2.48	0.62	35.36
ENSMUSG00000041552	Ptchd1	-2.81	1.08	52.82
ENSMUSG00000026238	Ptma	-0.88	8.17	11964.88
ENSMUSG00000081219	Bambi-ps1	-1.52	1.59	84.13
ENSMUSG00000050244	Heatr1	0.94	6.7	2833
ENSMUSG00000022667	Cd200r1	0.56	6.18	1996.97
ENSMUSG00000026039	Sgol2a	-1.36	3.02	220.11
ENSMUSG00000076437	Selenoh	-0.86	4.18	441.45
ENSMUSG00000022408	Fam83f	-1.65	3.07	227.34
ENSMUSG00000033740	St18	-0.98	3.01	190.98
ENSMUSG00000020868	Xylt2	-0.97	7.07	3675.72
ENSMUSG00000003228	Grk5	0.61	4.33	550.53
ENSMUSG00000028044	Cks1b	-1.13	3.64	303
ENSMUSG00000049327	Kmt5a	0.52	6.2	1953.56
ENSMUSG00000037907	Ankrd13b	-0.82	4.15	510.7
ENSMUSG00000030365	Clec2i	-0.91	2.83	173.04
ENSMUSG00000036853	Mcoln3	-1.16	3.27	233.25
ENSMUSG00000032640	Chsy1	0.98	5.07	919.73
ENSMUSG00000037628	Cdkn3	-1.44	2.28	132.64
ENSMUSG00000024732	Ccdc86	0.64	5.24	927.21
ENSMUSG00000022070	Bora	-0.94	2.54	218.16
ENSMUSG00000034765	Dusp5	-2.14	2.16	118.5
ENSMUSG00000026928	Card9	0.61	6.28	2314.46
ENSMUSG00000020092	Pald1	-0.88	4.65	609.32
ENSMUSG00000072812	Ahnak2	-0.58	5.47	1643.48
ENSMUSG00000018919	Tm4sf5	-1.74	0.38	32.93
ENSMUSG00000020649	Rrm2	-1.67	4.2	495.55
ENSMUSG00000004317	Clcn5	0.53	5.36	1009.24
ENSMUSG00000015143	Actn1	-0.69	6.99	3105.46
ENSMUSG00000030677	Kif22	-1.34	4.12	477.64
ENSMUSG00000020788	Atp2a3	-0.63	6.7	2583.17
ENSMUSG00000046718	Bst2	-0.71	6.54	2258.7
ENSMUSG00000005824	Tnfsf14	1.38	3.24	252.91
ENSMUSG00000022389	Tef	-0.49	6.38	2407.18
ENSMUSG00000074476	Spc24	-2.01	2.2	114.61

ENSMUSG00000032643	Fhl3	-1.07	5.26	1039.33
ENSMUSG00000036564	Ndrg4	-1.42	2.99	187.98
ENSMUSG00000028358	Zfp618	-3.47	-0.26	19.74
ENSMUSG00000032280	Tle3	0.79	6.97	3061.87
ENSMUSG00000021451	Sema4d	-0.57	7.6	5143.2
ENSMUSG00000022747	St3gal6	-3.74	-0.53	22.77
ENSMUSG00000001827	Folr1	-3.18	-0.51	20.44
ENSMUSG00000010461	Eya4	-1.42	1.35	91.84
ENSMUSG00000024236	Svil	0.69	6.45	2258.4
ENSMUSG00000052776	Oas1a	-0.71	5.9	1614.11
ENSMUSG00000006378	Gcat	-1.7	2.37	132.27
ENSMUSG00000020898	Ctc1	-0.69	4.69	920.31
ENSMUSG00000020935	Dcakd	-0.64	4.66	948.19
ENSMUSG00000076435	Acsf2	-0.8	3.14	334.7
ENSMUSG00000001348	Acp5	1.39	2.74	171.01
ENSMUSG00000027199	Gatm	-1.15	5.29	951.07
ENSMUSG00000027695	Pld1	0.8	5.15	876.66
ENSMUSG00000045763	Basp1	-1.16	7.39	4716.25
ENSMUSG00000030978	Rrm1	-1.18	5.83	1366.99
ENSMUSG00000005470	Asf1b	-1.39	4.07	432.64
ENSMUSG00000066152	Slc31a2	0.63	6.19	1921.77
ENSMUSG00000032725	Folr2	-2.88	5.03	NA
ENSMUSG00000021477	Ctsl	0.62	NA	42798.01
ENSMUSG00000070348	Ccnd1	-3.52	6.11	NA
ENSMUSG00000031138	F9	-2.63	-0.77	NA
ENSMUSG00000004040	Stat3	0.58	NA	6514.01
ENSMUSG00000038370	Pcp4l1	-2.77	5.07	NA
ENSMUSG00000029819	Npy	-2.69	4.87	NA
ENSMUSG00000078349	AW011738	-2.25	-0.56	NA
ENSMUSG00000015854	Cd5l	-2.11	7.17	NA
ENSMUSG00000015568	Lpl	-2.63	10.34	NA
ENSMUSG00000031555	Adam9	0.57	NA	10210.81
ENSMUSG00000027808	Serp1	0.94	NA	19122.82
ENSMUSG00000020901	Pik3r5	0.49	NA	11637.84
ENSMUSG00000028862	Map3k6	1.45	NA	538.52
ENSMUSG00000035493	Tgfbi	0.73	NA	8808.92
ENSMUSG00000019935	Slc17a8	-5.34	-1.59	9.33
ENSMUSG00000006445	Epha2	1.84	0.38	42.51
ENSMUSG00000021822	Plau	-3.27	5.03	NA

ENSMUSG00000029192	Tbc1d14	0.7	NA	4098.33
ENSMUSG00000044456	Rin3	1.02	NA	4953.88
ENSMUSG00000021536	Adcy2	-2.22	-0.06	NA
ENSMUSG00000001270	Ckb	-1.55	7.97	9796.47
ENSMUSG00000049313	Sorl1	0.9	NA	4234.75
ENSMUSG00000002944	Cd36	-1.92	8.22	NA
ENSMUSG00000001228	Uhrf1	-2.43	3.7	489.42
ENSMUSG00000067297	Ifit1bl2	-2.8	-0.97	22.02
ENSMUSG00000049625	Tifab	0.8	NA	3586.94
ENSMUSG00000033460	Armcx1	-2.43	-0.74	NA
ENSMUSG00000002032	Tmem25	-1.51	0.59	NA
ENSMUSG00000058099	Nfam1	0.47	NA	8950.75
ENSMUSG00000068747	Sort1	0.87	NA	8318.72
ENSMUSG00000090124	Ugt1a7c	0.49	NA	5806.2
ENSMUSG00000071714	Csf2rb2	0.47	NA	14193.63
ENSMUSG00000022565	Plec	-0.56	NA	8719.99
ENSMUSG00000018378	Cuedc1	-0.65	4.55	669.52
ENSMUSG00000019942	Cdk1	-1.33	NA	776.02
ENSMUSG00000026879	Gsn	-0.8	NA	13713.59
ENSMUSG00000028614	Ndc1	-0.8	4.04	383.28
ENSMUSG00000042377	Fam83g	-1.8	0.33	NA
ENSMUSG00000004267	Eno2	-0.94	2.89	176.74
ENSMUSG00000025420	Katnal2	-4.52	-0.57	15.83
ENSMUSG00000037994	Slc9b2	-4.45	-0.47	19.33
ENSMUSG00000062991	Nrg1	5.11	-1.83	9.41
ENSMUSG00000022034	Esco2	-1.95	1.96	92.84
ENSMUSG00000030346	Rad51ap1	-1.93	2.33	114.07
ENSMUSG00000038644	Pold1	-0.87	4.7	653.16
ENSMUSG00000052485	Tmem171	-2.01	NA	126.16
ENSMUSG00000021483	Cdk20	0.49	5.48	1385.78
ENSMUSG00000045287	Rtn4rl1	-1.22	2.18	NA
ENSMUSG00000070923	Klhl9	0.66	NA	3530.49
ENSMUSG00000020277	Pfkl	0.78	NA	4841.43
ENSMUSG00000078521	Aunip	-2.14	0.95	45.79
ENSMUSG00000018930	Ccl4	-1.75	NA	301.49
ENSMUSG00000039055	Eme1	-1.87	1.96	97.13
ENSMUSG00000038400	Pmepa1	-1.74	-0.31	NA
ENSMUSG00000043008	Klhl6	1.09	NA	2850.54
ENSMUSG00000021175	Cdca7l	-0.94	4.24	437.14

ENSMUSG00000050271	Prag1	-1.46	2.18	163.18
ENSMUSG00000039886	Tmem120a	-0.83	5.39	1458.84
ENSMUSG00000040964	Arhgef10l	-0.59	5.96	2255.75
ENSMUSG00000031530	Dusp4	-1.43	3.5	261.15
ENSMUSG00000032046	Abhd12	-0.69	8.61	8901.89

A.2 *KPten*$^{\Delta Duct}$ BMDM differentially expressed genes

The table below lists differentially expressed genes of *KPten*$^{\Delta Duct}$ BMDMs compared to M0 and NC BMDM controls. Genes are ranked by significance. Genes that are highlighted are shared with the *KPten*$^{\Delta Acinar}$ BMDMs.

gene_id	gene_name	log2FoldChange	log2CPM	baseMean
ENSMUSG00000041773	Enc1	-1.3	6.23	2037.51
ENSMUSG00000036362	P2ry13	2.34	3.57	320.44
ENSMUSG00000026712	Mrc1	2.2	9.48	19510.62
ENSMUSG00000102918	Pcdhgc3	1.31	5.14	974.2
ENSMUSG00000040829	Zmynd15	-2.16	2.47	147.23
ENSMUSG00000019960	Dusp6	1.67	6.28	2119.47
ENSMUSG00000017754	Pltp	-1.16	8.71	11294.35
ENSMUSG00000018920	Cxcl16	-1.68	6.65	2689.35
ENSMUSG00000021990	Spata13	-1.99	3.27	259.9
ENSMUSG00000038352	Arl5c	-1.21	3.9	401.44
ENSMUSG00000020592	Sdc1	-1.5	4.2	496.56
ENSMUSG00000060550	H2-Q7	-1.71	3.36	268.88
ENSMUSG00000037820	Tgm2	-0.89	8.53	10059.38
ENSMUSG00000044006	Cilp2	-1.42	3.11	233.28
ENSMUSG00000031004	Mki67	1.08	8.05	7214.69
ENSMUSG00000038151	Prdm1	-1.09	4.21	500.7
ENSMUSG00000002289	Angptl4	-1.77	2.71	176.06
ENSMUSG00000029299	Abcg3	1.24	3.93	412.49
ENSMUSG00000060477	Irak2	-0.86	5.74	1427.85
ENSMUSG00000047180	Neurl3	-0.99	7.9	6479.07
ENSMUSG00000024164	C3	-0.91	5.54	1264.78
ENSMUSG00000015766	Eps8	2.07	6.11	1873.69
ENSMUSG00000020023	Tmcc3	-1.4	3.96	421.18
ENSMUSG00000023034	Nr4a1	-1.46	3.72	356.18
ENSMUSG00000002983	Relb	-0.9	5.77	1463.63
ENSMUSG00000035342	Lzts2	-1.31	4.03	443.26
ENSMUSG00000079293	Clec7a	-1.81	6.1	1859.01
ENSMUSG00000030671	Pde3b	-1.01	5.27	1043.36
ENSMUSG00000049866	Arl4c	-0.74	7.74	5814.58
ENSMUSG00000030657	Xylt1	-1	4.33	660.88
ENSMUSG00000026580	Selp	3.22	2.15	117.56
ENSMUSG00000036181	Hist1h1c	-0.73	6.82	3064.27
ENSMUSG00000038811	Gngt2	-0.83	5.42	1158.54

ENSMUSG00000027848	Olfml3	-2.14	1.86	96.76
ENSMUSG00000025150	Cbr2	2.02	5.33	1088.65
ENSMUSG00000026360	Rgs2	-1.14	7.4	4582.98
ENSMUSG00000032575	Manf	0.78	6.62	2414.09
ENSMUSG00000037224	Zfyve28	-1.34	4.53	621.87
ENSMUSG00000051439	Cd14	-0.81	8.66	11019.67
ENSMUSG00000007872	Id3	-0.88	6.46	2386.05
ENSMUSG00000044716	Dok7	-5.05	-0.92	15.12
ENSMUSG00000031880	Rrad	-1.16	3.38	281.39
ENSMUSG00000025854	Fam20c	-0.96	8.07	7302.33
ENSMUSG00000044629	Cnrip1	0.73	5.23	1023.21
ENSMUSG00000024180	Tmem8	0.7	7.37	4492.61
ENSMUSG00000021451	Sema4d	-0.84	7.49	4855.31
ENSMUSG00000026628	Atf3	-1.29	7.51	4949.21
ENSMUSG00000031861	Lpar2	-1.23	2.53	154.74
ENSMUSG00000019818	Cd164	1.08	7.63	5375.46
ENSMUSG00000027611	Procr	-0.94	4.07	450.73
ENSMUSG00000017652	Cd40	-1.68	3.3	240.76
ENSMUSG00000027597	Ahcy	0.71	5.57	1275.51
ENSMUSG00000022408	Fam83f	-2.1	2.99	214.74
ENSMUSG00000006179	Prss16	1.52	3.46	294.02
ENSMUSG00000054545	Ugt1a6a	0.83	4.72	656.54
ENSMUSG00000022769	Sdf2l1	0.64	6.96	3447.67
ENSMUSG00000003882	Il7r	-1.28	6.07	1823.08
ENSMUSG00000033857	Engase	-0.82	5.51	1219.19
ENSMUSG00000047415	Gpr68	-2.14	1.51	75.29
ENSMUSG00000004609	Cd33	1.74	6.27	2461.96
ENSMUSG00000024737	Slc15a3	-0.99	7.94	6639.85
ENSMUSG00000023367	Tmem176a	-0.89	4.13	473.53
ENSMUSG00000032915	Adgre4	-2.47	2.97	211.69
ENSMUSG00000008305	Tle1	-1.47	3.91	390.19
ENSMUSG00000036353	P2ry12	1.23	3.15	213.25
ENSMUSG00000004267	Eno2	-1.2	2.81	174.47
ENSMUSG00000059824	Dbp	-0.91	5.64	1175.58
ENSMUSG00000076441	Ass1	-0.94	4.52	649.94
ENSMUSG00000048537	Phldb1	-1.2	3.94	413.58
ENSMUSG00000071068	Treml2	1.55	3.18	243.56
ENSMUSG00000057337	Chst3	-1.22	3.22	225.75
ENSMUSG00000039629	Strip2	2.74	0.83	47.85

ENSMUSG00000041046	Ramp3	-1.33	2.5	155.49
ENSMUSG00000025823	Pdia4	0.75	7.07	3733.69
ENSMUSG00000025225	Nfkb2	-0.71	6.56	2377.6
ENSMUSG00000038390	Gpr162	-1.95	4.6	672.89
ENSMUSG00000002602	Axl	-1.5	4.5	610.39
ENSMUSG00000015312	Gadd45b	-0.6	5.73	1770.41
ENSMUSG00000020334	Slc22a4	-0.99	3.02	242.32
ENSMUSG00000020571	Pdia6	0.67	NA	8547.57
ENSMUSG00000018919	Tm4sf5	-2.16	0.29	NA
ENSMUSG00000030787	Lyve1	3.59	-1.1	NA
ENSMUSG00000027398	Il1b	-3.21	NA	99.44
ENSMUSG00000022106	Rcbtb2	-0.66	NA	7384.58
ENSMUSG00000027435	Cd93	0.62	NA	15692.23
ENSMUSG00000036158	Prickle1	-3.4	-0.82	NA
ENSMUSG00000037405	Icam1	-0.6	NA	4796.51
ENSMUSG00000026864	Hspa5	0.76	NA	31101.83
ENSMUSG00000033207	Mamdc2	-2.23	NA	150.68
ENSMUSG00000034652	Cd300a	-0.59	NA	8684.72
ENSMUSG00000031451	Gas6	0.7	NA	23034.87

A.3 *KPten*$^{\Delta Acinar}$ BMDM gene ontology pathways

The table below lists significant gene ontology pathways expressed by *KPten*$^{\Delta Acinar}$ BMDMs analyzed by Enrichr. Pathways highlighted in yellow are shared with the KIC macrophages in Hosein et al. (Hosein et al., 2019).

Term	-log10(P-value)	Genes
neutrophil mediated immunity (GO:0002446)	3.30	ITGAM;ARG1;NFAM1;CARD9;FGL2;PLAUR;PYGL;SCAMP1;PLD1;AP2A2;PYCARD;BST1;PFKL;LRG1;SELL;CRISPLD2;LCN2;PRTN3;CD33
cytokine-mediated signaling pathway (GO:0019221)	3.30	CCR1;IFITM1;RNASEL;IFITM2;ITGAM;TNFSF14;CISH;CEBPD;STAT3;SLA;IRS2;CSF2RB;PYCARD;SOCS2;NFKBIA;SOCS3;LCN2;PRTN3;STX3;CD300LF;CCR2
neutrophil degranulation (GO:0043312)	3.30	ITGAM;ARG1;NFAM1;FGL2;PLAUR;PYGL;SCAMP1;PLD1;AP2A2;PYCARD;BST1;PFKL;LRG1;SELL;CRISPLD2;LCN2;PRTN3;CD33
cellular response to cytokine stimulus (GO:0071345)	3.30	CCR1;GBP5;IFITM2;GBP7;ITGAM;CEBPD;STAT3;SLA;CSF2RB;PYCARD;SOCS2;SOCS3;SBNO2;LCN2;PRTN3;STX3;TLR4;CCR2
neutrophil activation involved in immune response (GO:0002283)	3.30	ITGAM;ARG1;NFAM1;FGL2;PLAUR;PYGL;SCAMP1;PLD1;AP2A2;PYCARD;BST1;PFKL;LRG1;SELL;CRISPLD2;LCN2;PRTN3;CD33
positive regulation of cytokine production involved in inflammatory response (GO:1900017)	2.28	GBP5;CARD9;STAT3;TLR4
cellular response to interleukin-7 (GO:0098761)	2.20	SOCS2;CISH;STAT3;IRS2
interleukin-7-mediated signaling pathway (GO:0038111)	2.20	SOCS2;CISH;STAT3;IRS2
regulation of cytokine production involved in inflammatory response (GO:1900015)	1.95	PYCARD;GBP5;CARD9;STAT3;TLR4
negative regulation of cytokine production (GO:0001818)	1.88	PYCARD;SRGN;CD274;CD200R1;RARA;KLF4;FCGR2B;TLR4;CD33
regulation of interleukin-10 production (GO:0032653)	1.85	PYCARD;CD274;STAT3;FCGR2B;TLR4
negative regulation of tumor necrosis factor superfamily	1.85	CD274;ARG2;RARA;TLR4;CD33

cytokine production (GO:1903556)		
positive regulation of cytokine production (GO:0001819)	1.80	PYCARD;GBP5;CD274;SPHK1;NFAM1;CARD9;STAT3;RARA;FLOT1;TLR4;SORL1;CCR2
regulation of tumor necrosis factor production (GO:0032680)	1.58	PYCARD;ARG2;STAT3;RARA;TLR4;CD33;CCR2
positive regulation of interleukin-10 production (GO:0032733)	1.55	PYCARD;CD274;STAT3;TLR4
regulation of immune response (GO:0050776)	1.39	IFITM1;CD200R1;SELL;TREML2;AHR;CD300LF;FCGR2B;CD33
cellular component disassembly (GO:0022411)	1.38	CTSL;FLOT1;HTRA1;MMP19;FURIN
extracellular matrix disassembly (GO:0022617)	1.38	CTSL;FLOT1;HTRA1;MMP19;FURIN
cellular protein modification process (GO:0006464)	1.38	PTPN1;RNASEL;CTDP1;CISH;TIPARP;CP;F5;MTM1;KLHL9;TGM1;SOCS2;SOCS3;SERP1;GRK5;GRK6;CDK20;ST3GAL4;RARA;GCNT2;ASB4;FBXL5;MAP3K6
regulation of cell communication (GO:0010646)	1.38	SOCS2;PTPN1;GRK5;GRK6
negative regulation of phagocytosis (GO:0050765)	1.36	PRTN3;CD300LF;FCGR2B
regulation of adaptive immune response (GO:0002819)	1.32	PYCARD;AHR;FCGR2B
dendritic cell migration (GO:0036336)	1.32	CCR1;EPS8;CCR2
response to cytokine (GO:0034097)	1.32	SELP;CD274;IFITM1;IFITM2;SPHK1;STAT3;ADAM9
positive regulation of DNA-binding transcription factor activity (GO:0051091)	1.32	FZD1;PYCARD;NFKBIA;SPHK1;NFAM1;CARD9;STAT3;FLOT1;TLR4
regulation of neuroinflammatory response (GO:0150077)	1.32	CD200R1;SPHK1;NUPR1
regulation of cytokine-mediated signaling pathway (GO:0001959)	1.32	PYCARD;SOCS3;PTPN1;RNASEL;SPHK1
positive regulation of NF-kappaB transcription factor activity (GO:0051092)	1.32	PYCARD;NFKBIA;SPHK1;CARD9;STAT3;FLOT1;TLR4

cellular response to hormone stimulus (GO:0032870)	1.32	SOCS2;CTSL;STAT3;ARID5A;RARA
positive regulation of leukocyte tethering or rolling (GO:1903238)	1.32	SELP;ST3GAL4
growth hormone receptor signaling pathway (GO:0060396)	1.32	SOCS2;PTPN1;STAT3
cellular response to molecule of bacterial origin (GO:0071219)	1.32	PYCARD;CD274;SBNO2;ADAM9;FCGR2B;TLR4
organonitrogen compound biosynthetic process (GO:1901566)	1.32	ARG2;CERS6;ARG1;SPHK1;ST3GAL4;FURIN;CEPT1
regulation of inflammatory response (GO:0050727)	1.32	NFKBIA;BST1;CD200R1;SBNO2;SPHK1;KLF4;TLR4;CCR2
regulation of B cell proliferation (GO:0030888)	1.32	BST1;IRS2;AHR;FCGR2B
negative regulation of tumor necrosis factor production (GO:0032720)	1.32	ARG2;RARA;TLR4;CD33
response to interferon-gamma (GO:0034341)	1.31	GBP5;IFITM1;IFITM2;GBP7;TLR4
positive regulation of neuron death (GO:1901216)	1.31	ITGAM;NUPR1;FCGR2B;TLR4

A.4 *KPten*$^{\Delta Duct}$ BMDM gene ontology pathways

The table below lists significant gene ontology pathways expressed by *KPten*$^{\Delta Duct}$ BMDMs analyzed by Enrichr. Pathways highlighted in yellow are shared with the KIC macrophages in Hosein et al. (Hosein et al., 2019).

Term	-log10(P-value)	Genes
positive regulation of ruffle assembly (GO:1900029)	1.38	P2RY12;EPS8
regulation of ruffle assembly (GO:1900027)	1.38	P2RY12;EPS8
chaperone cofactor-dependent protein refolding (GO:0051085)	1.38	SDF2L1;HSPA5
platelet degranulation (GO:0002576)	1.38	SELP;GAS6;MANF
negative regulation of interleukin-1 production (GO:0032692)	1.38	GAS6;CD33
'de novo' posttranslational protein folding (GO:0051084)	1.38	SDF2L1;HSPA5
calcium-dependent cell-cell adhesion via plasma membrane cell adhesion molecules (GO:0016339)	1.31	SELP;PCDHGC3

A.5 KIC macrophage markers expressed by *KPten*$^{\Delta Acinar}$ BMDMs and *KPten*$^{\Delta Duct}$ BMDMs

The table below lists the gene expression levels (FPKM) of KIC macrophage markers in *KPten*$^{\Delta Acinar}$ BMDMs and *KPten*$^{\Delta Duct}$ BMDMs. Genes are listed in alphabetical order.

Gene name	***KPten*$^{\Delta Acinar}$ BMDMs**		***KPten*$^{\Delta Duct}$ BMDMs**	
	321A-BMDM	333A-BMDM	409-BMDM	746A-BMDM
1600014C10Rik	51.9184	55.4094	40.3693	19.1184
2010107E04Rik	165.398	160.74	208.472	182.471
A930007I19Rik	0.0213182	0.0585111	0.0794342	0.0199118
AB124611	179.663	168.128	145.079	128.47
AF251705	206.023	185.466	175.771	175.781
AI607873	93.3644	93.6343	88.4599	99.392
AI662270	79.857	81.1667	87.9093	81.7465
AW112010	26.1331	28.7096	15.7083	12.478
Abca1	46.2447	38.4536	33.4171	38.1484
Abracl	58.3334	61.0983	68.5753	69.2816
Acp5	8.34846	6.88632	4.97431	2.86794
Actb	1242.6	1255.24	1431.93	1412.74
Actr2	141.6	134.498	161.794	166.117
Actr3	203.6	197.463	198.557	214.519
Adam8	422.91	445.894	410.179	508.454
Adamdec1	0	0	0	0
Adgre1	350.551	364.514	337.341	411.107
Adssl1	69.3475	65.0762	54.1148	56.6205
Agpat9	0.895197	0.881248	0.613618	0.536805
Aif1	11.8732	10.5703	15.7676	13.0115
Alas1	30.0268	33.9225	31.5318	29.9466
Aldh3b1	65.3089	62.482	57.0102	54.5523
Alox5ap	655.015	676.665	634.385	617.99
Amica1	29.3175	33.4685	12.7049	8.05247
Ankrd33b	12.8157	12.3534	8.68651	9.51249
Ap1s2	55.1661	58.6262	73.9187	73.0504
Ap2s1	355.256	383.859	455.954	385.221
Apbb1ip	75.9387	80.2306	75.7915	81.1442
Apoe	7249.13	5901.98	4883.47	4221.11
App	376.821	373.886	438.553	434.524
Arg1	0.597261	0.834421	0.360017	0.425573
Arg2	9.87262	11.3045	3.46606	1.3726
Arhgap31	17.8993	19.4311	16.0711	17.4305

Arhgap9	90.5654	88.5929	82.3623	81.887
Arhgdib	497.133	497.272	501.133	461.615
Arih2	18.0716	18.0883	14.3625	14.8115
Arpc1b	587.539	608.785	683.961	649.004
Arpc2	413.399	428.912	482.701	501.444
Arpc3	502.746	482.84	641.667	615.633
Arpc4	131.714	141.883	155.485	152.89
Arpc5	271.349	285.497	308.094	291.029
Arrb2	186.336	189.359	205.085	214.351
Arrdc4	34.796	36.8938	25.7728	19.643
Asah1	292.286	282.742	275.695	241.641
Atf4	114.257	113.211	93.9334	97.9331
Atox1	316.298	343.634	319.256	320.36
Atp11b	17.9704	19.473	17.7991	18.0383
Atp13a2	188.214	194.237	195.981	165.51
Atp1a1	175.245	180.968	190.011	208.793
Atp1b3	221.075	219.601	233.963	225.19
Atp5e	353.594	367.543	433.477	382.096
Atp5l	31.5082	30.9402	34.3436	29.3565
Atp6ap1	282.85	287.466	289.7	297.839
Atp6ap2	115.599	112.833	146.184	141.221
Atp6v0b	453.262	473.826	453.184	429.592
Atp6v0d1	181.055	181.592	205.852	190.208
Atp6v1a	180.229	175.504	208.286	236.377
Atp6v1b2	200.379	195.231	190.915	196.435
Atp6v1e1	189.241	192.303	204.283	179.606
Atp6v1f	358.403	349.316	346.932	364.588
Atp6v1g1	186.658	189.348	210.634	193.245
B2m	2016.66	2168.57	2165.65	2103.77
BC005537	210.927	228.412	200.958	257.62
BC028528	45.9184	48.573	43.6029	46.3407
Basp1	61.61	62.9692	73.5081	85.6588
Bcl10	61.9948	63.9822	57.5836	55.947
Bcl2a1a	0.296083	0.471272	0.275855	0.205526
Bcl2a1b	247.13	232.125	242.47	173.97
Bcl2a1c	0.172625	0	0.160932	0.157213
Bcl2a1d	1.55444	2.89496	1.99995	0.959122
Bcl2l11	22.7215	20.8317	17.6895	17.2218
Bhlhe40	14.7545	15.4553	13.3679	11.2393

Bin2	79.3881	77.9047	69.5628	58.3472
Birc3	50.1423	52.8996	36.3378	33.3539
Btg1	73.4543	80.9294	48.4827	31.7881
C1qa	360.035	356.843	465.576	394.217
C1qb	2835.42	2696.99	3016.32	2841.28
C1qc	1615.7	1600.69	1893.51	1726.88
C3ar1	188.744	186.621	174.702	193.805
C5ar1	127.876	123.654	104.236	125.223
Calm1	132.346	140.184	182.578	181.801
Capza2	163.698	178.121	177.354	171.585
Casp4	20.0962	26.1326	20.9393	16.2685
Ccdc71l	14.1977	15.8373	14.0151	14.4954
Ccl2	25.8571	38.0312	64.3317	19.6212
Ccl24	1.06841	0.825273	2.10548	1.26225
Ccl3	37.0012	41.3331	43.0394	45.0327
Ccl4	9.21741	10.8648	19.213	30.7588
Ccl6	1321.88	1285.19	862.084	330.216
Ccl9	396.351	393.762	356.647	263.244
Ccnl1	40.5041	44.0684	33.7354	30.7407
Ccr1	54.919	62.756	73.9038	27.0156
Ccr2	24.1585	23.5412	14.8117	9.87326
Ccr5	33.7089	32.7997	19.3625	13.3829
Ccrl2	19.7703	19.7615	11.7989	11.5066
Cd14	307.658	325.488	185.202	223.429
Cd274	11.3811	13.4496	7.4113	4.41094
Cd300a	91.3117	84.3633	57.3669	57.9495
Cd300lf	88.5357	99.405	63.2356	37.1277
Cd302	65.2279	68.0391	57.5558	40.9581
Cd33	46.1773	60.5696	58.2413	40.4342
Cd38	9.53137	7.40671	4.80862	0.907695
Cd48	139.478	137.349	141.458	140.569
Cd52	353.348	379.406	334.977	332.029
Cd53	196.046	186.658	180.662	169.208
Cd68	874.66	884.566	1145.75	1283.77
Cd74	12.5326	13.2758	12.0371	9.63133
Cd80	7.73382	6.95913	6.70183	7.71594
Cd83	10.4835	9.62872	12.3832	16.5572
Cd84	165.196	163.25	180.31	189.918
Cd86	5.52305	6.09671	5.16284	4.79962

Cd93	74.5258	68.0197	101.821	114.424
Cdc42	327.124	332.455	380.252	385.049
Cdc42ep4	11.2404	11.6025	12.2357	12.5632
Cdkn1a	218.866	226.92	218.362	226.955
Cebpb	243.737	277.247	201.741	135.302
Cfh	72.7263	67.2118	44.8115	33.6187
Cflar	8.57276	8.91751	8.34998	8.88683
Cfp	551.681	565.624	533.793	458.862
Chil3	419.686	381.634	128.343	50.5326
Chmp2a	146.586	139.855	141.854	133.598
Clec10a	61.3769	46.9933	35.5971	26.7459
Clec4a2	24.8128	27.8644	22.4318	21.3223
Clec4a3	88.9103	86.1005	54.6818	51.9206
Clec4d	682.047	740.01	543.371	519.934
Clec4e	22.8849	32.223	17.8526	16.6507
Clec4n	150.909	184.243	88.7323	58.2067
Clec5a	5.15011	7.56432	7.90085	8.40049
Clta	428.889	430.517	615.831	583.606
Cmip	45.926	43.7471	41.931	43.6047
Cmtm7	107.692	100.955	115.715	112.6
Cndp2	305.498	286.656	321.817	337.29
Coro1a	200.224	197.583	189.782	202.238
Coro1b	262.089	261.648	247.209	229.033
Cotl1	474.571	456.216	588.745	564.188
Cox17	121.91	119.955	129.091	117.254
Cox4i1	735.562	696.337	700.092	677.102
Cox5b	201.601	198.639	242.284	225.195
Cox8a	472.965	476.764	473.945	416.089
Creb5	3.97517	4.90825	3.48233	5.24951
Creg1	367.912	371.826	313.943	334.373
Crem	7.39118	6.56275	7.02472	5.47916
Csf1r	1103.82	1147.02	925.266	1033
Csf2ra	75.2353	99.5096	80.4097	82.1702
Csf2rb	169.637	183.179	91.3433	56.4159
Csf2rb2	133.056	135.162	72.9413	61.6686
Csrnp1	11.2455	12.3399	8.20494	6.67796
Cst3	1521.35	1459.98	1500.83	1626.17
Cstb	547.748	555.504	588.455	596.125
Ctsa	471.148	468.174	443.59	439.931

Ctsb	3919.35	3714.2	4615.97	4712.46
Ctsc	82.4459	91.2453	90.409	82.8384
Ctsd	11079.4	10083.7	10863.1	10138.6
Ctsh	255.58	239.618	175.55	154.534
Ctss	3306.45	3203.74	2588.62	2096.56
Ctsz	802.967	805.063	854.31	747.352
Cxcl1	1.60054	2.43022	1.15976	0.715062
Cxcl16	23.8226	25.1429	18.4491	23.9258
Cxcl2	3.23041	5.75364	2.72735	1.92319
Cxcl3	0.489544	1.09078	0.101349	0.0505144
Cyba	1189.66	1226	1156.64	981.93
Cybb	258.081	285.306	162.007	177.955
Cyp4f18	28.6793	19.8376	23.0909	20.2697
Cyth1	70.5015	69.8105	57.3452	54.754
Cytip	7.61715	7.00908	5.24702	5.34244
Dab2	141.469	162.384	226.102	226.206
Dapk1	39.1168	42.5411	23.4561	27.6885
Dazap2	277.145	275.139	275.182	272.034
Dbi	167.786	167.296	210.966	177.891
Dcstamp	0.0301719	0.22063	0.0771197	0.0562784
Ddx5	166.985	181.6	175.912	169.762
Dennd4a	9.8345	9.20555	6.30234	6.15595
Dirc2	17.6509	17.3224	15.627	14.1595
Dmxl2	10.4541	11.2109	6.55016	5.00505
Dock10	34.4257	34.3896	30.487	36.9495
Dok2	22.2925	24.1967	23.6663	25.492
Dok3	64.313	70.3413	71.8132	63.1158
Dpep2	147.818	160.091	121.36	121.255
Dpys	0.0198848	0.0545855	0.05557	0.0371551
Dtx4	28.1594	23.2995	21.9951	22.7922
Dusp1	58.3081	61.9011	54.5573	50.7261
Dusp16	3.18615	3.64209	1.96138	2.70142
Dusp3	76.3461	70.6621	59.8631	58.3504
Dusp5	0.981642	0.682322	1.04514	0.86937
Ear1	0	0	0	0
Ear10	0	0	0	0
Ear2	0.340336	0.309169	0.124261	0
Efhd2	250.53	258.064	247.027	274.166
Ehd1	37.6771	40.9258	37.2169	41.628

Eif4a1	200.015	200.643	206.319	223.631
Eif4e	12.459	13.8733	17.5578	17.7134
Eif5	71.047	70.0339	63.1858	61.8027
Ell2	9.21785	10.3889	8.91673	12.9699
Emb	362.314	376.166	268.115	173.032
Emilin2	206.685	236.134	180.755	134.704
Erp29	208.06	200.341	197.701	216.626
Ets2	9.36389	10.86	7.8553	9.43953
Evi2a	79.4187	89.4265	84.682	103.421
F10	7.47014	7.70362	2.36419	0.76235
F13a1	258.198	281.358	304.57	179.183
F7	1.65925	3.38223	1.95109	0.862933
Fam105a	64.9448	62.2049	65.7186	62.319
Fam134b	43.6744	36.6997	38.733	42.1163
Fam49b	41.2345	43.1314	45.138	40.6916
Fam96a	100.235	96.1783	121.194	100.433
Fcer1g	830.657	873.565	941.736	974.084
Fcgr1	59.4355	52.7818	48.8125	35.906
Fcgr2b	170.13	182.184	110.788	56.9688
Fcgr3	1212.8	1266.29	1167.82	968.068
Fcgr4	135.74	116.273	72.3727	49.6626
Fem1c	16.8919	14.0024	13.5233	15.1553
Fermt3	188.202	190.085	185.628	181.748
Fes	119.831	127.553	103.194	91.6823
Fgr	0.792331	0.923301	0.496516	0.498458
Fn1	4.01673	3.37337	0.972022	0.727491
Fosl2	24.7651	26.0321	15.0654	12.2453
Fpr1	10.8446	19.9112	5.0513	3.0438
Fpr2	10.9029	17.4834	4.48886	2.85088
Fth1	17574.8	17993.3	17032.9	14426.7
Ftl1	9695.19	10065.2	10836.4	10928
Furin	72.1606	79.4826	64.0144	47.8412
Fxyd5	785.987	797.831	651.219	616.596
Gabarap	494.579	485.763	498.39	473.952
Gadd45a	24.5331	19.9191	20.0488	17.8301
Gadd45b	58.2877	62.052	39.4448	38.0395
Gas2l3	6.82726	6.50726	9.5299	9.95677
Gas7	57.0447	54.1798	44.6272	32.8135
Gatm	11.5514	11.6791	17.3882	19.5276

Gda	149.793	144.981	96.3827	47.6352
Gde1	63.0634	66.2873	62.0831	57.5162
Gdi2	276.079	267.72	299.472	301.19
Gdpd3	0.513285	0.65524	0.90855	0.620009
Glrx	22.8848	27.9675	29.1657	38.2855
Gltp	218.145	222.243	218.58	220.332
Gm2a	86.4276	83.1629	79.2894	72.1481
Gm5150	4.97549	5.77744	2.43358	1.61504
Gm6377	2.27683	2.13168	2.03996	2.94033
Gmfg	95.1914	93.0288	101.344	98.6824
Gna13	40.3009	39.3757	37.7303	39.1925
Gng2	67.699	65.3751	70.0181	71.4324
Gngt2	78.1191	66.2795	72.9409	65.6207
Gns	349.368	344.706	338.011	292.239
Gpi1	225.463	228.326	207.53	204.477
Gpr132	5.74746	7.75001	5.01577	4.82301
Gpr171	4.54464	5.84885	2.6978	0.582525
Gpr65	45.9059	44.2144	35.6645	49.1569
Gpsm3	106.971	103.611	104.069	93.9855
Gpx1	821.976	856.956	852.018	872.698
Grn	1571.07	1578.23	1989.7	2056.22
Gsap	7.43631	8.34265	5.90339	5.42621
Gsr	89.8664	94.6088	54.0146	47.1332
Gtf2b	47.6987	44.7774	46.3762	45.654
Gusb	311.787	305.492	388.064	441.591
Gyg	103.574	98.428	108.274	104.876
H2-Aa	0.461437	0.561006	0.334352	0.524037
H2-Ab1	0.494891	1.23157	1.25738	0.962537
H2-D1	1672.03	1656.28	1433.32	1458.05
H2-DMa	11.0365	12.9321	15.2494	11.2113
H2-DMb1	19.1122	19.9336	21.1503	20.5559
H2-DMb2	0.677195	1.50541	0.560827	0.696259
H2-Eb1	0.183603	0.755106	0.370578	0.770459
H2-K1	966.737	998.499	835.077	805.818
H3f3a	175.806	185.223	185.441	167.48
H3f3b	266.65	266.693	294.418	273.663
Hacd4	75.7725	68.3866	79.722	76.0451
Hal	0.0176704	0.0485189	0.0164603	0.0495454
Hck	48.5613	52.5663	49.5427	50.6323

Hcls1	176.835	170.879	176.782	189.064
Hcst	44.7004	40.0833	33.0792	41.3352
Hebp1	25.9718	25.0017	31.2328	23.8902
Hexa	869.506	813.605	900.058	918.715
Hexb	125.642	118.312	172.597	192.105
Hfe	80.1346	78.3782	78.0353	76.7251
Hif1a	45.5385	45.9234	29.5636	23.3937
Hilpda	10.136	11.2494	8.44068	5.62464
Hk2	16.6691	15.6948	10.378	9.22971
Hmox1	521.458	566.511	524.782	535.024
Hnrnpa2b1	176.348	177.232	223.419	222.003
Hopx	4.6717	4.43468	2.2728	1.06727
Hp	149.855	143.65	57.2836	26.8436
Hspa5	560.899	533.471	762.177	723.82
Id2	85.0102	92.1115	64.9651	73.5274
Ier3	59.1022	69.9311	44.0948	16.9904
Ier5	35.3508	32.649	32.2018	34.0352
Ifi30	77.8677	85.8755	109.398	105.523
Ifitm1	20.8592	25.2262	6.85426	6.26418
Ifitm2	1182.44	1170.06	782.087	667.193
Ifitm3	981.955	954.745	758.289	715.611
Ifngr1	225.563	215.428	154.057	154.271
Ifrd1	46.2861	47.9169	32.5069	30.2959
Igsf6	133.2	146.33	85.3786	76.4074
Ikbkb	38.0714	38.7728	32.54	31.8316
Il10rb	172.779	168.743	201.082	213.653
Il1a	0.177771	0.139342	0.0473145	0
Il1b	0.993264	1.77744	0.81427	0.480881
Il1r2	0.665549	1.03665	0.182356	0.18227
Il1rn	1.63155	1.52611	1.21854	0.943766
Il23a	0.154606	0.10588	0.0720139	0.107979
Il4ra	172.2	184.036	177.93	91.4075
Il6	0.100505	0.274963	0	0
Inpp5d	137.242	135.499	140.254	139.552
Insig1	23.7742	20.5075	29.1786	26.9948
Iqgap1	128.371	120.094	114.546	144.408
Irak2	23.1871	20.3099	13.9776	14.3924
Irf2bp2	39.5594	44.6094	41.7849	33.835
Irf5	92.933	94.3944	73.2666	86.9541

Isg15	9.81683	10.7947	13.8669	17.0573
Itgam	388.509	404.842	358.744	283.174
Itgax	0.426475	0.379738	0.275877	0.64283
Itgb2	385.441	376.031	366.987	382.734
Itgb5	165.854	150.92	185.323	192.195
Jarid2	6.25721	6.69222	5.45126	5.592
Junb	111.022	127.073	90.0504	70.2704
Kctd12	68.4248	66.5019	59.0086	52.4599
Kdm6b	5.82716	5.96598	4.66658	2.90299
Kdm7a	9.41699	9.44189	6.66708	5.14332
Klf6	83.3249	82.095	70.3022	75.8421
Klra2	1.10574	1.50329	1.15525	0.423193
Lacc1	22.7476	26.6222	28.942	32.8642
Lamp1	1758.7	1750.55	1837.59	1689.16
Lamp2	397.803	397.294	418.968	421.315
Lamtor2	238.023	225.416	257.026	225.352
Laptm5	996.327	984.331	1010.13	1030.69
Larp4b	22.3196	22.1114	22.8707	22.3914
Lcp1	233.288	245.298	299.185	350
Lcp2	42.6904	44.3531	44.2267	40.9173
Lgals3	1343.18	1305.7	1336.39	1510.17
Lgmn	726.344	662.853	1041.34	908.433
Lilr4b	101.091	131.04	111.721	109.961
Lilrb4a	252.025	340.251	251.524	226.631
Litaf	219.173	212.311	208.974	160.835
Lmnb1	3.25018	4.19623	17.592	20.5304
Lrg1	12.6649	14.1538	4.1258	0.578815
Lrrc8d	26.868	25.6819	21.2459	20.4182
Lrrfip1	48.4809	48.6332	46.9303	48.1556
Lst1	136.939	123.414	147.658	137.305
Ltc4s	47.968	50.7408	56.575	36.8103
Ly86	120.96	112.172	85.7646	83.1931
Lyn	110.648	108.076	105.691	109.081
Lyz2	26258.5	27875	22736.2	19761.9
M6pr	159.408	165.6	162.252	168.617
Mafb	75.8012	74.5513	83.0256	72.8265
Maff	10.3877	10.4363	6.7622	6.1696
Malt1	6.00012	6.0239	6.00211	5.72186
Man2a1	96.1672	93.1818	76.9401	89.2118

Man2b1	330.394	322.711	275.958	284.743
Mapkapk2	91.6451	100.143	84.5695	89.7517
Marc1	0.0464409	0.042479	0	0
Marc2	44.6248	40.5327	39.4018	39.8439
March1	25.7253	25.7224	19.663	16.7369
March2	69.8009	74.3737	70.3223	64.742
Marcksl1	17.4757	25.5213	16.8174	21.9722
Mcemp1	3.78213	4.76011	1.42722	0.445108
Mcl1	287.33	294.109	267.394	233.095
Mdm2	55.2439	55.6788	52.1841	55.8414
Mertk	142.012	145.189	113.527	103.424
Metrnl	57.841	53.7095	59.5744	65.218
Mfsd1	134.625	132.237	171.493	158.363
Mgst1	268.319	266.421	179.23	131.321
Milr1	44.7487	44.101	54.6087	61.1078
Mmp12	12.9861	12.5	9.71939	10.6918
Mpeg1	1435.28	1301.71	1213.52	1312.32
Mrc1	82.4343	113.369	261.922	211.766
Mrpl23	11.5753	14.2855	14.6988	15.3363
Ms4a6b	175.241	179.067	260.022	234.255
Ms4a6c	467.601	485.631	536.97	476.387
Ms4a6d	483.859	538.271	588.195	435.072
Msr1	83.242	101.047	121.367	115.366
Msrb1	716.133	748.278	490.013	391.807
Mt1	486.588	452.281	433.012	359.922
Myeov2	221.038	230.637	268.868	232.543
Naaa	33.2333	40.7743	22.1841	15.2861
Nampt	51.1707	56.3021	44.8964	39.5208
Napsa	112.568	115.871	72.2519	66.8435
Nceh1	87.7474	83.1748	91.9764	100.568
Ncf1	392.743	395.282	347.499	307.314
Ncf2	153.334	151.727	134.948	130.576
Ncf4	104.942	120.228	79.7016	68.3477
Nckap1l	188.278	194.817	178.064	187.891
Neu1	45.1532	44.5222	45.7947	41.369
Neurl3	85.6507	76.2819	61.7906	69.7056
Nfe2l2	110.477	114.875	111.885	116.899
Nfil3	59.5397	57.0239	28.3642	16.5222
Nfkb1	34.168	36.7284	33.4761	35.9615

Nfkbia	168.062	202.907	130.8	95.3363
Nfkbib	34.5969	36.6452	34.4836	33.0031
Nfkbid	5.40244	7.58171	5.00939	4.74078
Nfkbie	4.81587	7.66453	5.94052	6.52436
Nfkbiz	3.4716	5.95706	2.64809	2.73162
Ninj1	443.419	445.223	353.773	365.879
Nlrp3	24.0261	27.1958	22.3361	22.4669
Nov	0	0	0	0
Npc2	434.947	429.043	405.089	415.658
Npl	8.71886	9.11954	14.8561	12.2164
Nr4a3	0.250372	0.109254	0.0787293	0.152357
Nrg1	0.189532	0.108346	0.0662086	0
Nrros	81.7602	90.0744	85.5028	87.1753
Ntpcr	39.4527	37.0586	36.6235	34.2532
Olr1	0	0	0	0
Osbpl9	91.7922	86.9098	87.8443	76.1367
Oser1	10.188	10.3631	10.3201	10.8489
Osgin2	4.43177	4.59663	5.12596	4.72816
Osm	9.73478	8.12925	8.06077	5.2193
Ostf1	168.977	166.313	193.021	198.404
P4hb	234.887	233.753	266.368	261.509
Pde4b	11.6857	11.6333	6.43962	5.74152
Pf4	105.105	99.456	278.186	173.872
Pgd	428.564	446.85	317.542	300.875
Phlda1	2.18422	2.60829	1.65169	1.82272
Picalm	248.326	242.132	184.213	153.932
Pid1	88.2887	94.8657	111.42	132.987
Pik3r1	20.5245	20.1342	19.3955	22.854
Pik3r5	117.2	127.237	75.506	71.7323
Pilra	2.40262	3.13359	1.88564	1.76776
Pim1	31.4856	35.6917	24.4195	19.1562
Pim3	24.294	25.0397	17.7784	15.9854
Pira2	6.80403	6.3368	6.56503	5.59045
Pirb	355.103	391.142	234.141	189.748
Pitpna	161.63	170.744	163.051	175.156
Pla2g7	112.996	125.292	95.696	91.6291
Plaur	42.7961	48.0153	28.487	19.6162
Plbd1	0.584104	0.650263	0.378516	0.59259
Pld3	241.225	239.514	227.939	220.55

Pld4	222.175	223.426	239.469	216.998
Plek	84.0419	79.0916	105.929	118.693
Plet1	0.109392	0	0.0509517	0
Plgrkt	60.653	61.832	50.2936	39.7515
Plin2	1104.22	983.64	813.214	840.672
Plk3	1.2915	2.05834	2.73601	2.33497
Plxdc2	8.45364	8.29565	2.82127	2.64078
Pmvk	18.2032	18.9783	13.0512	11.841
Pnrc1	76.1868	77.7343	62.6532	62.9629
Ppig	15.7183	15.7331	15.4807	13.8942
Ppp1r15a	26.2169	25.3991	20.2234	17.6891
Ppt1	161.799	161.931	134.63	113.261
Prcp	30.9743	27.365	25.9266	25.2083
Prdx5	751.284	699.165	524.492	404.736
Prkcd	161.309	162.311	140.876	137.05
Prtn3	2.48118	1.57731	0.806355	0.482003
Psap	9801.59	9071.86	8084.98	6702.5
Psma6	158.285	168.716	153.701	147.375
Psmb8	92.9394	88.7647	104.614	106.351
Ptafr	54.7854	51.3053	42.9866	45.1002
Ptbp3	37.1871	37.774	43.0239	45.18
Ptgs1	41.9074	36.8688	32.9235	21.2428
Ptgs2	0.33315	0.220955	0.0856081	0.171975
Ptp4a1	8.9823	8.78371	6.4051	5.67845
Ptpn1	145.051	149.943	119.787	99.504
Ptpn18	45.1731	45.729	47.3227	47.5065
Ptpn6	142.099	149.081	149.791	151.062
Ptprc	98.3964	97.4684	87.9374	93.0489
Ptpre	18.1807	17.8612	16.0511	16.1628
Pycard	53.9012	54.3755	50.4497	37.5337
Pygl	160.431	167.177	106.367	68.8581
Rab11fip1	2.37376	2.30418	1.99306	1.75889
Rab20	37.6952	40.2857	25.6352	22.8554
Rab5c	221.582	228.831	259.536	253.017
Rab8b	84.1516	77.5065	81.5892	87.8016
Rabgef1	13.351	13.8635	12.5392	12.6995
Rac2	117.2	114.604	108.743	108.273
Rap1b	250.622	248.165	247.934	241.644
Rap2a	38.7377	37.5176	42.929	39.7036

Rapgef2	6.25609	5.80481	5.16072	5.73047
Rbm47	16.8121	18.9573	15.8894	16.953
Rbm7	49.1001	49.2195	49.6341	46.1014
Rcbtb2	88.7046	76.4492	60.3413	61.927
Rel	5.68493	4.83826	5.26034	5.20584
Renbp	136.079	132.151	149.38	132.137
Rffl	21.41	21.1438	13.7998	10.7253
Rgcc	1.30428	1.69695	1.04154	0.864032
Rgs1	24.4101	23.4809	24.955	28.1877
Rgs10	177.377	169.424	210.784	227.397
Rhoa	242.074	246.772	276.772	275.773
Rhog	258.049	258.526	260.37	262.539
Rilpl2	74.52	74.913	48.4303	43.1189
Rnasel	59.209	65.4395	67.7295	56.0458
Rnaset2a	25.8233	25.6992	20.9317	24.7042
Rnf13	93.2936	101.301	105.839	112.609
Rnf130	285.238	284.549	279.29	238.249
Rnf149	181.255	196.417	134.371	113.572
Rnpep	182.023	181.014	173.298	164.127
Rps27a	507.177	490.94	502.363	483.089
Rps29	1008.62	1003.84	988.663	1050.14
Runx3	1.82888	2.16951	2.60687	2.11282
Samhd1	119.896	121.188	102.235	111.252
Samsn1	22.4935	23.192	17.6144	16.3916
Sash1	58.1502	55.8694	49.6588	48.3335
Sat1	422.793	411.298	363.511	331.333
Scand1	110.935	122.146	106.433	96.0483
Scarb2	153.672	139.477	118.303	116.986
Sdcbp	488.239	468.296	537.424	512.392
Sdf2l1	122	117.766	178.446	166.542
Selplg	105.976	107.336	104.163	99.2036
Sepp1	3918.31	3563.24	3584.93	2790.3
Serinc3	937.614	889.246	903.072	935.307
Serp1	422.192	424.21	371.962	272.522
Sgk1	35.7829	35.8311	35.6197	30.1322
Sh3bgrl	140.641	148.385	191.817	175.608
Sh3bgrl3	779.806	827.674	936.277	971.857
Shfm1	441.159	433.508	464.211	431.41
Sirpa	347.297	369.735	408.057	506.014

Sirpb1b	5.40157	5.09264	2.77401	1.71012
Skap2	157.087	156.543	157.74	159.4
Skil	15.9989	17.4167	11.652	11.7606
Sla	81.1077	84.4892	70.0599	47.707
Slc11a1	137.079	136.496	92.4082	96.7006
Slc15a3	120.91	121.23	74.6233	70.1492
Slc25a5	194.14	219.428	228.757	205.18
Slc3a2	165.963	162.926	142.34	154.876
Slc7a11	5.18023	5.23242	2.73855	2.23043
Slc7a2	2.1988	2.20325	1.67674	1.36901
Slc7a8	39.2859	45.419	50.0482	64.1331
Slfn2	393.835	428.124	349.461	266.528
Slpi	2.09611	3.1606	1.40361	0.546434
Smim3	26.0343	25.9535	20.4685	18.5784
Smox	43.4416	38.4326	29.8385	27.1314
Smpdl3a	357.683	373.496	322.212	287.825
Snap23	95.5638	88.8947	88.95	84.207
Snx10	52.0012	54.2017	51.119	44.0958
Snx18	33.2731	33.8114	26.0122	23.3942
Snx20	82.997	86.0944	77.0468	72.7491
Snx3	177.101	187.207	223.04	224.075
Snx5	287.178	271.755	297.219	310.097
Socs3	42.6357	52.5587	37.6309	9.94073
Sod2	24.7877	33.0258	16.4878	15.8446
Sorl1	25.7115	22.8017	11.727	11.6753
Sowahc	18.5476	16.2767	9.57878	8.43234
Specc1l	18.801	18.7097	17.1451	17.856
Spi1	354.527	379.05	324.269	306.356
Sqstm1	450.077	457.628	399.945	426.453
Srgn	291.741	307.722	234.538	164.987
Srsf5	129.544	151.468	126.318	115.167
St3gal1	17.8645	17.9318	13.3095	14.2514
St8sia4	22.9145	20.8893	18.5945	21.8163
Stra13	75.3245	63.1432	93.8593	93.0932
Stx7	96.0402	100.244	97.9877	86.2631
Sub1	31.2526	29.9155	30.8953	26.4453
Syk	143.863	137.765	113.593	110.498
Synj1	25.0761	25.4684	22.5227	23.7843
Taldo1	536.39	565.349	459.641	452.607

Tbxas1	137.694	125.222	131.454	112.413
Tcirg1	266.063	293.911	247.419	233.244
Tcn2	224.207	232.373	243.59	220.864
Tfec	43.6818	54.2583	40.0017	22.8333
Tgfb1	164.05	173.732	159.981	149.694
Tgfbi	151.162	182.138	177.98	150.162
Tgif1	60.9977	60.8989	50.5407	53.3884
Tgm2	121.389	106.845	76.7389	82.6281
Thbs1	268.292	224.411	114.798	61.1391
Tiparp	9.99478	10.7708	8.17841	8.08601
Tkt	109.66	113.378	112.504	119.317
Tlr2	70.8426	85.3101	45.9716	39.7629
Tm6sf1	146.602	149.596	132.155	144.27
Tmbim6	316.364	322.443	346.849	332.19
Tmed5	26.3278	27.7427	24.9284	26.2861
Tmem14c	172.304	181.885	192.101	176.324
Tmem189	127.968	132.443	105.526	104.333
Tmem251	35.437	31.9315	28.6637	29.9054
Tmem256	174.947	157.709	186.634	193.453
Tmem37	60.2315	58.2277	44.5455	33.2272
Tmsb4x	3809.24	3863.21	5170.96	5108.21
Tnf	2.19625	3.25103	2.04594	2.18545
Tnfaip2	122.007	139.761	96.5903	84.1658
Tnfaip3	14.9386	17.4824	9.0019	9.6325
Tnfrsf1b	158.885	151.537	114.205	110.651
Tnfsf9	5.03481	6.45669	5.33734	4.88656
Top1	27.447	28.8794	27.3841	30.0348
Tpd52	234.214	223.434	199.876	201.331
Traf1	3.88668	5.77104	2.57198	1.82508
Trappc2l	83.1729	81.7291	91.0424	87.3976
Trem1	3.10625	4.01614	3.78842	3.02376
Trem2	641.69	607.685	690.824	751.957
Trf	361.703	271.947	165.885	183.557
Trps1	2.41764	2.39929	1.81598	2.06042
Trpv2	68.3758	71.695	72.4741	77.9975
Tubb6	22.3736	18.8537	30.5305	32.6624
Txn1	190.329	186.315	210.075	209.682
Txnrd1	53.4453	53.9657	45.3803	53.2786
Tyrobp	1733.73	1736.54	1551.47	1574.59

Ubash3b	11.1687	12.0363	13.0913	13.058
Ubc	22.9622	30.3454	25.0279	24.5641
Ube2d3	100.356	104.985	102.322	92.3294
Ubl3	91.1096	91.4459	91.0472	85.0749
Uck2	27.3739	28.7696	18.0158	10.7819
Ucp2	1433.1	1419.07	1295.19	1347.02
Unc93b1	423.858	422.623	344.083	328.371
Uqcrb	149.417	150.487	175.715	146.046
Vamp4	11.8537	11.3612	8.8589	8.63237
Vdr	0.447417	0.449792	0.406603	0.194012
Vegfa	41.4631	38.8238	25.9921	18.3783
Wfdc17	475.084	527.187	630.503	384.249
Wfdc21	0.176604	0.158943	0.329299	0.160742
Wsb1	40.6704	45.0834	44.2976	42.9706
Zc3h12a	12.2692	16.5033	10.8955	8.92114
Zeb2	36.8825	36.4407	32.5878	32.2867
Zeb2os	32.0351	29.8511	29.3278	26.8543
Zfand5	28.4906	28.3512	24.3246	20.9148
Zfp36	131.054	129.969	96.1883	106.509
Zfp36l1	76.1441	74.3572	63.8016	60.4005
Zfp703	26.9496	28.9021	27.3594	25.6745

Appendix B PDAC cell lines cytokine array

B.1 Cytokine array raw data of *KPten*$^{\Delta Acinar}$ and *KPten*$^{\Delta Duct}$ PDAC cell lines

The table below lists the raw integrated density data of cytokines expressed by two *KPten*$^{\Delta Acinar}$ PDAC cell lines and two *KPten*$^{\Delta Duct}$ PDAC cell lines. The average of duplicates is shown for each cytokine.

	***KPten*$^{\Delta Acinar}$ PDAC**		***KPten*$^{\Delta Duct}$ PDAC**	
	321A	339A	409	746A
G-CSF	1096	18954	830	326
GM-CSF	5869.5	18541	3457	420
CD54	0	11397	13.5	237
IFN-gamma	1384	2125	1481	2448.5
CXCL10	1009	2884.5	3547	3362.5
CXCL1	20326.5	35859	34020.5	25225
M-CSF	679	4050.5	7290.5	5329.5
CCL2	176	21561	26216.5	31137.5
CXCL2	577.5	11219	17373	1815.5
CCL5	427.5	164.5	7013	8967.5
CXCL12	749	950.5	12491.5	11344.5
TIMP-1	23853	23941	28558.5	29651
TNF-alpha	1824	17658.5	11614	1760

B.2 Gene expressions with neutralization of CCL5 in conditioned-BMDM groups

The figure below relative expression of genes in *KPten*$^{\Delta Acinar}$ and *KPten*$^{\Delta Duct}$ BMDMs neutralized with anti-CCL5 antibody or isotype control by qPCR. All gene expressions were normalized to the negative control (NC). All values shown as mean±SEM. **P<0.01

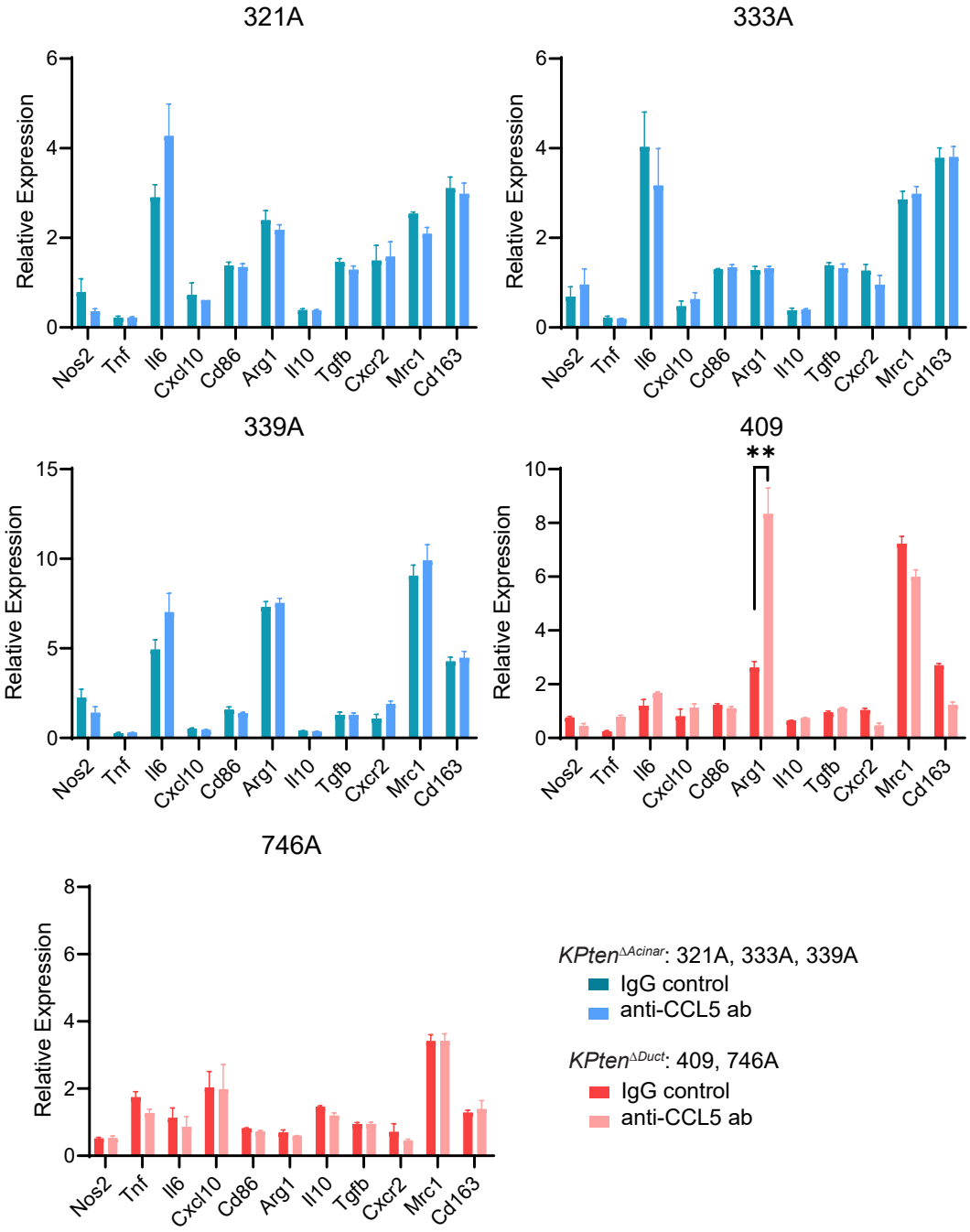

B.3 Gene expressions with neutralization of CXCL12 in conditioned-BMDM groups

The figure below relative expression of genes in *KPten*$^{\Delta Acinar}$ and *KPten*$^{\Delta Duct}$ BMDMs neutralized with anti-CXCL12 antibody or isotype control by qPCR. All gene expressions were normalized to the negative control (NC). All values shown as mean±SEM. *P<0.05

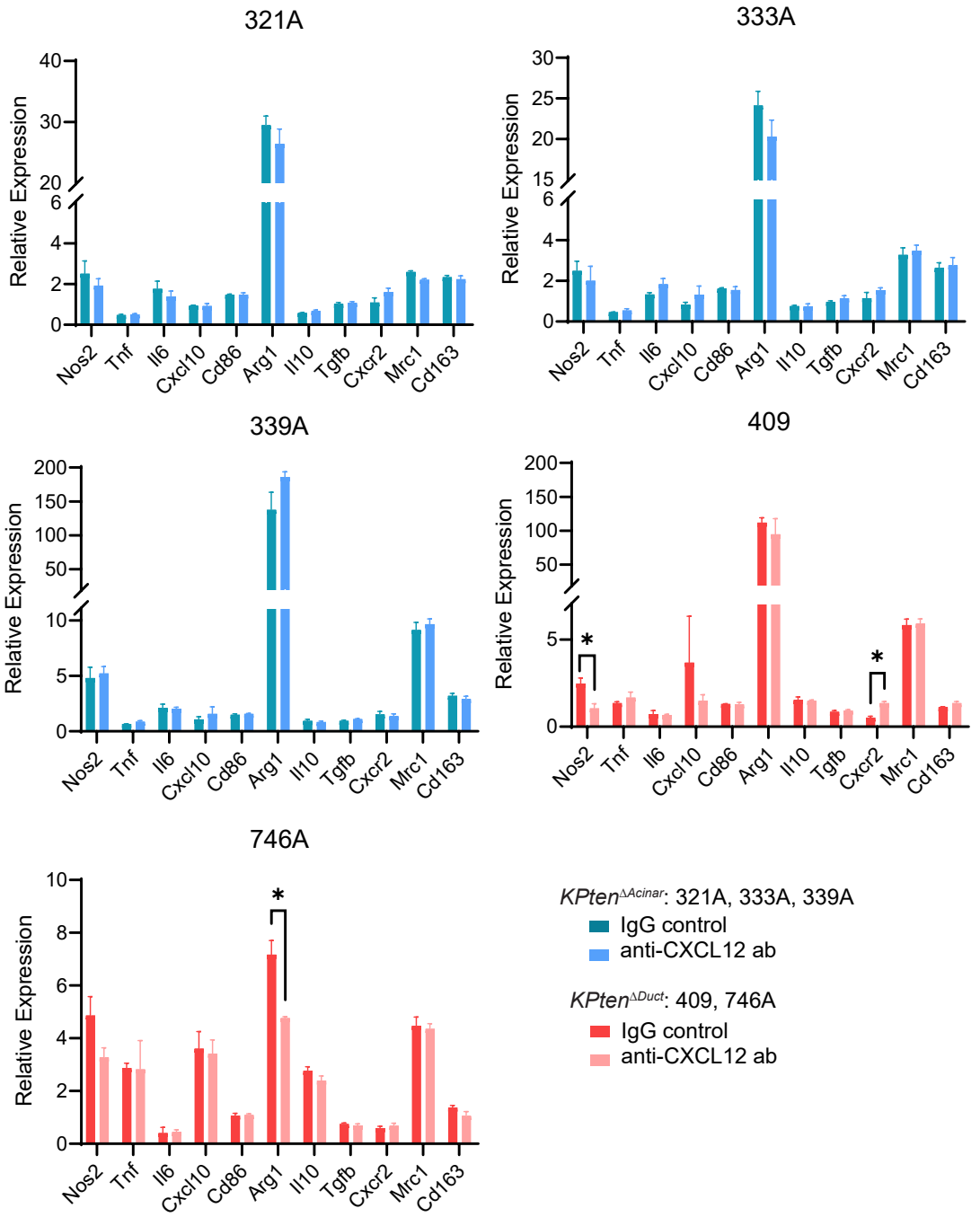

B.4 Gene expressions with neutralization of M-CSF in conditioned-BMDM groups

The figure below relative expression of genes in *KPten*$^{\Delta Acinar}$ and *KPten*$^{\Delta Duct}$ BMDMs neutralized with anti-M-CSF antibody or isotype control by qPCR. All gene expressions were normalized to the negative control (NC). All values shown as mean±SEM.